Topological semimetallic states with magnetic order: electronic states and collective excitations

A thesis
submitted in fulfillment of the requirements
for the award of the degree of

Doctor of Philosophy

by

Garima
(Reg. no. 902012018)

Under the Supervision of

Dr. Dheeraj Kumar Singh

Department of Physics and Material Science
Thapar Institute of Engineering and Technology
Patiala, Punjab - 147004, India
(May 2026)

THAPAR INSTITUTE
OF ENGINEERING & TECHNOLOGY
(Deemed to be University)

Department of Physics and Material Science
Thapar Institute of Engineering and Technology, Patiala
Punjab - 147004, India

Candidate's Declaration

I hereby declare that the work presented in the thesis entitled "**Topological semimetallic states with magnetic order: electronic states and collective excitations**" in partial fulfillment of the requirements for the award of the Degree of **Doctor of Philosophy** and submitted in the Department of Physics and Material Science of Thapar Institute of Engineering and Technology is an authentic record of my own work carried out during a period from Feb 2021 to May 2026 under the supervision of **Dr. Dheeraj Kumar Singh**, Department of Physics and Material Science, Thapar Institute of Engineering and Technology, Patiala.

The matter presented in this thesis has not been submitted by me for the award of any other degree of this or any other Institute/University.

Garima
(Reg. no. 902012018)

This is to certify that the above statement made by the candidate is true to the best of our knowledge and belief.

Dr. Dheeraj Kumar Singh
Associate Professor, DPMS
TIET Patiala

Place: Patiala
Date: 20 May 2026

Dedicated to my parents

ACKNOWLEDGMENTS

It is with profound joy and heartfelt gratitude that I take this opportunity to express my sincere acknowledgments to those who have supported me throughout this transformative journey.

First and foremost, I express my deepest respect and appreciation to my Ph.D. supervisor, Dr. Dheeraj Kumar Singh, Associate Professor, Department of Physics and Material Science, Thapar Institute of Engineering and Technology, Patiala, India. His profound wisdom, clear vision, and constant encouragement have been the guiding light throughout the course of this research. When I joined as a project assistant alongside my Ph.D. studies, I was uncertain and unrefined, and the responsibilities of being the senior-most student felt overwhelming. However, it was his unwavering mentorship, insightful guidance, and tireless support—especially in refining my manuscripts—that made this thesis possible. I will always be grateful for his dedication to my academic growth.

I am highly obliged to the Director of the Institute, Prof. Padmakumar Nair, a truly humble and visionary leader. His innovative funding initiatives enabled us to pursue research without financial worries. His thoughtful interactions with Ph.D. scholars were always insightful and inspiring, motivating me to push boundaries and discover new possibilities through his unique problem-solving perspectives.

I extend my heartfelt thanks to both the former Head of Department, Prof. Kulvir Singh, and the current HOD, Prof. B. N. Chudasama, for their consistent support throughout my research. I am especially grateful to Prof. Chudasama for his ever-approachable and understanding demeanor— every concern I brought to him was met with empathy and a solution. I also owe my sincere thanks to my doctoral committee members—Prof. Soumendu Jana, Dr. Debabrata Deb, and Dr. Harish Garg—for their valuable suggestions and constructive feedback during my half-yearly reviews, which helped shape this research.

With all my heart, I dedicate this thesis to my beloved parents, whose unconditional love and unwavering support have been the foundation of my strength. My father, who always dreamed of seeing his daughter educated, independent, and strong, now sees that dream fulfilled. My mother, with her gentle care and delicious home-cooked meals, made every homecoming a moment of warmth and rejuvenation. My younger brother, Geetansh Goyal, though younger in years, stood by me like a pillar of strength whenever I needed him. Their presence in my life is a blessing beyond words, and this achievement belongs as much to them as it does to me.

I would also like to express my heartfelt appreciation to my friend and colleague, Harun Al Rashid, who played a vital role in my Ph.D. journey. From coding support to moral backing during tough times, his presence was invaluable. I will always cherish our endless debates, disagreements, and the comforting humor that came with them. He has always been my 2 AM friend, whose humor and light-hearted teasing often lifted my spirits.

Special thanks to my juniors, Aastha Jain and Charu Dadwaria, for their warmth, care, and sisterly affection throughout this journey. Their only motive was to lift my mood when in distress with their witty jokes. I also extend my sincere gratitude to all my friends and well-wishers—named or unnamed—who offered help, encouragement, or simply stood by me during both the highs and the lows.

A very special note of gratitude goes to a dear friend, Manasvi Bhardwaj, my confidant, and an irreplaceable part of this journey. Through every moment of doubt, stress, and emotional turmoil, he stood by me like a rock—offering not just wise and practical advice, but also the quiet strength of someone who truly cares. He listened patiently when I needed to vent, encouraged me when I lost hope, and even scolded me when I needed a push—always knowing exactly what I needed, even when I didn't. He endured my countless mood swings and frustrations with unwavering patience and never once made me feel like a burden. His presence was a silent strength in the background of every step I took. This thesis is not mine alone; it carries his fingerprints just as much as it carries mine.

I also gratefully acknowledge Mrs. Neelam Sadana, Superintendent of the Physics Office, and the other staff members of the Physics Department for their timely assistance and cooperation. I thank Thapar Institute for the opportunity to take tutorials and lab sessions, which greatly boosted my confidence and deepened my understanding of core physics. The experience of working as an Assistant Professor (Contractual-I), along with a certificate and stipend, was truly the icing on the cake.

I am grateful to the anonymous reviewers of my research publications for their constructive comments, which helped enhance the quality and impact of my work. My sincere thanks also goes to the Dean of Academic Affairs, Dean of Research and Sponsored Projects, and Dean of Student Affairs for their consistent support and for fostering a nurturing and research-oriented environment at the institute.

Finally, I bow my head in gratitude to the Almighty, whose divine presence, strength, and grace carried me through every challenge and led me to this milestone.

Garima

ABSTRACT

The discovery of linear band crossings at the Fermi level in graphene, protected by symmetry and topology, marked a transformative milestone in condensed matter physics. This novel quantum phase, termed the *topological semimetal* (TSM), has catalyzed extensive exploration in a wide array of material systems. Characterized by exotic and robust electronic properties, topological semimetals have opened new frontiers in next-generation electronic and spintronic technologies, enabling the manipulation of multiple degrees of freedom in a fundamentally new manner.

Among various classes, Dirac and Weyl semimetals have emerged as key representatives, where the protection and breaking of fundamental symmetries—such as time-reversal and inversion—govern the emergence of Dirac or Weyl points. While Dirac semimetals require these symmetries (or sometimes, non-symmorphic lattice symmetries) to protect the four-fold degenerate Dirac points, Weyl semimetals arise when either symmetry is broken, resulting in pairs of Weyl nodes carrying opposite topological charges (Chern numbers). Although substantial focus has been given to three-dimensional semimetals, their two-dimensional counterparts have garnered increasing attention due to promising potential for miniaturized device applications. Notably, magnetic monolayers like FeSe and $TaCoTe_2$ have been proposed as candidates to host two-dimensional Dirac fermions.

This thesis explores the emergence and tunability of topological semimetallic phases within two-dimensional magnetically ordered systems. The first system considered is the spin-density wave (SDW) state in iron pnictides, which hosts Dirac-like features near the Fermi level. Experimentally observed metallic SDW state dictates the presence of additional pockets at the Fermi level. However, no attempt has been made in exploring the possibility of Dirac points at the Fermi level. We demonstrate that the Dirac points in this phase can be brought precisely to the Fermi level by tuning the orbital splitting between the d_{xz} and d_{yz} orbitals of iron. This tuning simultaneously suppresses non-Dirac Fermi pockets, stabilizing a Dirac semimetallic state with $(\pi, 0)$ SDW state. The orbital character and slopes of bands forming the Dirac cone are shown to be key parameters in controlling this behavior. Additionally, by eliminating second-neighbor intraorbital hopping, we reveal a perfectly nested (π, π) ordered phase in a two-orbital Hubbard model, analyze the semimetallic state, and discuss its topological characteristics.

The second system involves an antiferromagnetically (AFM) ordered state with Rashba-type spin-orbit coupling, where a Dirac semimetallic phase is realized under

specific symmetry constraints on magnetic moment orientation using the Rashba-Hubbard model. Upon introducing an in-plane magnetic field like term aligned with the moment direction, Dirac points split into Weyl points, thereby realizing a Weyl semimetallic phase.

Subsequently, we also investigate collective excitations using two primary probes: quasiparticle interference and optical conductivity. These tools elucidate the interplay between correlations, symmetry, and band topology in the ordered systems, and thereby provide insights into the possible anisotropic electronic states.

The research work presented in the thesis is organized and structured in the form of seven chapters, which are briefly described as follows:

i) **Chapter 1** introduces the fundamental concepts of topology in condensed matter physics, reviews the development of topological insulators and semimetals, and outlines the two magnetically ordered 2D systems that form the focus of this thesis.

ii) **Chapter 2** develops the theoretical framework, employing the Hubbard model for systems with broken time-reversal ($\mathcal{T}$) and inversion ($\mathcal{P}$) symmetries. It demonstrates how Dirac and Weyl semimetallic phases emerge under specific symmetry constraints and external tuning in an antiferromagnetically ordered non-symmorphic lattice. Topological invariants (Chern numbers) and edge-state dispersions are computed to confirm non-trivial band topology.

iii) **Chapter 3** examines collective excitations in AFM–TSM phases within a non-symmorphic crystal, focusing on optical conductivity and quasiparticle interference for both magnetic and non-magnetic impurities, revealing strong anisotropy in the electronic responses.

iv) **Chapter 4** addresses the realization of a Dirac semimetallic phase in a striped $(\pi, 0)$ SDW order within a multi-orbital Hubbard model. By tuning the orbital splitting δ between d_{xz} and d_{yz} orbitals, Dirac points are brought exactly to the Fermi level, eliminating additional band crossings. Edge-state dispersions for ribbons with varying orientations and chain parity are also analyzed.

v) **Chapter 5** provides a detailed analysis of optical conductivity and quasiparticle excitation spectra in the semimetallic SDW phase, demonstrating that Dirac cones near the Fermi level can play a very significant role in the origin of anisotropic transport and one-dimensional QPI patterns.

vi) **Chapter 6** explores the semimetallic state in iron-based superconductors with the checkerboard-type antiferrromagnetic order, which emerges upon suppression of second-neighbor intraorbital hopping in the minimal two-orbital model of iron pnictides. Fermi-surface reconstruction collapses the pockets into Dirac points with equal orbital contributions but anisotropic. Analytical conditions for Dirac point formation and the evolution of edge states with interaction strength are derived. Furthermore, quasiparticle interference as well as optical conductivity are also explored.

vii) **Chapter 7** summarizes the principal findings and outlines potential directions for future research in the field of topological quantum materials.

Contents

List of Figures

List of Acronyms/Abbreviations

2D	Two Dimensional
3D	Three Dimensional
AFM	Antiferromagnet
AFM-I	Antiferromagnetic Insulator
ARPES	Angle-Resolved Photoemission Spectroscopy
BZ	Brillouin Zone
CECs	Constant Energy Contours
DOS	Density of States
DP	Dirac Point
DSM	Dirac Semimetals
DSM-NM	Dirac semimetal with no magnetic order
IBS	Iron-Based Superconductors
IQHE	Integer Quantum Hall Effect
LDOS	Local Density of States
meV	milli electron volt
NLSM	Nodal Line Semimetals
OS	Orbital Splitting
QHE	Quantum Hall Effect
QPI	Quasiparticle Interference
SDW	Spin-Density Wave
SOC	Spin-Orbit Coupling
STM/STS	Scanning Tunneling Microscopy/Spectroscopy
TI	Topological Insulators
TS	Topological Superconductors
TSM	Topological Semimetals
WSM	Weyl Semimetals

List of Symbols

δ	Orbital Splitting between d_{xz} and d_{yz} orbitals
σ_i	Pauli matrices, $i = 0, 1, 2, 3$
$\mathbf{k}$	Wave vector
v_f	Fermi Velocity
$\boldsymbol{\mathcal{T}}$	Time-Reversal Symmetry
$\boldsymbol{\mathcal{P}}$	Inversion Symmetry
$\mathbf{U}$	Complex Conjugation Operator
$G = \{g\|\mathbf{t}\}$	Non-symmorphic symmetry element
$C_{2\hat{n}_\perp}$	$\hat{n}_\perp$ rotation axis perpendicular to $\hat{z}$
$M_{\hat{n}_\perp}$	Glide Mirror Lines
$M_{\hat{z}}$	Glide Mirror Planes
ϕ_n	Berry Phase associated with band n
$\mathbf{A}_n(\mathbf{k})$	Berry Vector Potential for n^{th} band
Ω_n	Berry curvature for n^{th} band
C	Chern number for a system

t	Hopping parameter
$c_{\mathbf{i}}^{\dagger}(c_{\mathbf{i}})$	Electron creation(annihilation) operator at site $\mathbf{i}$
U	Onsite Coulomb Interaction
U'	Inter-orbital Coulomb Repulsion
J	Hund's Coupling
$n_{\mathbf{i}\sigma} = c_{\mathbf{i}\sigma}^{\dagger} c_{\mathbf{i}\sigma}$	Number operator at site $\mathbf{i}$ for spin σ
μ	Chemical Potential
λ	SOC strength
Δ	Exchange Field
$\mathbf{m_i}$	Magnetic moment at site $\mathbf{i}$
$E_{\mathbf{k}}$	Energy dispersion
B_x	Magnetic field along x-direction
$\mathbf{S}^j = \frac{1}{2}\sum_{\sigma\sigma'} d_{\sigma}^{\dagger}\sigma_{\sigma\sigma'}^{j} d_{\sigma'}$	Spin operator along j direction
σ_l	Optical conductivity in the l direction
θ	Step Function
ω	Angular frequency
D_l	Drude weight in the l direction
$j_{nn'}$	Current Operator
T_{nn}	Kinetic Energy Operator for band n
$V(\mathbf{k}_1, \mathbf{k}_2) = V_0\delta(\mathbf{k}_1 - \mathbf{k}_2)$	Single-particle impurity
$\hat{G}^0(\mathbf{k}, \omega)$	Free particle Green's function
$\delta\rho(\mathbf{q}, \omega)$	Modulation in DOS

Chapter 1

Introduction

This chapter introduces topological semimetals, a class of materials that has been the subject of intense research over the past two decades because of their unique topological characteristics and the resulting exotic physical phenomena. The chapter begins with a brief discussion of the concept of topology and its relevance in condensed matter physics, and subsequently introduces topological semimetals, with particular emphasis on their interaction with magnetism.

1.1 Background

Band theory of solids serves as a fundamental theoretical framework to describe the electronic properties of crystalline materials. When individual atoms assemble to form a crystal, the discrete energy levels of isolated atoms broaden into continuous energy bands as a result of atomic overlap. The electronic properties of a solid are primarily governed by the position and occupation of the valence and conduction bands with respect to the Fermi level. The energy gap between these bands, known as the band gap, determines the material's electrical properties—whether it behaves as a conductor, semiconductor, or insulator.

In insulators, a significant energy gap exists between these bands, preventing electrical conduction under normal conditions. In contrast, metals exhibit partially filled conduction band or overlapping bands at the Fermi level, enabling free movement of charge carriers and thereby high electrical conductivity. Semiconductors, which possess a smaller band gap, can exhibit conductivity upon thermal excitation or through doping, making them highly tunable for electronic applications.

On the other hand, conventional semimetals represent an intermediate phase between metals and semiconductors, characterized by a slight overlap between the conduction and valence bands. This results in a low carrier concentration near the Fermi level, with both electrons and holes contributing to the electrical transport. Classic examples of such materials include bismuth and graphite, where the semimetallic nature arises from band structure features without necessitating any topological considerations. These systems can be well described within the conventional band theory

framework.

Over the past decade, condensed matter physics has experienced remarkable advancements in the domain of band theory, resulting into the identification of novel phases of matter characterized by unconventional and exotic properties. This could be explained in the context of topological band theory [1,2]. Traditionally, the classification of phases has been grounded in Landau's paradigm, which relies on the concept of spontaneous symmetry breaking—particularly of translational symmetry—to distinguish between different states of matter. However, the advent of topological band theory, initiated by the successful theoretical description of the quantum Hall effect (QHE) through the notion of topological order, has significantly broadened this framework [3, 4].

The subsequent discovery of topological insulators (TIs) [5–8] underscored the fundamental role of symmetry-protected, linearly dispersing topological band crossings, also known as edge states— features that had previously been overlooked despite experimental indications in certain materials. These stepping stones have catalyzed the identification of a distinct class of materials, collectively termed as *"topological materials"*, which exhibit topologically nontrivial electronic structures and possess a wide array of unconventional physical properties [2].

It has been shown in the last course of years that materials with topological characteristics can exhibit remarkable phenomena such as giant magnetoresistance [9–11], enhanced thermoelectric power [12], chiral anomaly [13–16], and quantum anomalous Hall effect [17], etc. These atypical properties distinguish them from their conventional counterparts and have sparked considerable interest due to their promising technological applications [18].

1.2 Concept of Topology

Topology is a branch of mathematics, concerned with those properties of geometric structures that are preserved under continuous and smooth transformations, including stretching, bending, and twisting, while excluding operations such as cutting or joining. Within this formalism, two objects are regarded as topologically equivalent if one can be continuously deformed into the other without changing its fundamental connectivity. A classic illustrative example is the equivalence between a doughnut and a coffee mug, both of which possess a single hole and can be smoothly deformed into each other without cutting or reattaching parts (see Fig. 1.1). Topological equivalence is often quantified using a topological invariant known as the genus, which counts the number of holes in an object. This mathematical concept forms the foundation for

understanding topologically equivalent phases in physical systems [19].

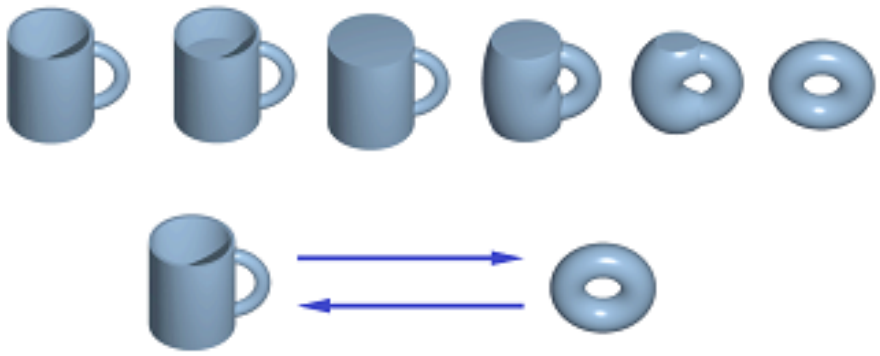

Figure 1.1: An illustration of topologically equivalent classes based on genus, g. A mug and a doughnut belong to the same topological class with genus $g = 1$, due to the presence of a single hole [20].

Within condensed matter physics, a *topological material* refers to a system in which certain physical observables—such as quantized Hall conductivity or the presence of gapless boundary modes—remain unchanged under adiabatic, continuous changes in system parameters, as long as the system does not pass through a phase transition. These observables serve as topological invariants, analogous to the genus in mathematical topology.

The emergence of topological insulators (TIs) has been a milestone in the field, representing a paradigm shift in the classification of quantum phases [21]. TIs differ from conventional insulators by exhibiting an insulating bulk while simultaneously supporting metallic, gapless states on their surfaces or edges. These surface states are the electronic states that are confined to the boundaries of a material, such as its surfaces or edges, and do not exist in the bulk spectrum. In topological insulators, the edge states exhibit a helical nature as a consequence of spin–momentum locking, whereby the spin orientation of an electron is intrinsically tied to its direction of motion. This helical structure arises from strong spin-orbit coupling and is protected by time-reversal and crystal symmetries. As a consequence, these surface states are robust against backscattering and remain stable under moderate perturbations such as chemical substitution or thermal fluctuations. Early experimental realizations include the HgTe/CdTe quantum well heterostructures [22–24] and the binary compound Bi_2Se_3 [25].

Following the discovery of TIs, attention rapidly expanded to a broader class of topological materials. These include topological semimetals (TSMs) [26], nodal line semimetals (NLSMs) [27, 28], and topological superconductors (TSs) [29]. While differing in dimensionality and symmetry protections, these phases share key features

in their low-energy electronic spectra. In particular, they host massless quasiparticle excitations that behave as Dirac or Weyl fermions, in contrast to the conventional massive fermions governed by the Schrödinger equation. The relativistic nature of these carriers leads to a variety of novel phenomena and unconventional transport properties, positioning these materials at the forefront of both fundamental research and potential technological applications.

1.3 Topological Band Crossings

Topological band crossings are typically classified into two broad categories: *accidental* and *symmetry-enforced*, based on the nature of symmetries involved in their protection.

Accidental band crossings occur at critical points in the band structure and are generally perturbatively stable. These crossings often arise as a quantum critical phase during a continuous transition between a normal (trivial) insulating phase and a topological insulating phase (see Fig. 1.2). Such crossings are protected by *symmorphic crystal symmetries*, which consist of conventional point group operations (e.g., reflections, rotations) followed by lattice translations by a full unit cell vector [30,31]. Although these symmetries can protect band degeneracies locally, the crossings themselves are not globally stable and can be eliminated through sufficiently large, yet symmetry-preserving, deformations of the Hamiltonian. Consequently, accidental band crossings are only locally robust and do not represent a stable topological phase over a wide parameter space.

In contrast, **symmetry-enforced band crossings** emerge due to non-symmorphic symmetries present in a system, which are fundamentally distinct from their symmorphic counterparts. Non-symmorphic symmetries combine point group operations with fractional lattice translations (e.g., glide planes and screw axes) [32–35]. These fractional translations introduce additional constraints on the band structure, resulting in robust degeneracies that cannot be lifted without breaking the protecting symmetry. Band crossings arising from non-symmorphic symmetries are therefore *globally stable* under all symmetry-preserving perturbations to the Hamiltonian. A detailed discussion of non-symmorphic symmetries and their implications on the band topology will be discussed later in the subsequent section.

We now turn to a class of materials that constitutes the core subject of this thesis, namely *topological semimetals*. These materials are of significant interest due to their unconventional quasiparticle excitations, tunable band structures, and potential for realizing novel quantum phenomena. The presence of topologically protected band

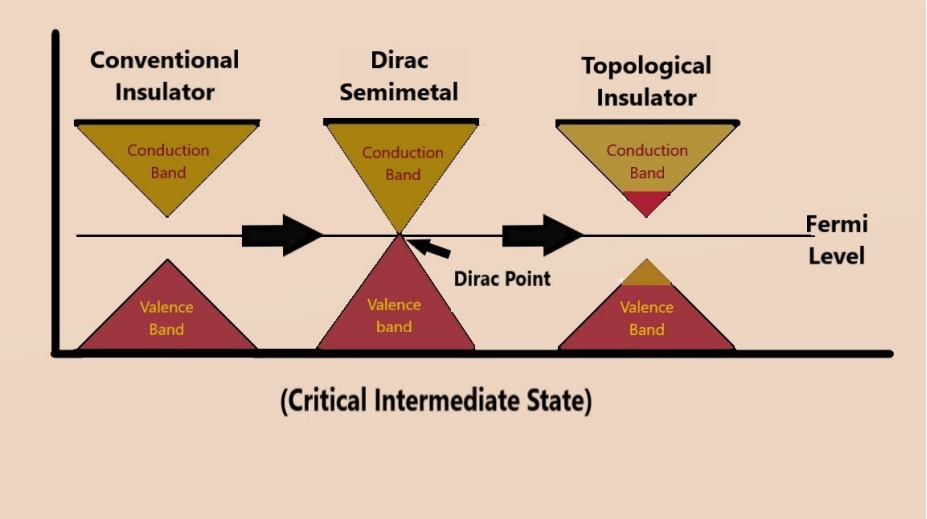

Figure 1.2: Schematic depiction of *accidental band crossing* during the topological phase transition between a trivial (conventional) and a topological insulator. The critical point, where two bands, namely valence and conduction bands touch each other at the Fermi level, defines a Dirac semimetallic state and the band touching point is referred to as the Dirac point.

crossings is central to their exotic electronic, optical, and transport properties, and provide a versatile platform for both fundamental investigations and technological applications.

1.4 Topological semimetals

Topological semimetals are distinguished by the appearance of linear band crossings at isolated points in momentum space, typically located at or near the Fermi level [36]. These crossings are associated with nontrivial topological charges and serve as sources or sinks of Berry curvature within the Brillouin zone. The linear dispersion near the crossing points leads to quasiparticle excitations that mimic relativistic fermions, characterized by exceptionally high carrier mobility. As a result, TSMs offer potential for nearly dissipationless charge transport [26], rendering them promising candidates for applications in low-power electronics, ultrafast photodetectors [38], thermal sensors [37], next-generation spintronic and magnetic memory devices [39, 40].

Figure 1.3 displays how one can obtain different topological states from a normal insulating state satisfying different symmetry criteria. If the band crossing is symmetry protected, a topological semimetallic state with robust DPs is obtained. Conversely, when the band inversion takes place, the energy band gap opens with the inverted band structure, a topological insulator possessing surface states can be obtained.

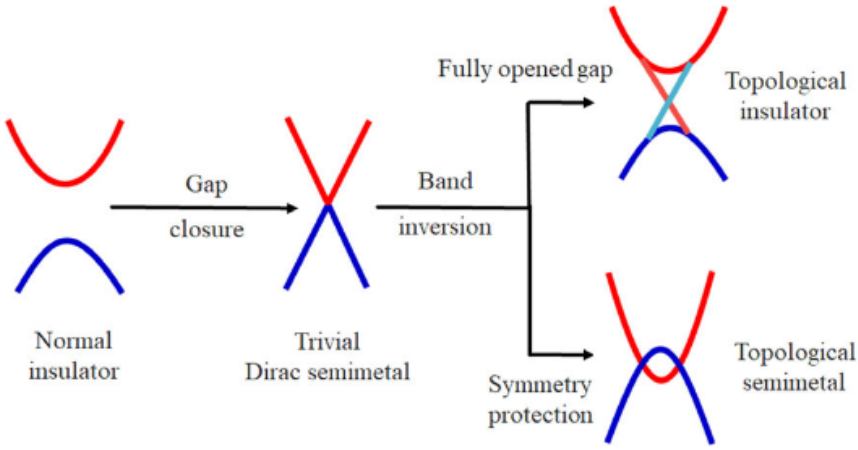

Figure 1.3: Schematic illustration of the evolution of electronic phases from a normal insulating state. A normal insulator exhibits a bulk energy gap and is non-conductive. Band inversion can result in either a topological insulator with protected surface states or a topological semimetallic (TSM) phase with robust band-touching points, if the crossing is symmetry-protected. (Fig. ref. [41])

Within the framework of band theory, the electronic states of a crystalline solid are described by a Bloch wavefunction, which can be expressed in terms of cell-periodic Bloch states $|\phi_n(\mathbf{k})\rangle$ defined within a single unit cell. These states are eigenfunctions of the Bloch Hamiltonian $H(\mathbf{k})$, satisfying the eigenvalue equation:

$$H(\mathbf{k})|\phi_n(\mathbf{k})\rangle = \varepsilon_n(\mathbf{k})|\phi_n(\mathbf{k})\rangle, \tag{1.4.1}$$

where n labels the energy bands and the eigenvalues $\varepsilon_n(\mathbf{k})$ constitute the electronic bandstructure of the material.

Band crossings occur when two or more eigenvalues become degenerate at specific points in momentum space, typically under certain symmetry constraints or fine-tuned parameter conditions. Depending on the nature and symmetry of these degeneracies, topological semimetals can be broadly classified into various subclasses. Among them, Dirac semimetals (DSMs) and Weyl semimetals (WSMs) represent two prominent categories, distinguished by the number of degeneracies, symmetry protections, and the presence or absence of inversion or time-reversal symmetry. These subclasses will be discussed in detail in the following subsections.

1.4.1 Dirac semimetals

Dirac semimetals (DSMs) represent a class of materials characterized by Dirac cone-like band dispersion at specific momenta within the first Brillouin zone [32, 36, 42]. The Bloch Hamiltonian near these points closely resembles that of a massless Dirac particle, featuring a linear energy-momentum relationship around the band cross-

ings, where conduction and valence bands meet. These bands draw a formal analogy with electrons and positrons in the Dirac mass framework. Consequently, the band crossing points are termed as Dirac points (DPs), and the state is said to be a *"Dirac semimetallic state"*. Near these points, the quasiparticle excitations are well described by a massless Dirac equation, with a remarkably high Fermi velocity $v_f \approx 10^5$ m/s. The effective low-energy Hamiltonian can be expressed in the matrix form as

$$\mathcal{H}(\mathbf{k}) = \begin{pmatrix} \hbar v_f \boldsymbol{\sigma} \cdot \mathbf{k} & 0 \\ 0 & -\hbar v_f \boldsymbol{\sigma} \cdot \mathbf{k} \end{pmatrix} \tag{1.4.2}$$

where $\boldsymbol{\sigma} = (\sigma_x, \sigma_y, \sigma_z)$ are the three Pauli matrices and $\mathbf{k}$ is the wave vector. The above matrix expression indicates that the band crossings are non-removable and can only occur in crystals that are time-reversal invariant and possess inversion symmetry.

This extraordinary behavior of Dirac fermionic quasiparticles in the vicinity of the Fermi energy gives rise to the distinctive and unconventional properties observed in these materials. The electronic properties of Dirac systems can be systematically tuned by shifting the chemical potential with respect to the Dirac nodes, which may be achieved through chemical substitution, external pressure, or carrier doping [45].

DSM is often inherited from TI as an intermediate phase during a topological phase transition between a conventional insulator to a topological insulator (TI) [46]. At the quantum critical point of this transition, the system enters a phase where the topological order changes, and conduction and valence bands touch each other at isolated points in momentum space (see Fig. 1.2). The persistence of these Dirac points is ensured by the combination of *crystalline symmetries* and *non-spatial symmetries*, discussed below.

Non-spatial symmetries

Non-spatial symmetries act locally in the position space and do not transform different lattice sites onto one another. Time-reversal ($\boldsymbol{\mathcal{T}}$) and inversion ($\boldsymbol{\mathcal{P}}$) symmetries are prominent examples of this class, and together they play a crucial role in stabilizing Dirac points [47].

1. *TR symmetry* ($\boldsymbol{\mathcal{T}}$): In the absence of an external magnetic field, physical systems are generally invariant under time-reversal symmetry. This symmetry operation reverses the spin of a particle while transforming the Hamiltonian from momentum $\mathbf{k}$ to $-\mathbf{k}$. Mathematically, $\boldsymbol{\mathcal{T}}$ is represented by an anti-unitary operator composed of a unitary part $\mathbf{U} = i\boldsymbol{\sigma_y}$ and complex conjugation $\boldsymbol{\mathcal{K}}$, such

that $\boldsymbol{\mathcal{T}} = \mathbf{U}\boldsymbol{\mathcal{K}}$.

A Bloch Hamiltonian that respects time-reversal symmetry satisfies the condition:

$$\boldsymbol{\mathcal{T}}\mathcal{H}(-\mathbf{k}) = \mathcal{H}(\mathbf{k})\boldsymbol{\mathcal{T}} \tag{1.4.3}$$

Consequently, the energy eigenvalues obey the relation $E_{n\uparrow}(\mathbf{k}) = E_{n\downarrow}(-\mathbf{k})$.

2. *Inversion symmetry* ($\boldsymbol{\mathcal{P}}$): This operation retains the spin of a particle while $\mathbf{k}$ to $-\mathbf{k}$ transformation. This symmetry operation can be represented in different forms, however, a common representation of the inversion operator is $\boldsymbol{\mathcal{P}} = \boldsymbol{\sigma_x}$, under which the Bloch Hamiltonian transforms as:

$$\boldsymbol{\mathcal{P}}\mathcal{H}(-\mathbf{k}) = \mathcal{H}(\mathbf{k})\boldsymbol{\mathcal{P}} \tag{1.4.4}$$

Accordingly, the eigenenergies satisfy $E_{n\uparrow}(\mathbf{k}) = E_{n\uparrow}(-\mathbf{k})$.

By combining these two symmetry constraints, one arrives at the relation $E_{n\uparrow}(\mathbf{k}) = E_{n\downarrow}(\mathbf{k})$, indicating that each energy band is at least twofold degenerate. For fermionic particles carrying spin $s = \frac{1}{2}$, it follows that $\boldsymbol{\mathcal{T}}^2 = -1$ and $(\boldsymbol{\mathcal{T}}\boldsymbol{\mathcal{P}})^2 = -1$, reinforcing this double degeneracy. This observation is a direct consequence of the *Kramers theorem*, which states that any $\boldsymbol{\mathcal{T}}$-invariant fermionic system must have doubly degenerate eigenstates. Therefore, Dirac points arise as the crossing points of such doubly degenerate bands. Importantly, the stability of Dirac points crucially depends on the simultaneous preservation of both time-reversal ($\boldsymbol{\mathcal{T}}$) and inversion ($\boldsymbol{\mathcal{P}}$) symmetries.

Lattice or non-symmorphic symmetries

Non-symmorphic symmetries arise in crystals containing more than one atom per unit cell [31, 34, 35, 48–51]. In systems with a sublattice structure, such as a bipartite lattice, the translational symmetry no longer preserves the spatial origin, leading to an effective enlargement of the unit cell. Consequently, the Brillouin zone (BZ) folds and reduces in size. In these cases, non-symmorphic symmetries play a crucial role in protecting Dirac points (DPs).

A non-symmorphic symmetry element is generally denoted by $G = \{g|\mathbf{t}\}$, where g represents a point group operation and $\mathbf{t}$ is a fractional lattice translation vector [52]. Examples include screw rotations such as $C_{2\hat{n}_\perp}$ (with the rotation axis $\hat{n}_\perp$ perpendicular to $\hat{z}$), glide mirror lines $M_{\hat{n}_\perp}$, and glide mirror planes $M_{\hat{z}}$. Typically, the fractional translation $\mathbf{t}$ lies within the g-invariant plane and satisfies $g\mathbf{t} = \mathbf{t}$.

To better understand these symmetry operations, let us consider two illustrative examples: a twofold screw axis rotation and a glide mirror plane, each combined with a half-translation. A simple schematic is shown in Fig. 1.4.

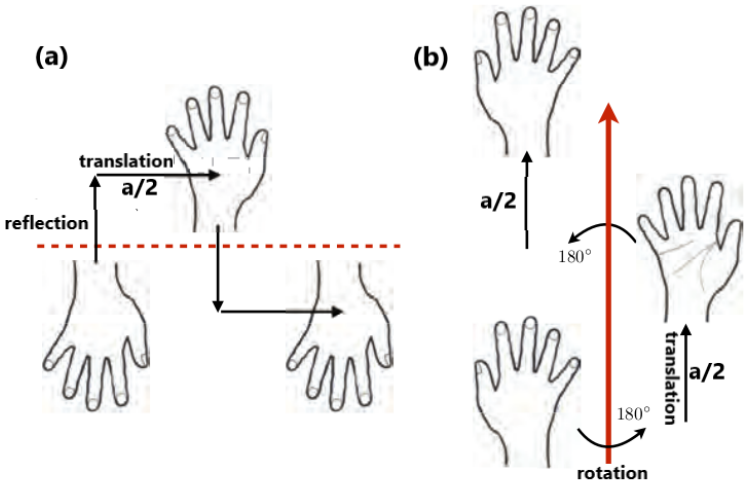

Figure 1.4: An illustration of non-symmorphic symmetries: (a) glide reflection and (b) two-fold screw rotation followed by two half translations.

The twofold screw rotation about the x-axis, combined with a half-lattice translation along the same direction, is represented as $G_{2\hat{x}} = \{C_{2\hat{x}}|\frac{1}{2}0\}$. Applying this operation twice results in a full lattice translation along the x-axis, that is,

$$G_{2\hat{x}}^2 = \pm T_x, \tag{1.4.5}$$

where T_x denotes the full translation along x and the $\pm$ sign arises from the nature of quasiparticles: g^n equals -1 for spin-$\frac{1}{2}$ particles and $+1$ for spinless particles after applying n-fold operation n times.

Similarly, the glide mirror operation involving reflection about the xy-plane combined with half-lattice translations along both x and y directions is represented as $G_{\hat{z}} = \{M_{\hat{z}}|\frac{1}{2}\frac{1}{2}\}$. This operation also satisfies the relation

$$G_{\hat{z}}^2 = \pm T_a, \tag{1.4.6}$$

where $M_{\hat{z}}$ denotes the mirror reflection through the xy-plane, and T_a represents the full lattice translation along the diagonal direction in the plane.

Band degeneracy obtained by the operators $\{g|\mathbf{t}\}$ in the invariant g-space satisfying $g\mathbf{k} = \mathbf{k}$ suggests that Bloch states $u_m(\mathbf{k})$ can be chosen as the eigenstates which commute simultaneously with both $\{g|\mathbf{t}\}$ and $\mathcal{H}(\mathbf{k})$. Eigenvalues of $\{g|\mathbf{t}\}$ operated on Bloch states $u_m(\mathbf{k})$ are obtained as

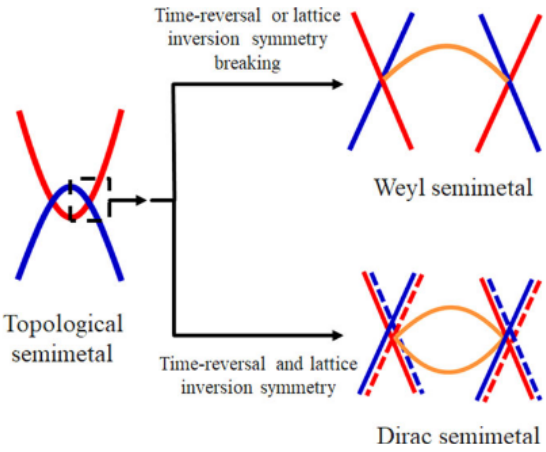

Figure 1.5: WSM obtained as a result of symmetry breaking in a topological semimetal while DSM requires the simultaneous preservation of $\mathcal{T}$ and $\mathcal{P}$ [41].

$$\{g|\mathbf{t}\}|u_m(\mathbf{k})\rangle = \lambda e^{im\mathbf{k}\cdot\mathbf{t}}|u_m(\mathbf{k})\rangle \tag{1.4.7}$$

where λ is a real number and the phase factor $e^{im\mathbf{k}\cdot\mathbf{t}}$ switches the two eigenstates which sustains band crossings at discrete points. For $\mathbf{k} \to \mathbf{k} + \mathbf{G}$, $e^{i\mathbf{G}\cdot\mathbf{t}} = -1$ for odd reciprocal lattice vectors. As a consequence, the two degenerate band branches are compelled to cross an odd number of times when traversing the Brillouin zone boundary. This odd number of intersections constitutes a necessary condition for the emergence of topologically nontrivial surface states.

1.4.2 Weyl semimetals (WSM)

Weyl semimetals can be realized through breaking of either inversion ($\mathcal{P}$) or time-reversal ($\mathcal{T}$) symmetry. When inversion symmetry is broken while $\mathcal{T}$ is preserved, the lifting of band degeneracy leads to Weyl nodes that appear in multiples of four, as observed in non-centrosymmetric TaAs-family materials (TaAs, NbAs, TaP, NbP) [16, 53–55], which exhibit clear Fermi arc surface states and Berry-curvature–driven transport signatures. In contrast, when $\mathcal{T}$ symmetry is broken while inversion remains intact, magnetic ordering splits band degeneracies into pairs of Weyl nodes related by $\mathbf{k} \to -\mathbf{k}$. Representative examples include pyrochlore iridates $A_2Ir_2O_7$ [56], ferromagnetic $Co_3Sn_2S_2$ [57, 58], and the non-collinear antiferromagnets Mn_3Sn and Mn_3Ge [59–61], all of which display large anomalous Hall responses arising from strong Berry curvature. These two routes highlight how crystal symmetry and magnetic ordering provide complementary pathways for realizing Weyl fermions in solids.

An illustration of different semimetallic phases emerging under the presence or absence of $\mathcal{T}$ and $\mathcal{P}$ symmetries is shown in Fig. 1.5. The distinction between topo-

logically trivial and non-trivial phases is characterized by the topological order of the system, which is quantified by the so-called *Chern number*.

The following section provides a detailed mathematical and physical interpretation of the frequently used concepts of *winding number* or *Chern number*.

1.5 Chern number

The notion of topological order emerged from the theoretical understanding of the Integer Quantum Hall Effect (IQHE), where the Hall conductivity assumes quantized values of the form $N(e^2/h)$, with the integer N identified as a topological invariant known as the *Chern number*.

Fundamentally, this concept stems from the *Berry phase*, a central idea in topological band theory [62]. First formulated by M. V. Berry, the Berry phase describes a geometric phase accumulated during the adiabatic evolution of a system subjected to slowly varying external parameters. When the system follows a closed loop $\mathcal{S}$ in parameter space, the resulting phase encodes essential information about the underlying topological structure of the electronic states [63].

The time evolution of a quantum system is governed by the time-dependent Schrödinger equation [64],

$$H(\eta(t))|\Phi(t)\rangle = i\hbar\partial_t|\Phi(t)\rangle \tag{1.5.1}$$

where $|\Phi(t)\rangle$ denotes the state vector of the system at time t and $\eta(t)$ represents a set of slowly varying external parameters.

Under adiabatic conditions, the system's wavefunction acquires a phase. Accordingly, the wavefunction may be written as $|\Phi(t)\rangle = e^{-i\theta(t)}|u(\eta(t))\rangle$, with $|u(\eta(t))\rangle$ denoting the instantaneous eigenstate of the Hamiltonian. Substituting this ansatz into the Schrödinger equation and utilizing the eigenvalue equation $H(\eta(t))|u(\eta(t))\rangle = \varepsilon_n(\eta(t))|u(\eta(t))\rangle$, one arrives at:

$$H(\eta(t))|u(\eta(t)\rangle = \hbar\dot{\theta}(t)|u(\eta(t)\rangle + i\hbar\frac{d}{dt}|u(\eta(t)\rangle \tag{1.5.2}$$

Here, the first term corresponds to the conventional dynamical phase, while the second term captures the geometric contribution. The negative of this geometric phase is identified as the *Berry phase*.

When the parameter space corresponds to a periodic lattice, the cell-periodic part of the Bloch function satisfies $u_{n\mathbf{k}}(\mathbf{r}) = u_{n\mathbf{k}}(\mathbf{r} + R_n)$. Accordingly, for a closed trajectory in momentum space, such as a loop enclosing the Brillouin zone, the Bloch wave

function for band n can be expressed as $\Phi_{n\mathbf{k}} = e^{i\mathbf{k}\cdot\mathbf{r}} u_{n\mathbf{k}}(\mathbf{r})$. Thus, the Berry phase ϕ_n associated with band n can be written as [20]

$$\phi_n = \oint i\langle u_{n\mathbf{k}}|\nabla_{\mathbf{k}}|u_{n\mathbf{k}}\rangle \cdot d\mathbf{k} \tag{1.5.3}$$

From the analogy of vector potential in the electromagnetic theory, one can define the Berry vector potential as

$$\mathbf{A}_n(\mathbf{k}) = i\langle u_{n\mathbf{k}}|\boldsymbol{\nabla}_{\mathbf{k}}|u_{n\mathbf{k}}\rangle \tag{1.5.4}$$

This implies that $\phi_n = \oint \mathbf{A}_n(\mathbf{k}) \cdot d\mathbf{k}$.

Applying Stokes' Theorem, one can represent the above equation in the following form.

$$\phi_n = \int_{\mathcal{S}} (\boldsymbol{\nabla}_{\mathbf{k}} \times \mathbf{A}_n(\mathbf{k})) \cdot d\mathbf{S} = \int_{\mathcal{S}} \boldsymbol{F}_n \cdot d\mathbf{S} \tag{1.5.5}$$

where $\mathcal{S}$ is the enclosed surface area in the BZ. $\boldsymbol{F}_n = \nabla_{\mathbf{k}} \times \mathbf{A}_n(\mathbf{k})$ is known as the Berry curvature for band n and plays a role analogous to magnetic flux density in momentum space.

The topological invariant associated with the n^{th} band, namely the Chern number, is defined as the integral of the Berry curvature over a closed surface in momentum space,

$$C^{(n)} = \frac{1}{2\pi} \int_{\mathcal{S}} \boldsymbol{F}_n(\mathbf{k}) d\mathbf{k} \tag{1.5.6}$$

Thus, total Chern number $C = \sum_n C^{(n)}$ summed over all the occupied bands remains invariant even if there are degeneracies. This invariant is an intrinsic characteristic of the electronic band structure and plays a central role in determining the transport behavior of the system. The Chern number gives a quantitative value of the phase accumulated when the system is moved very slowly in the BZ.

Chern number for a trivial system turns out to be zero for the individual bands and non-zero for the non-trivial ones. This property helps to distinguish between the topological and non-topological phases. For instance, the Chern number for a Dirac point is zero while it is non-zero for individual bands whose winding numbers cancel out in pairs. Similarly, when a Dirac point splits, a pair of Weyl points with opposite winding numbers appear.

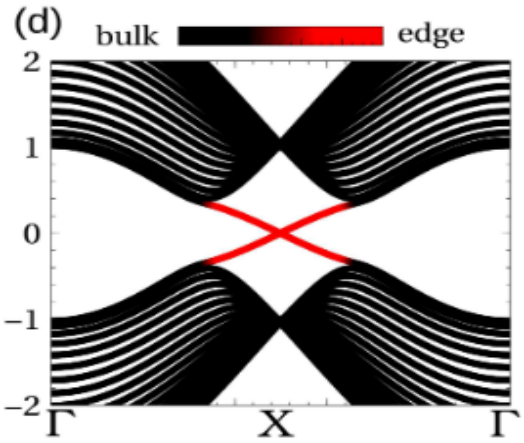

Figure 1.6: Schematic representation of edge bands in a graphene-like system with a zigzag ribbon geometry. The red curves correspond to edge-localized states [75].

1.6 Edge states

A key consequence of the nontrivial topology of electronic band structures is the appearance of gapless edge states at boundaries where the topological invariant changes [65]. In topological insulators, these edge states manifest as counter-propagating modes of opposite spin polarization, effectively act as one-dimensional conductors, bridging the energy gap between the valence and conduction bands [66,67]. Remarkably, such edge states can persist even in systems lacking magnetic ordering [68].

There are numerous instances where edge states appear in materials lacking both magnetic order and Dirac cone structures [68, 69]. Furthermore, Dirac and Weyl semimetals are also known to host robust edge states [70,71]. These phenomena arise because a one-dimensional Hamiltonian can often be continuously transformed into a form characterized by a nontrivial, topologically protected winding number. In the case of graphene, edge states are intimately linked to the Dirac cones located at the K and K' points of the Brillouin zone [72–74].

An illustration of the edge-state spectrum in a graphene-like material is shown in Fig. 1.6 [75]. Here, the bulk valence and conduction bands are indicated in black, while red curves represent edge-localized states bridging the energy gap. These edge modes highlight the profound relationship between bulk band topology and boundary phenomena, which is central to the understanding of topological phases of matter.

1.7 Prediction of TSM in 2D and 3D

The notion of two-dimensional Dirac semimetals (DSMs) originated with the discovery of the Dirac semimetallic state in graphene, which inspired extensive research

into gapless systems with non-trivial topology. Graphene's honeycomb lattice, comprising two sublattices, hosts six band crossing points, two of which are Dirac points protected by time-reversal and inversion symmetries in the absence of spin-orbit coupling (SOC) [76, 77]. The introduction of SOC, analogous to applying a magnetic field, breaks time-reversal symmetry and lifts the band degeneracy [78, 79]. Consequently, significant efforts have been made to identify symmetry-protected DSMs in the presence of SOC. Recent studies suggest that non-symmorphic crystalline symmetries are essential for protecting Dirac cones in 2D under SOC [34]. One of the promising materials include monolayer of HfGeTe, which exhibits Dirac cones at the Brillouin zone boundaries, and X_3SiTe_6 (X = Ta, Nb) monolayers [80], predicted to host 2D Dirac points as well [81, 82].

Dirac points can also be stabilized in three dimensions. Early theoretical candidates such as β-cristobalite BiO_2 [32] were followed by experimental signatures in materials like Na_3Bi [83] and Cd_3As_2 [84, 85]. Two principal mechanisms protect 3D Dirac points [42]: one through band inversion during a transition between trivial and topological insulators such as lanthanum monopnictides [43, 44], where the simultaneous presence of inversion and time-reversal symmetries is essential. These so-called *accidental band crossings* characterize the aforementioned systems [86]. Breaking either symmetry can split Dirac points into Weyl points. In some cases, small symmetry-deforming perturbations can also destroy band crossings and lead to an insulating state. Alternatively, Dirac points can arise from direct conduction-valence band contacts at isolated momenta, stabilized by non-symmorphic symmetries even in the absence of $\boldsymbol{\mathcal{T}}$ and $\boldsymbol{\mathcal{P}}$.

1.8 TSM in magnetically ordered systems

Magnetic ordering in topological semimetals profoundly alters their electronic structures by breaking time-reversal symmetry, lifting degeneracies, and inducing spin-polarized band states. These changes can drive a range of topological phase transitions, including the conversion of Dirac semimetals into Weyl semimetals [87], the emergence of Chern or axion insulating phases [96, 97], and the realization of higher-order topological states [98]. Magnetically ordered topological semimetals are characterized by distinctive transport signatures such as the anomalous Hall effect [99, 100], modified chiral anomaly responses [101, 102], and novel magneto-optical phenomena [103]. Elucidating the relationship between non-magnetic and magnetic semimetals deepens our understanding of symmetry-protected topological transitions and offers pathways for engineering emergent quantum phases. Owing to their potential

applications in spintronics [104–106], low-power transfer, and optoelectronics [107], these systems are of considerable interest both fundamentally and technologically. In the subsequent discussion, we briefly examine two magnetically ordered systems proposed as candidates for hosting topological semimetallic phases, particularly Dirac semimetals.

1.8.1 2D Dirac points with spin-orbit coupling

Young *et al.* first proposed the stabilization of Dirac points (DPs) in two-dimensional systems possessing non-symmorphic symmetries when spin-orbit coupling (SOC) is present [34]. This work marked an initial step towards realizing 2D Dirac semimetals (DSMs) in spin-orbit coupled materials. A key requirement for such stability is the presence of non-symmorphic crystalline symmetries. In Hamiltonians exhibiting multiple symmetries, including time-reversal ($\boldsymbol{\mathcal{T}}$) and inversion ($\boldsymbol{\mathcal{P}}$) symmetries, Dirac points are protected; however, SOC typically causes band splitting except at high-symmetry points known as time-reversal invariant momenta (TRIMs). Young *et al.* demonstrated that symmetry-protected Dirac points cannot appear as isolated entities in two-dimensional systems; instead, symmetry-equivalent DPs must exist at the Brillouin zone (BZ) boundaries, stabilized by the spatial and non-symmorphic symmetries.

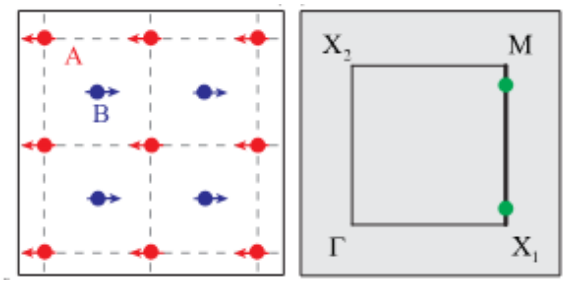

Figure 1.7: Antiferromagnetically ordered spin configuration on two sublattices: atoms from sublattice A (red) and B (blue) are displaced along $+z$ and $-z$ directions, respectively, introducing non-symmorphic symmetry. For magnetic moments aligned along x, symmetry-protected Dirac points (green dots) emerge along the $X_1 - M$ path [87].

Building upon this foundation, Wang *et al.* [87] theoretically explored Dirac semimetals in magnetically ordered systems featuring antiferromagnetic (AFM) spin configurations. In their model, the robustness of Dirac nodes depends critically on the direction of magnetic ordering and the underlying lattice symmetries. Their analysis showed that robust Dirac points could be preserved in AFM-ordered crystals exhibiting non-symmorphic symmetry. As illustrated in Fig. 1.7, atoms of sublattice A (red)

and sublattice B (blue) are displaced along $+z$ and $-z$ directions, respectively, introducing non-symmorphic elements into the lattice. Using a tight-binding model, Wang *et al.* demonstrated the presence of stable Dirac points along $X_1 - M$ path, protected by the combined $\boldsymbol{\mathcal{TP}}$ symmetry. When the magnetic moments are aligned along the x-axis, the preservation of screw axis operations $\{C_{2\hat{x}/\hat{y}}|\mathbf{t}\}$ and glide mirror symmetries $\{M_{\hat{x}/\hat{y}}|\mathbf{t}\}$ ensures the protection of these Dirac points.

Over the past decade, extensive efforts have been devoted to identifying materials that host DPs in magnetically ordered states. First-principles calculations and theoretical predictions have suggested robust DPs in several systems with magnetic order. One notable candidate is CuMnAs [88], predicted to host symmetry-protected DPs in its orthorhombic AFM state where both $\boldsymbol{\mathcal{T}}$ and $\boldsymbol{\mathcal{P}}$ symmetries are broken. Additional proposals include magnetic systems at fractional band fillings, where non-symmorphic symmetries play a central role in protecting DPs. Prominent examples include monolayers of FeSe [89] and $TaCoTe_2$ [90], where DPs persist even in the presence of SOC. Anisotropic Dirac points have also been reported in $AMnBi_2$ (A = Ca, Sr), which is further substantiated by neutron diffraction results [91–93]. Earlier, it was suggested that $SrMnBi_2$ can also host DPs when SOC is present with Mn spins being ordered antiferromagnetically. However, the Dirac fermions become massive around the Fermi level. Similarly, transport measurements reveal the signatures of Dirac fermions in two-dimensional layered compounds such as $YbMnBi_2$ [94] and $EuMnBi_2$ [95]. Collectively, these results establish a foundation for designing magnetically functionalized Dirac materials with promising potential for spintronic applications.

1.8.2 Dirac Cones and Nodal SDW State in Iron Pnictides

Over the past decade, iron pnictides have been intensively investigated due to their potential for high-temperature superconductivity [108–110] and a range of unconventional electronic properties [111, 112]. Their complex multiband structure supports multiple phases, including nematic, spin-density wave (SDW), and superconducting states [113].

The parent state of iron pnictides is a collinear antiferromagnet characterized by a commensurate ordering wave vector of either $(\pi, 0)$ or $(0, \pi)$ [114–116]. This ordering vector appears in the electronic band structure as a nesting vector that connects the hole pocket centered at the $\Gamma(0, 0)$ point with the electron pocket around the $X(\pi, 0)$ point. In this magnetically ordered phase, the band structure exhibits linearly dispersing features that form cone-like crossings. The quasiparticles associated with these Dirac cones behave as massless relativistic fermions and obey the Dirac equation. The emergence of Dirac cones originates from the multiorbital nature of iron pnictides,

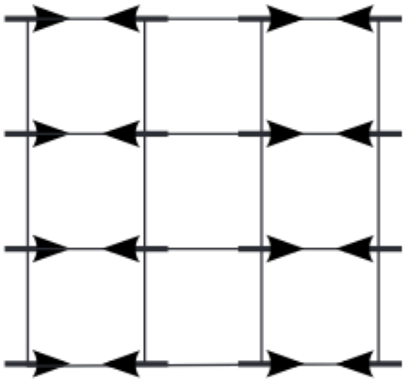

Figure 1.8: Real-space schematic of the $(\pi, 0)$ SDW order. Spins align antiferromagnetically and ferromagnetically along x- and y-axes, respectively [118].

which arises due to the hybridization between Fe $3d$ orbitals and pnictogen $4p$ orbitals. Consequently, an accurate description of the electronic structure requires the inclusion of all Fe $3d$ states [117].

At low temperatures, iron pnictides undergo SDW ordering, leading to Fermi surface reconstruction, Brillouin zone folding, and opening of energy gaps due to electron-hole interactions. SDW state consists of chains of atoms arranged in a collinear magnetic order in which spins are aligned parallely in one direction while anti-parallely in the other (see Fig. 1.8). Generally, SDW formation gaps the spectrum when the nesting condition is satisfied across the entire Fermi surface. However, in iron-based superconductors, due to Fermi surface topology and a coupling between electron and hole pockets induces a partial SDW gap.

Theoretical studies based on the five-orbital model predict that the electron Fermi surface is odd under mirror reflection, while the outer hole pocket is even. As a result, the SDW matrix element between them vanishes, giving rise to a nodal SDW phase. The existence of a Dirac node can further be quantified in terms of a topological invariant, 'vorticity' quantum number. The SDW state connects electron pockets of zero vorticity with hole pockets of $+2$ vorticity. This vorticity mismatch is responsible for the gapless or "nodal SDW" state with the apex of Dirac cones not far away from the Fermi level [118]. Consequently, the parent magnetic compounds remain semimetallic even in the presence of strong electronic correlations, which is further substantiated by angle-resolved photoemission spectroscopy (ARPES) measurements (Fig. 1.9) [119, 120].

The linear energy dispersion near Dirac points results in high carrier mobility and low effective mass, enhancing transport properties and optical conductivity [120, 121]. Dirac fermions emerging in the spin-density-wave (SDW) state of iron pnictides have been shown to produce nearly linear magnetoresistance under applied magnetic fields,

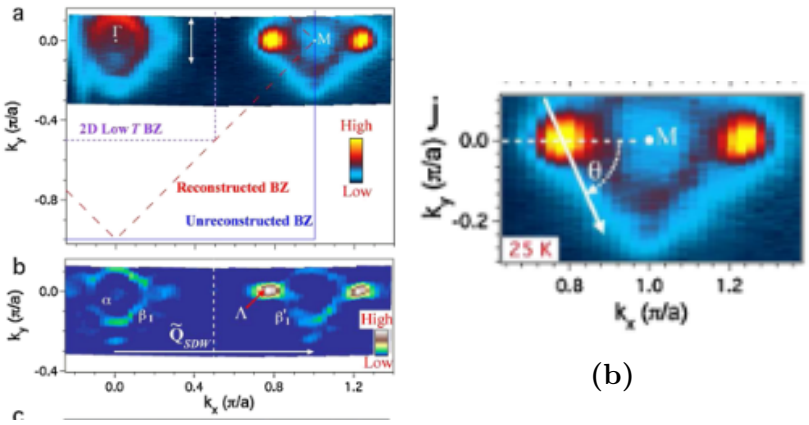

Figure 1.9: ARPES evidence of Dirac cone formation close to the Fermi surface in the SDW state of $BaFe_2As_2$ [120].

reflecting the relativistic nature of the low-energy quasiparticles [122,123]. The strong interplay between magnetism and superconductivity in these materials gives rise to gapless excitations, which significantly influence their thermodynamic and spectroscopic responses [124,125]. Recent interest has been further motivated by the recognition that iron-based superconductors can host nontrivial band topology, potentially supporting Majorana modes and other exotic quasiparticles [126], making these systems promising candidates for applications in quantum information processing and the exploration of novel quantum phases [127–130]. Consequently, iron pnictides provide a rich platform for studying unconventional superconductivity, topological phenomena, and emergent relativistic quasiparticles.

1.9 Collective excitations in the magnetically ordered systems

Magnetically ordered systems host a rich variety of collective excitations arising from the interplay between spin, charge, and lattice degrees of freedom [131,132]. The collective excitations represent coherent modes involving many-body correlations. They not only determine low-energy properties of a system but also serve as fingerprints of the underlying order and symmetry. In the context of topological semimetals, the study of such excitations is of particular importance because their interplay with Dirac or Weyl fermions can lead to exotic emergent phenomena [133–135].

Collective excitations manifest in diverse forms in magnetically ordered states, including spin waves (magnons), charge- and orbital-density fluctuations. Magnons, originating from coherent spin precessions, are strongly influenced by spin–orbit cou-

pling and lattice symmetries, which can endow them with nontrivial topological character [136, 137]. Their interaction with Dirac quasiparticles leads to renormalized spectra, hybrid modes such as magnon polarons, and the stabilization of exotic textures like skyrmions [138]. Meanwhile, charge and orbital collective modes, particularly SDWs driven by Fermi surface nesting, reconstruct the electronic structure while sometimes preserving symmetry-protected Dirac states [139,140]. Together, these excitations define the low-energy dynamics of ordered Dirac materials and establish the stage for their experimental detection.

The fingerprints of collective excitations in ordered systems often appear in quasiparticle interference (QPI) patterns, observed via scanning tunneling microscopy (STM) [141, 142]. In magnetically ordered Dirac semimetals, scattering of quasiparticles by electrons generates distinctive interference features in momentum-resolved maps. These QPI signatures directly reflect both the reconstructed band topology and the coupling between electronic states and collective modes [143,144]. STM-based QPI measurements directly visualize interference patterns arising from scattering between ordered states with Dirac quasiparticles.

Another powerful probe is optical conductivity, which captures dynamical responses of charge carriers in the presence of magnetic order [145]. Optical conductivity spectra can reveal gap openings due to SDW formation [146], magnon-assisted absorption features, Kerr responses [147], and renormalized Drude weights caused by coupling with collective excitations [148]. In Dirac systems, deviations from the characteristic linear frequency dependence of conductivity often signal the influence of ordering and many-body interactions [149, 150]. Thus, QPI and optical conductivity serve as complementary tools for identifying and characterizing the role of collective modes in ordered topological systems.

QPI and optical conductivity studies are particularly promising, as they enable precise identification of order-induced modifications to the electronic spectrum and provide guidance for engineering tunable quantum phases. Looking forward, the combination of high-resolution spectroscopy, theoretical modeling, and external control parameters (strain, pressure, and fields) is expected to reveal novel intertwined modes, thereby advancing both science and technology of magnetically ordered Dirac materials.

1.10 Motivation for the Present Research Work

Despite substantial progress in the understanding of high-temperature superconductivity and a range of unconventional phenomena in iron-based pnictides and chalco-

genides, certain aspects of their parent phases remain largely unexplored from both theoretical and experimental perspectives. Although signatures of Dirac pockets have been obtained in experimental studies within the spin-density wave (SDW) state of these compounds, limited attention has been devoted to investigating the potential realization of a Dirac semimetallic phase, despite its well-known significance for exceptional transport and electronic properties. Addressing this gap, the present work seeks to systematically explore the relevant parameter space, employing realistic inputs within the multi-orbital Hubbard model framework, to determine the conditions under which a Dirac semimetallic state may emerge in the SDW phase of iron pnictides.

Following the identification of such a state, we further examine the possibility of topological semimetallic phases with spin-orbit coupling (SOC) present, utilizing a tight-binding model augmented by Hubbard interactions in a 2D antiferromagnetically (AFM) ordered system. A comprehensive theoretical analysis also necessitates the study of collective excitations, which provide essential insights into the interplay between electronic correlations and band structure.

A central focus of our investigation is the role of crystal symmetries, particularly non-symmorphic symmetries, in protecting the Dirac nodes and maintaining the persistence of a semimetallic phase in a checkerboard antiferromagnetic order. By analyzing both quasiparticle interference patterns and optical conductivity, we aim to elucidate how the interplay of electronic correlations and band structure topology helps to gain a comprehensive understanding of the electronic states. Thus, the present study seeks to provide a complete and detailed understanding of the emergence, electronic states, and excitation spectra of topological semimetals in magnetically ordered systems, contributing to the broader search for materials with exotic topological properties and potential technological applications.

1.11 Problem Statement

1. **To explore the possibility of topological semimetallic states within correlated electron models, which supports conventional magnetic orderings such antiferromagnetism, stripe order, etc.:** This objective aims to theoretically explore the parameter space of magnetically ordered states in order to identify possible realization of topological semimetallic phases within correlated electron framework such as the multi-orbital Hubbard model. Specifically, we analyze two cases: (i) an antiferromagnetic spin configuration on a square lattice, i.e., (π, π) ordering and (ii) a striped spin-density-wave (SDW)

state with $(\pi, 0)$ ordering. Furthermore, we investigate the role of spin–orbit coupling in non-symmorphic crystal on the emergence of the resulting semimetallic states.

2. **To study the collective excitations such as edge states, quasiparticle interference, optical conductivity, etc., in the magnetically ordered topological semimetallic systems:** A detailed theoretical analysis of a topological semimetallic state necessitates an exploration of collective excitations, which are crucial for determining the dynamical properties of a system. Specifically, charge dynamics are examined through the calculation of optical conductivity, providing insights into charge dynamics, many-body interaction effects, etc. Simultaneously, the study of quasiparticle interference (QPI) patterns is employed to probe the electronic structure and scattering processes at low energies, offering a window into the interplay between band topology and correlation effects. In addition to this, edge states are explored in the semimetallic state which provides an evidence of being a topological nature.

Bibliography

[1] Bloch F 1929 *Z. Physik* **52** 555.

[2] Bansil A, Lin H, and Das T 2016 *Rev. Mod. Phys.* **88** 021004

[3] Thouless D J, Kohmoto M, Nightingale M P, and Nijs den M 1982 *Phys. Rev. Lett.* **49** 405

[4] Wen X G 1995 *Advances in Physics* **44** 405

[5] Kane C L and Mele E J 2005b *Phys. Rev. Lett.* **95** 146802.

[6] Fu L, Kane C L, and Mele E J 2007 *Phys. Rev. Lett.* **98** 106803.

[7] Moore J E and Balents L 2007 *Phys. Rev. B* **75** 121306(R).

[8] Qi X. -L. and Zhang S. -C. 2011 *Rev. Mod. Phys.* **83** 1057

[9] Yan Y, Wang L -X, Yu D -P, Liao Z -M 2013 *Appl. Phys. Lett.* **103** 033106

[10] Dai X, Du Z Z, and Lu H -Z 2017 *Phys. Rev. Lett.* **119** 166601

[11] Novak M, Sasaki S, Segawa K, and Ando Y 2015 *Phys. Rev. B* **91** 041203(R)

[12] Xu Y, Gan Z, and Zhang S -C 2014 *Phys. Rev. Lett.* **112** 226801

[13] Nandy S, Sharma G, Taraphder A, and Tewari S 2017 *Phys. Rev. Lett.* **119** 176804

[14] Sadhukhan B and Nag T 2023 *Phys. Rev. B* **107** L081110

[15] Burkov A A and Kim Y B 2016 *Phys. Rev. Lett.* **117** 136602

[16] Huang X *et al* 2015 *Phys. Rev. X* **5** 031023

[17] Chang C -Z, Liu C -X, and MacDonald A H 2023 *Rev. Mod. Phys.* **95** 011002

[18] Shiomi Y, Nomura K, Kajiwara Y, Eto K, Novak M, Segawa K, Ando Y, and Saitoh E 2014 *Phys. Rev. Lett.* **113** 196601

[19] Nakahara M 1990 *Geometry, topology and physics* (2nd ed.) CRC Press

[20] Basu S 2023 *Topological phases in condensed matter physics,* Springer

[21] Hasan M Z and Kane C L 2010 *Rev. Mod. Phys.* **82** 3045

[22] Bernevig B A, Hughes T A, and Zhang S C 2006 *Science* **314** 1757

[23] König M, Wiedmann S, Brne C, Roth A, Buhmann H, Molenkamp L W, Qi X L, and Zhang S C 2007 *Science* **318** 766.

[24] Roth A, Brüne C, Buhmann H, Molenkamp L W, Maciejko J, Qi X -L, and Zhang S -C 2009 *Science* **325** 294.

[25] Hsieh D, Qian D, Wray L, Xia Y, Hor Y S, Cava R J, and Hasan M Z 2008 *Nature* **452** 970.

[26] Burkov A A 2016 *Nature Mater.* **15** 1145.

[27] Fang C, Weng H, Dai X, and Fang Z 2016 *Chinese Phys. B* **25** 117106

[28] Regmi S *et al* 2024 *Phys. Rev. Materials* **8** L041201

[29] Sato M and Ando Y 2017 *Rep. Prog. Phys.* **80** 076501

[30] Chiu C -K and Schnyder A P 2014 *Phys. Rev. B* **90** 205136

[31] Zhao Y X, Schnyder A P, and Wang Z D 2016 *Phys. Rev. Lett.* **116** 156402

[32] Young S M, Zaheer S, Teo J C Y, Kane C L, Mele E J, and Rappe A M 2012 *Phys. Rev. Lett.* **108** 140405

[33] Zhao Y X and Schnyder A P 2016 *Phys. Rev. B* **94** 195109

[34] Young S M and Kane C L 2015 *Phys. Rev. Lett.* **115** 126803

[35] Yang B -J, Bojesen T A, Morimoto T, and Furusaki A 2017 *Phys. Rev. B* **95** 075135

[36] Gao H, Venderbos Jörn W F, Kim Y, and Rappe A M 2019 *Annu. Rev. Mater. Res.* **49** 153

[37] Lundgren R, Laurell P, and Fiete G A 2014 *Phys. Rev. B* **90** 165115

[38] Wang Q *et al* 2017 *Nano Letters* **17** 834

[39] Li P *et al* 2018 *Nat. Commun.* **9** 3990

[40] Mondal S, Ganguly S, and Basu S 2022 *Phys. Sci. Rev.* **9** 497

[41] Zhang M, Wang X, Song F, and Zhang R 2019 *Adv. Quantum Technol.* **2** 1800039

[42] Armitage N P, Mele E J, and Vishwanath A 2018 *Rev. Mod. Phys.* **90** 015001

[43] Wadhwa P, Kumar T J D, Shukla A, and Kumar R 2020 *J. Phys.: Condens. Matter* **32** 395703

[44] Wadhwa P, Kumar T J D, Shukla A, and Kumar R 2022 *Solid State Commun.* **358** 114976

[45] Mutch J, Chen W -C, Went P, Qian T, Wilson I Z, Andreev A, Chen C -C, Chu J -H 2019 *Sci. Adv.* **5(8)** eaav9771

[46] Murakami S 2007 *New J. Phys.* **9** 356

[47] Chiu C -K, Teo J C Y, Schnyder A P, and Ryu S 2016 *Rev. Mod. Phys.* **88** 035005

[48] Michel L and Zak J 1999 *Phys. Rev. B* **59** 5998

[49] Furusaki A 2017 *Science Bulletin* **62** 788

[50] Zhang J, Chan Y -H, Chiu C -K, Vergniory M G, Schoop L M, and Schnyder A P 2018 *Phys. Rev. Materials* **2** 074201

[51] Chan Y -H, Kilic B, Hirschmann M M, Chiu C -K, Schoop L M, Joshi D G, and Schnyder A P 2019 *Phys. Rev. Materials* **3** 124204

[52] Bradley C J and Cracknell A P, *The Mathematical Theory of Symmetry in Solids* (Clarendon Press Oxford, 1972).

[53] Yan B and Felser C 2017 *Annu. Rev. Condens. Matter Phys.* **8** 337

[54] Xu S Y *et al* 2015 *Science* **349** 613

[55] Lv B Q *et al* 2015 *Nat. Phys.* **11** 724

[56] Yang K -Y, Lu Y -M, and Ran Y 2011 *Phys. Rev. B* **84** 075129

[57] Liu E *et al* 2018 *Nat. Phys.* **14** 1125

[58] Wang Q *et al* 2018 *Nat. Commun.* **9** 3681

[59] Nakatsuji S, Kiyohara N, and Higo T 2015 *Nature 527* 212

[60] Kiyohara N, Tomita T, and Nakasuji S 2016 *Phys. Rev. Applied* **5** 064009

[61] Sinha I, Dutta P, Firdosh N, Sinha S, Ganguli N, and Manna S 2025 *J. Phys.: Condens. Matter* **37** 265001

[62] Berry M V 1984 *Proc. R. Soc. Lond. A* **392** 45

[63] Shapere A and Wilczek F *Geometric Phases in Physics* (World Scientific, Singapore, 1989)

[64] Xiao D, Chang M -C, and Niu Q 2010 *Rev. Mod. Phys.* **82** 1959

[65] Halperin B I 1982 *Phys. Rev. B* **25** 2185

[66] Wu C, Bernevig B A, and Zhang S -C 2006 *Phys. Rev. Lett.* **96** 106401

[67] Chen W, Deng W -Y, Hou J -M, Shi D N, Sheng L, and Xing D Y 2016 *Phys. Rev. Lett.* **117** 076802

[68] Lau A and Timm C 2013 *Phys. Rev. B* **88** 165402

[69] Fertig H A and Brey L 2006 *Phys. Rev. Lett.* **97** 116805

[70] Lado J L, García-Martínez N and Fernández-Rossier J 2015 *Synth. Met.* **210** 56

[71] Matveeva P G, Aristov D N, Meidan D, and Gutman D B 2019 *Phys. Rev. B* **99** 075409

[72] Yao W, Yang S A, and Niu Q 2009 *Phys. Rev. Lett.* **102** 096801

[73] Nakada K, Fujita M, Dresselhaus G and Dresselhaus M S 1996 *Phys. Rev. B* **54** 17954

[74] Wakabayashi K, Fujita M, Ajiki H and Sigrist M 1999 *Phys. Rev. B* **59** 8271

[75] Lado J L, Fernández-Rossier J 2022 arXiv:2210.07568

[76] Castro Neto A H, Guinea F, Peres N M R, Novoselov K S and Geim A K 2009 *Rev. Mod. Phys.* **81** 109

[77] McCann E 2012 arXiv:1205.4849

[78] Kane C L and Mele E J 2005 *Phys. Rev. Lett.* **95** 226801.

[79] Haldane F D M 1988 *Phys. Rev. Lett.* **61**

[80] Guan S, Liu Y, Yu Z -M, Wang S -S, Yao Y and Yang S A 2017 *Phys. Rev. Mater.* **1** 054003

[81] Li S, Liu Y, Wang S -S, Yu Z -M, Guan S, Sheng X L, Yao Y and Yang S A 2018 *Phys. Rev. B* **97** 045131

[82] Sato T *et al* 2018 *Phys. Rev. B* **98** 121111

[83] Liu Z K *et al* 2014 *Science* **343** 864

[84] Liu Z K *et al* 2014 *Nat. Mater.* **13** 677

[85] Borisenko S, Gibson Q, Evtushinsky D, Zabolotnyy V, Büchner B and Cava R J 2014 *Phys. Rev. Lett.* **113** 027603

[86] Yang B J and Nagaosa N 2014 *Nat. Commun.* **5** 4898

[87] Wang J 2017 *Phys. Rev. B* **95** 115138

[88] Tang P, Zhou Q, Xu G and Zhang S -C 2016 *Nat. Phys.* **12** 1100

[89] Young S M and Wieder B J 2017 *Phys. Rev. Lett.* **118** 186401

[90] Li S, Liu Y, Yu Z -M, Jiao Y, Guan S, Sheng X L, Yao Y and Yang S A 2019 *Phys. Rev. B* **100** 205102

[91] Park J *et al* 2011 *Phys. Rev. Lett.* **107** 126402

[92] Lee G, Farhan M A, Kim J S and Shim J H 2013 *Phys. Rev. B* **87** 245104

[93] Guo Y F, Princep A J, Zhang X, Manuel P, Khalyavin D, Mazin I I, Shi Y G and Boothroyd A T 2014 *Phys. Rev. B* **90** 075120

[94] Wang A, Zaliznyak I, Ren W, Wu L, Graf D, Garlea V O, Warren J B, Bozin E, Zhu Y and Petrovic C 2016 *Phys. Rev. B* **94** 165161

[95] Masuda H *et al* 2016 *Sci. Adv.* **2** e1501117

[96] Pournaghavi N, Islam M F, Islam R, Autieri C, Dietl T, and Canali C M 2021 *Phys. Rev. B* **103** 195308

[97] Islam R, Mardanya S, Lau A, Cuono G, Chang T -R, Singh B, Canali C M, Dietl T, and Autieri C 2023 *Phys. Rev. B* **107** 125102

[98] Guo Z, Liu Y, Jiang H, Zhang X, Jin L, Liu C, and Liu G 2023 *Mater. Today Phys.* **36** 101153

[99] Rai V, Stunault A, Schmidt W, Jana S, Perßon1 J, Soh J -R, Brückel Th, and Nandi S 2023 *Phys. Rev. B* **107** 184413

[100] Kikugawa N, Uji S, and Terashima T 2024 *Phys. Rev. B* **109** 035143

[101] Ong N P and Liang S 2021 *Nat. Rev. Phys.* **3** 394

[102] Sharma G, Goswami P, and Tewari S 2017 *Phys. Rev. B* **96** 045112

[103] Okamura Y *et al* 2020 *Nat. Commun.* **11** 4619

[104] Li P *et al* 2018 *Nat. Commun.* **9** 3990

[105] Fan Y *et al* 2014 *Nat. Mater.* **13** 699

[106] Yasuda K, Tsukazaki A, Yoshimi R, Takahashi K S, Kawasaki M, and Tokura Y 2016 *Phys. Rev. Lett.* **117** 127202

[107] Chorsi H, Cheng B, Zhao B, Toudert J, Asadchy V, Shoron O F, Fan S, and Matsunaga R 2022 *Adv. Funct. Mater.* **32** 2110655

[108] Kamihara Y, Watanabe T, Hirano M, and Hosono H 2008 *J. Am. Chem. Soc.* **130** 3296

[109] Ren Z A *et al* 2008 *Chin. Phys. Lett.* **25** 2215

[110] Si Q, Yu R, and Abrahams E 2016 *Nat. Rev. Mater.* **1** 16017

[111] Boeri L, Dolgov O V, and Golubov A A 2008 *Phys. Rev. Lett.* **101** 026403

[112] Crivelli D and Ptok A 2014 *Acta Phys. Pol. A* **126** A-16

[113] Martinelli A, Bernardini F, and Massidda S 2016 *C. R. Physique* **17** 5

[114] Raghu S, Qi X -L, Liu C -X, Scalapino D J, and Zhang S -C 2008 *Phys. Rev. B* **77** 220503(R)

[115] Graser S, Maier T A, Hirschfeld P J, and Scalapino D J 2010 *New J. Phys.* **11** 025016

[116] Brydon P M R, Daghofer M and Timm C 2011 *J. Phys.: Condens. Matter* **23** 246001

[117] Hasan M Z and Bernevig B A 2010 *Physics* **3** 27

[118] Ran Y, Wang F, Zhai H, Vishwanath A, and Lee D -H 2009 *Phys. Rev. B* **79** 014505

[119] Watson M D *et al* 2019 *npj Quantum Mater.* **4** 36

[120] Richard P 2010 *Phys. Rev. Lett.* **104** 137001

[121] Morinari T, Kaneshita E, and Tohyama T 2010 *Phys. Rev. Lett.* **105** 037203

[122] Huynh J, Tanabe Y, and Tanigaki K 2011 *Phys. Rev. Lett.* **106** 217004

[123] Wang Z, Sun Y, Chen X -Q, Franchini C, Xu G, Weng H, Dai X, and Fan Z 2012 *Phys. Rev. B* **85** 195320

[124] Mazin I I and Schmalian J 2009 Physica C **469** 614

[125] Si Q and Abrahams E 2008 *Phys. Rev. Lett.* **101** 076401

[126] Zhang P *et al* 2019 *Nat. Phys.* **15** 41

[127] Fu L and Kane C L 2008 *Phys. Rev. Lett.* **100** 096407

[128] Mourik V, Zuo K, Frolov S M, Plissard S R, Bakkers E P A M, and Kouwenhoven L P 2012 *Science* **336** 1003

[129] Zhang P *et al* 2018 *Science* **360** 182

[130] Xu G, Lian B, Tang P, Qi X -L, and Zhang S -C 2016 *Phys. Rev. Lett.* **117** 047001

[131] Auerbach A *Interacting Electrons and Quantum Magnetism* (Springer, New York, 1994)

[132] Sachdev S *Quantum Phase Transitions*, 2nd ed. (Cambridge University Press, 2011)

[133] Li Q N, Vasilopoulos P, Peeters F M, Xu W, Xiao Y M, and Milošević M V 2024 *Phys. Rev. B* **109** 115123

[134] Srivatsa N S and Ganesh R 2018 *Phys. Rev. B* **98** 165133

[135] Maciejko J and Nandkishore R 2014 *Phys. Rev. B* **90** 035126

[136] Elnaggar H, Nag A, Haverkort M W, Garcia-Fernandez M, Walters A, Wang R P, Zhou K J, de Groot F 2023 *Nat. Commun.* **12** 14(1)

[137] Yan Z -M, Li Z -X, Wang X -G, Han X, and Guo G -H 2025 *Phys. Rev. B* **112** 094441

[138] Hoffmann A 2021 *J. Magn. Magn. Mater.* **539** 168391

[139] Knowles P, Yang B, Muramatsu T, Moulding O, Buhot J, Sayers C J, Como E Da, and Friedemann S 2020 *Phys. Rev. Lett.* **124** 167602

[140] Jin J -T, Jiang K, Yao H, and Zhou Y 2022 *Phys. Rev. Lett.* **129** 167001

[141] Kreisel A, Choubey P, Berlijn T, Ku W, Andersen B M, and Hirschfeld P J 2015 *Phys. Rev. Lett.* **114** 217002

[142] Hoffman J E, McElroy K, Lee D -H, Lang K M, Eisaki H, Uchida S, and Davis J C 2002 *Science* **297** 1148

[143] Chuang T -M, Allan M P, Lee J, Xie Y, Ni N, Bud'ko S L, Boebinger G S, Canfield P C, and Davis J C 2010 *Science* **327** 181

[144] Knolle J, Eremin I, Akbari A, and Moessner R 2010 *Phys. Rev. Lett.* **104** 257001

[145] A V Pronin and M Dressel 2021 *Phys. Status Solidi B* **258** 2000027 (2021).

[146] Valenzuela B, Calderón M J, León G and Bascones E 2013 *Phys. Rev. B* **87** 075136

[147] Singh N, Saini S M, Nautiyal T, and Auluck S 2007 *Physica B* **388** 99

[148] Dagotto E 1994 *Rev. Mod. Phys.* **66** 763

[149] Xu S X, Pi H Q, Li R S, Hu T C, Wu Q, Wu D, Weng H M, and Wang N L 2022 *Phys. Rev. B* **106** 115121

[150] Chen R Y, Zhang S J, Schneeloch J A, Zhang C, Li Q, Gu G D, and Wang N L 2015 *Phys. Rev. B* **92** 075107

Chapter 2

TSM state in a non-symmorphic crystal with AFM order

In this chapter, we examine the possible existence of a topological semimetal with AFM order in a two-dimensional square lattice with a nonsymmorphic symmetry by using a Hartree-Fock meanfield theory within the Hubbard model discussed in the beginning of the chapter. We locate the region in the second-neighbor spin-orbit coupling vs interaction phase diagram, where such a state is obtained. Finally, the effect of an in-plane magnetic field-like term in obtaining Weyl points is also discussed. The nature of edge states in the ribbon geometry in the topological states is also explored.

2.1 The Hubbard model

The Hubbard model [1] provides a fundamental and widely used framework for investigating the effects of electronic correlations. It offers a relatively simple yet powerful approach to understanding how electron-electron interactions can lead to phenomena such as magnetic ordering, insulating behavior, and other emergent phases, which cannot be adequately captured by the conventional tight-binding model.

In modeling a solid, it is common to treat the atomic nuclei as stationary due to their significantly larger mass compared to electrons. The electrons, on the other hand, move within the potential created by the screened Coulomb fields of the fixed nuclei. While real atoms possess complex electronic structure with several energy levels, a considerable simplification one can think of is the one with a single energy level. In this scenario, governed by the Pauli exclusion principle, each level can accommodate at most two electrons with opposite spins. The dominant interaction in such a setup is the on-site Coulomb repulsion, characterized by the parameter U, representing the energy cost associated with double occupancy [2].

Within this framework, the Hubbard Hamiltonian can be written in terms of electron creation and annihilation operators as:

$$H = -t \sum_{\langle \mathbf{i},\mathbf{j} \rangle,\sigma} c^{\dagger}_{\mathbf{i}\sigma} c_{\mathbf{j}\sigma} + U \sum_{\mathbf{i}} n_{\mathbf{i}\uparrow} n_{\mathbf{i}\downarrow} - \mu \sum_{\mathbf{i}} (n_{\mathbf{i}\uparrow} + n_{\mathbf{i}\downarrow}). \tag{2.1.1}$$

This consists of three distinct contributions. The first term accounts for the kinetic energy due to electron hopping between neighboring lattice sites, with the amplitude t determined by the overlap of electronic wavefunctions on adjacent atoms. Given that atomic wavefunctions decay exponentially with distance, electron hopping is predominantly restricted to nearest neighbors, although longer-range hopping may occur depending on the lattice geometry and interaction details.

The second term represents the on-site Coulomb interaction, which contributes only when a site is occupied by two electrons with opposite spins; it vanishes for empty or singly occupied sites. The third term involves the chemical potential μ, which controls the overall electron filling in the lattice. In the non-interacting limit ($U = 0$), the Hubbard model reduces to the tight-binding model and describes a metallic state. In the opposite limit ($t = 0$), electrons are localized, resulting in an insulating phase. Therefore, the interplay between t and U governs the rich phase diagram observed in correlated electron systems [2].

Additionally, by performing the particle-hole transformation defined as $a^{\dagger}_{\mathbf{i}\sigma} a_{\mathbf{i}\sigma} = 1 - c^{\dagger}_{\mathbf{i}\sigma} c_{\mathbf{i}\sigma}$, the Hamiltonian can be expressed in an alternative symmetric form:

$$H_h = -t \sum_{\langle \mathbf{i},\mathbf{j} \rangle, \sigma} a^{\dagger}_{\mathbf{i}\sigma} a_{\mathbf{j}\sigma} + U \sum_{\mathbf{i}} n_{\mathbf{i}\uparrow} n_{\mathbf{i}\downarrow}, \tag{2.1.2}$$

which highlights the intrinsic particle-hole symmetry of the system, an important feature that plays a key role in analyzing the behavior of correlated electrons.

2.2 Rashba spin-orbit coupling

Spin-orbit coupling (SOC) is fundamentally a relativistic interaction that manifests as the entanglement between an electron's spin and its orbital motion. This coupling significantly impacts the magnetic and transport properties of materials and is a key factor in the realization of a variety of non-trivial quantum phases in condensed matter systems.

In two-dimensional (2D) heterostructures, particularly at their interfaces, the absence of inversion symmetry leads to a specific type of spin-orbit interaction known as *Rashba spin-orbit coupling* (Rashba SOC). This type of spin-orbit coupling is a characteristic feature of systems that lack a center of inversion and is linearly dependent on the crystal momentum $\mathbf{k}$. It lifts the spin degeneracy of electronic bands, thereby exerting a pronounced influence on the magnetic and transport behavior of the system and enabling the realization of several exotic phenomena.

This spin splitting is experimentally observed at certain metallic surfaces and can

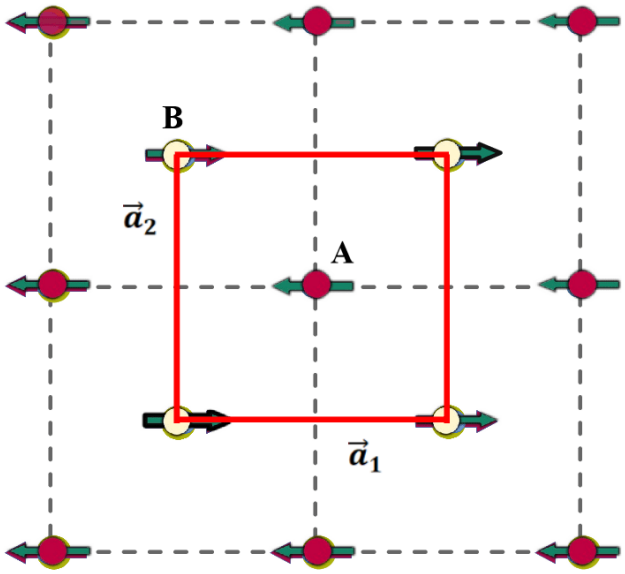

Figure 2.1: AFM lattice arrangement with 2 atoms per unit cell (shown in red square) having sublattices A and B with magnetic moments aligned along x-direction whose lattice vectors are $\vec{a}_1 = (1, 0, 0)$ and $\vec{a}_2 = (0, 1, 0)$, respectively. The A(B) atoms are displaced along $+z(-z)$ directions by a tiny fraction of the lattice vector to make the crystal non-symmorphic. The red (yellow) circles show the atoms lying above (below) the plane.

be understood as resulting from the coupling between an electron's motion and the electric field gradient encountered at an interface lacking inversion symmetry. Unlike in centrosymmetric materials, where SOC arises predominantly from atomic $(\mathbf{L} \cdot \mathbf{S})$ coupling within the d- and f-orbitals of transition metals, Rashba SOC is intrinsically linked to structural asymmetry and interface effects.

In a 2D antiferromagnetically ordered system, SOC can be originated in a crystal having non-symmorphic symmetry. For this, we consider a square lattice as shown in Fig. 2.1 with a single orbital per site. The unit cell has two atoms placed in an AFM arrangement with the lattice vectors denoted by $\vec{a_1} = (1, 0, 0)$ and $\vec{a_2} = (0, 1, 0)$, respectively. In order to make the lattice non-symmorphic, the atoms in the unit cell namely A and B are displaced along $+z$ and $-z$ directions, respectively, by a tiny but equal fraction of the lattice vector. This atomic arrangement allows next-nearest-neighbor SOC, whose expression can be written as [3, 4]:

$$H_\lambda = i\lambda \sum_{\mathbf{i}} \sum_{\sigma\sigma'} (\nu_{\mathbf{i},\mathbf{i}+\delta'\sigma} a^\dagger_{\mathbf{i}\sigma} a_{\mathbf{i}+\delta'\sigma'} \sigma_{\sigma\sigma'} + h.c.) \tag{2.2.1}$$

where $\delta' = +\hat{x}$ or $+\hat{y}$. λ is the SOC parameter and $\nu_{\mathbf{i},\mathbf{i}+\delta'}$ = -$\nu_{\mathbf{i}+\delta',\mathbf{i}} = \pm 1$ depending on the orientation of two next-nearest neighboring bonds whereas the nearest neighbor

SOC is ignored.

To investigate the antiferromagnetic Dirac semimetal state, we employ a two-dimensional tight-binding Hamiltonian that includes both spin-orbit coupling and Hubbard interactions, expressed as

$$H = H_h + H_\lambda \tag{2.2.2}$$

The hopping parameter t in H_h is set to be unity throughout unless mentioned otherwise. In this study, we consider only nearest-neighbor hopping, as including second-neighbor hopping would break particle-hole symmetry and result in the two Dirac points appearing at different energies.

2.3 Mean-field Methodology

A Hamiltonian that is quadratic in the creation and annihilation operators can be diagonalized straightforwardly using a unitary transformation, allowing the energy spectrum to be determined directly. However, the number operator $n_{\mathbf{i}\sigma} = c^\dagger_{\mathbf{i}\sigma} c_{\mathbf{i}\sigma}$ appearing in the second term of the above Hamiltonian, see Eq. 2.1.2, is quartic in the electron operators, significantly complicating the solution process. To overcome this difficulty, we employ Hartree-Fock mean-field approximation to decouple the quartic terms into an effective quadratic form.

The term $U n_{\mathbf{i}\uparrow} n_{\mathbf{i}\downarrow}$ can alternatively be represented in the rotationally invariant form in the following manner [5],

$$U n_{\mathbf{i}\uparrow} n_{\mathbf{i}\downarrow} = \frac{U}{4}(n_{\mathbf{i}})^2 - U S^2_{\mathbf{i}z} = \frac{U}{4}(n_{\mathbf{i}})^2 - U(S^2_{\mathbf{i}\mu} \cdot \hat{\Omega}_{\mathbf{i}})^2 \tag{2.3.1}$$

where the spin operator $S_{\mathbf{i}\mu} = \frac{1}{2}\sum_{\alpha\beta} c^\dagger_{\mathbf{i}\alpha} \sigma^\mu_{\alpha\beta} c_{\mathbf{i}\beta}$. σ^μ denotes μ^{th}-component of Pauli matrices and $\mu = \{x, y, z\}$. $\hat{\Omega}_{\mathbf{i}}$ is an arbitrary unit vector in 3D space. Also, $(S^2_{\mathbf{i}\mu} \cdot \hat{\Omega}_{\mathbf{i}})^2 = (S_{\mathbf{i}x})^2 = (S_{\mathbf{i}y})^2 = (S_{\mathbf{i}z})^2$. The number operator $n_{\mathbf{i}} = n_{\mathbf{i}\uparrow} + n_{\mathbf{i}\downarrow}$.

The first term in the above equation is a scalar as we assume constant charge density and is therefore absorbed into the chemical potential.

The fundamental idea underpinning the mean-field approach is that each electron experiences an average potential generated by the presence of all other electrons. Consequently, the motion and properties of an individual electron are modified relative to those of a free particle. In this approximation, the spin operator is expressed as the sum of its expectation value and the fluctuation around the mean:

$$S_{\mathbf{i}\mu} = \langle S_{\mathbf{i}\mu} \rangle + (S_{\mathbf{i}\mu} - \langle S_{\mathbf{i}\mu} \rangle) \tag{2.3.2}$$

Using this assumption in (2.3.1) and ignoring the first term, the mean-field Hamiltonian takes the form:

$$H_{im} = -U \sum_{\mu} (S_{\mathbf{i}\mu})^2 \approx -U \sum_{\mu} (2\langle S_{\mathbf{i}\mu}\rangle S_{\mathbf{i}\mu} - \langle S_{\mathbf{i}\mu}\rangle^2) \tag{2.3.3}$$

assuming the fluctuations are small enough that their squared contributions can be neglected.

Defining the local spin magnetization $m_{\mathbf{i}}^{\mu}$ as

$$m_{\mathbf{i}}^{\mu} = \langle S_{\mathbf{i}\mu}\rangle = \frac{1}{2}\langle \Psi_{\mathbf{i}}^{\dagger} \sigma^{\mu} \Psi_{\mathbf{i}}\rangle \tag{2.3.4}$$

where $\Psi_{\mathbf{i}}^{\dagger} = (a_{\mathbf{i}\uparrow}^{\dagger}, a_{\mathbf{i}\downarrow}^{\dagger})$. So, we get

$$H_{im} = -2U \sum_{\mu} m_{\mathbf{i}}^{\mu} S_{\mathbf{i}\mu} + U \sum_{\mu} (m_{\mathbf{i}}^{\mu})^2 \tag{2.3.5}$$

Recalling the definition of spin operator $S_{\mathbf{i}\mu}$, the first term in the above expression can be expressed as $\sum_{\mu} m_{\mathbf{i}}^{\mu} S_{\mathbf{i}\mu} = \frac{1}{2}\Psi_{\mathbf{i}}^{\dagger}(\mathbf{m_i} \cdot \boldsymbol{\sigma})\Psi_{\mathbf{i}}$. Thus, the resulting mean-field Hamiltonian becomes

$$H_{im} = -U \sum_{\mathbf{i}} \Psi_{\mathbf{i}}^{\dagger}(\boldsymbol{\sigma} \cdot \mathbf{m_i})\Psi_{\mathbf{i}} + U \sum_{\mathbf{i}} \mathbf{m}_{\mathbf{i}}^2 \tag{2.3.6}$$

Redefining $\mathbf{m_i} \to \frac{\mathbf{m_i}}{2}$, we arrive at the final expression of the mean-field decoupled interaction Hamiltonian

$$H_{im} = -\frac{U}{2} \sum_{\mathbf{i}\sigma} \Psi_{\mathbf{i}}^{\dagger}(\boldsymbol{\sigma} \cdot \mathbf{m_i})\Psi_{\mathbf{i}} + \frac{U}{4} \sum_{\mathbf{i}} \mathbf{m}_{\mathbf{i}}^2 \tag{2.3.7}$$

When incorporated into the sublattice structure of the system with AFM order under consideration, the meanfield decoupled part with broken $\mathcal{P}$ and $\mathcal{T}$ becomes

$$H_{mf} = -\sum_{\mathbf{i}\alpha\beta} \tau a_{\mathbf{i}\alpha}^{\dagger}(\boldsymbol{\sigma} \cdot \boldsymbol{\Delta}_{\mathbf{i}})_{\alpha\beta} a_{\mathbf{i}\beta}, \tag{2.3.8}$$

where τ corresponds to the bipartite lattice space with sublattices denoted by A and B with spins aligned opposite to each other. $\tau = 1$ on A sublattice and -1 on B sublattice. $\boldsymbol{\Delta}_{\mathbf{i}}$ is the exchange field given by

$$2\boldsymbol{\Delta}_{\mathbf{i}} = U(m_{ix}\hat{x} + m_{iy}\hat{y} + m_{iz}\hat{z}). \tag{2.3.9}$$

m_{ix}, m_{iy}, and m_{iz} represent the components of magnetic moments, which are obtained

self consistently. $\hat{x}$, $\hat{y}$, and $\hat{z}$ are the unit vectors. The last term of H_{im} does not appear in H_{mf} as it is a scalar field and does not play any role in the self-consistent calculation. Thus, after Fourier transforming eqns. (2.1.2) and (2.2.1); and combining it with (2.3.9), the Hamiltonian in **k**-space can be written in the composite sublattice and spin basis as [6]

$$\begin{aligned}\mathcal{H}(\mathbf{k}) &= 4t\tau_1 \cos\frac{k_x}{2}\cos\frac{k_y}{2} + (\Delta_x - 2\lambda\sin k_y)\sigma_1 \otimes \tau_3 \\ &+ (\Delta_y + 2\lambda\sin k_x)\sigma_2 \otimes \tau_3 + \Delta_z\sigma_3 \otimes \tau_3, \end{aligned} \tag{2.3.10}$$

where σ and τ are Pauli matrices in the spin and sublattice spaces. The two-fold degenerate eigenvalues of the Hamiltonian can be readily shown to be

$$E_{\mathbf{k}} = \pm\sqrt{\varepsilon_{\mathbf{k}}^2 + \Delta_{x\mathbf{k}}'^2 + \Delta_{y\mathbf{k}}'^2 + \Delta_z^2}, \tag{2.3.11}$$

where $\varepsilon_{\mathbf{k}} = 4t\cos\frac{k_x}{2}\cos\frac{k_y}{2}$, $\Delta'_{x\mathbf{k}} = \Delta_x - 2\lambda\sin k_y$, $\Delta'_{y\mathbf{k}} = \Delta_y + 2\lambda\sin k_x$. The eigenvector $(\phi^A_{\mathbf{k}\uparrow},\ \phi^B_{\mathbf{k}\uparrow},\ \phi^A_{\mathbf{k}\downarrow},\ \phi^B_{\mathbf{k}\downarrow})^T$ of the Hamiltonian $\mathcal{H}(\mathbf{k})$ is used to obtain the magnetic moments in a self-consistent manner, where one electron per site is considered throughout. The components of magnetic moments at the sublattice A is [7]

$$\begin{aligned} m_z &= n^A_\uparrow - n^A_\downarrow \\ &= \sum_{\mathbf{k},l}(\phi^{A*}_{\mathbf{k}\uparrow}\phi^A_{\mathbf{k}\uparrow}\Theta(E_f - E_{\mathbf{k},\uparrow,\mathbf{l}}) - \phi^{A*}_{\mathbf{k}\downarrow}\phi^A_{\mathbf{k}\downarrow}\Theta(E_f - E_{\mathbf{k},\downarrow,\mathbf{l}})) \\ m_x &= \sum_{\mathbf{k},l}(\phi^{A*}_{\mathbf{k}\uparrow}\phi^A_{\mathbf{k}\downarrow} + \phi^A_{\mathbf{k}\uparrow}\phi^{A*}_{\mathbf{k}\downarrow})\Theta(E_f - E_{\mathbf{k},\uparrow,\mathbf{l}})\Theta(E_f - E_{\mathbf{k},\downarrow,\mathbf{l}}) \\ m_y &= \sum_{\mathbf{k},l}(-i\phi^{A*}_{\mathbf{k}\uparrow}\phi^A_{\mathbf{k}\downarrow} + i\phi^A_{\mathbf{k}\uparrow}\phi^{A*}_{\mathbf{k}\downarrow})\Theta(E_f - E_{\mathbf{k},\uparrow,\mathbf{l}})\Theta(E_f - E_{\mathbf{k},\downarrow,\mathbf{l}}), \end{aligned} \tag{2.3.12}$$

where l is the band index.

2.4 Phase Diagram

The energy dispersion given by (2.3.11) is gapped whenever the magnetic moments have a component along the z direction or along a direction in the x-y plane other than the x or y axes. However, there exists a two-fold degenerate band crossing at $E_k = 0$ provided that the magnetic moments are oriented either along the x or y direction. In these cases, the energy dispersions are linear in the vicinity of the band crossing. As discussed later, these band crossings correspond to Dirac cones and they

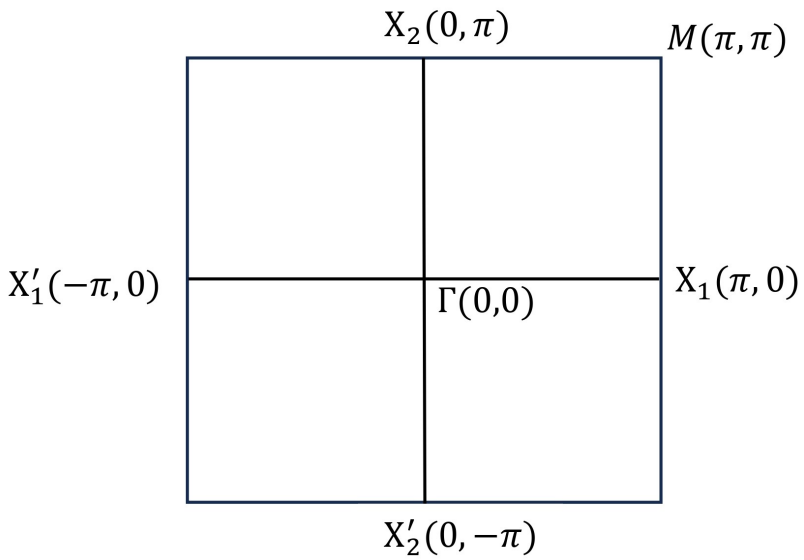

Figure 2.2: 2D Brillouin zone in a square lattice highlighting the high-symmetry points.

have non-trivial band topology. These DPs are protected by glide mirror symmetry $\{M_{\hat{x}}|\frac{1}{2}0\}$ and $\{M_{\hat{y}}|0\frac{1}{2}\}$ depending on whether the magnetic moments are oriented along x and y, respectively [6].

Fig. 2.3 shows the self-consistently obtained phase diagram in the λ-U parameter space when the magnetic moments are aligned along the x direction. Three different phases are obtained; DSM without magnetic order, DSM with AFM order, and a normal insulator with AFM order. It may be noted that the magnetic-order parameter vanishes in the DSM-NM state found in the small U but large λ region. Thus, there is no order parameter associated with this phase and both inversion and time-reversal symmetry are intact and DPs are protected by the nonsymmorphic symmetries. However, the magnetic-order paramater is non zero and time-reversal symmetry is broken in the DSM state with AFM order (AFM-DSM) as well as in the normal insulator with AFM order (AFM-I). The latter two are differentiated only by a condition based on the relative strength of magnetic-moment dependent exchange coupling and SOC, which is discussed later in this paragraph. Unlike in the symmorphic system, there is no further reduction in the translational symmetry originating from the sublattice structure associated with AFM ordering of magnetic moments. This is because the atoms in the sublattices A and B are displaced by a tiny fraction of lattice vector in a direction perpendicular to the plane of the two-dimensional system in the original model itself (Fig. 2.1). The DSM state with AFM order is obtained only for a very narrow window of SOC centered around $\lambda \sim 0.8$, which is sandwiched in between the DSM state without magnetic ordering and the AFM insulating state (AFM-I). The

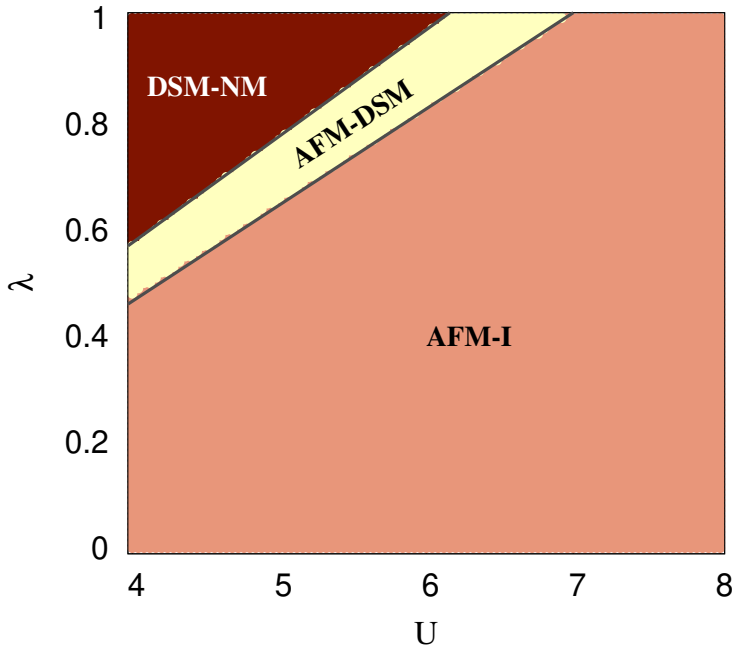

Figure 2.3: Phase diagram in the $\lambda - U$ space in the range $4 \leq U \leq 8$ and $0 \leq \lambda \leq 1.0$ at half-filling ($n = 1.0$). DSM state with AFM order is obtained only for a very narrow range of λ which separates the DSM state without magnetic order (DSM-NM) and the AFM insulating state (AFM-I).

DPs occur at the momenta $\mathbf{k} = (\pi, k_{y0})$ and $(\pi, \pi - k_{y0})$ with $\sin k_{y0} = \Delta_x/2\lambda$ [6]. Therefore, whenever the self-consistently obtained exchange field satisfies the condition $0 < \Delta_x \leq 2\lambda$, the AFM-DSM state is obtained, $\Delta_x = 0$ corresponds to DSM-NM state, and $\Delta_x \geq 2\lambda$ is satisfied in the AFM-I state.

Fig. 2.4 shows the electronic dispersion in the three phases for a fixed Coulomb interaction parameter $U = 5.0$ and different values of SOC parameter λ. In Fig. 2.4(a), the bulk dispersion is obtained for $\lambda = 0.4$ corresponding to the normal insulating state with AFM order indicated by a gap opening at the Fermi level. The gap opening disappears when SOC is increased and two DPs appear along X_1-M but they are located away from the high-symmetry points X_1 and M (Fig. 2.4(b)), where the high-symmetry points X_1, X_2, M, etc., in the first BZ, are shown in Fig. 2.2. The energy dispersion in the vicinity of DPs can be obtained from (2.3.11), which is

$$E_k = \pm 2\sqrt{(\lambda^2 + t^2 \cos^2 k_{y0}/2)q_x^2 + (\lambda^2 \cos^2 k_{y0})q_y^2}. \tag{2.4.1}$$

These DPs are protected by glide mirror symmetry $\{M_{\hat{x}}|\frac{1}{2}0\}$ while the dispersion in their vicinity is independent of magnetic moment. For $\lambda = 1.0$ (Fig. 2.4(c)), the magnetic moment vanishes, therefore, three DPs are obtained at the time-reversal invariant momenta, i.e., $X_1(\pi, 0)$, $M(\pi, \pi)$ and $X_2(0, \pi)$ of the Brillouin-zone boundary.

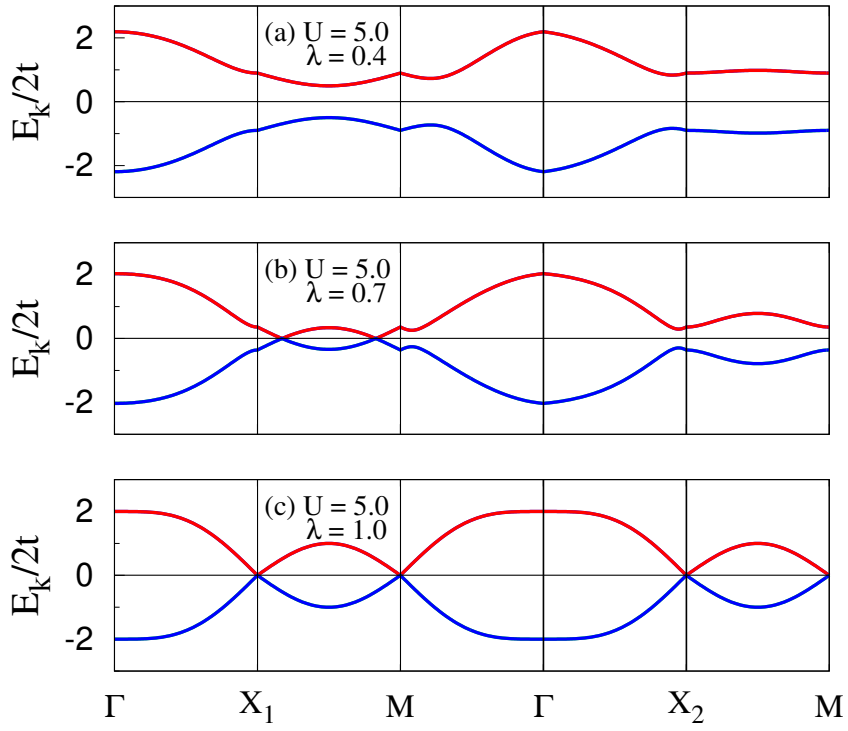

Figure 2.4: For $U = 5$, electronic dispersions are plotted when (a) $\lambda = 0.4$, (b) $\lambda = 0.7$ and (c) $\lambda = 1.0$. For these three different values, normal insulator, DSM state with antiferromagnetic order and without any magnetic order are obtained, respectively. In each case, the DPs are protected by the non-symmorphic symmetries.

These DPs are protected either by the screw axes $\{C_{2\hat{x}}|\frac{1}{2}0\}$ and $\{C_{2\hat{y}}|0\frac{1}{2}\}$ or by glide mirror plane symmetry $\{M_{\hat{z}}|\frac{1}{2}\frac{1}{2}\}$ as the system has now both $\mathcal{T}$ and $\mathcal{P}$ symmetry intact in the absence of any magnetic moment [3].

2.5 Chern number

The topological charge i.e., the Chern number associated with DPs should vanish as the degenerate bands have opposite chirality. The Chern number can be calculated with the help of the Berry flux, which is same as the line integral of the Berry connection along the boundary of the BZ, which includes one of the DPs. Thus, the Berry flux is given by

$$\phi_n = \int_{BZ} \mathbf{B}_n(\mathbf{k}) \cdot d\mathbf{S} \tag{2.5.1}$$

where n is the band number. The berry curvature can be written in terms of Berry connection $\mathbf{A}_n(\mathbf{k})$ as

$$\mathbf{B}_n(\mathbf{k}) = \nabla \times \mathbf{A}_n(\mathbf{k}) \tag{2.5.2}$$

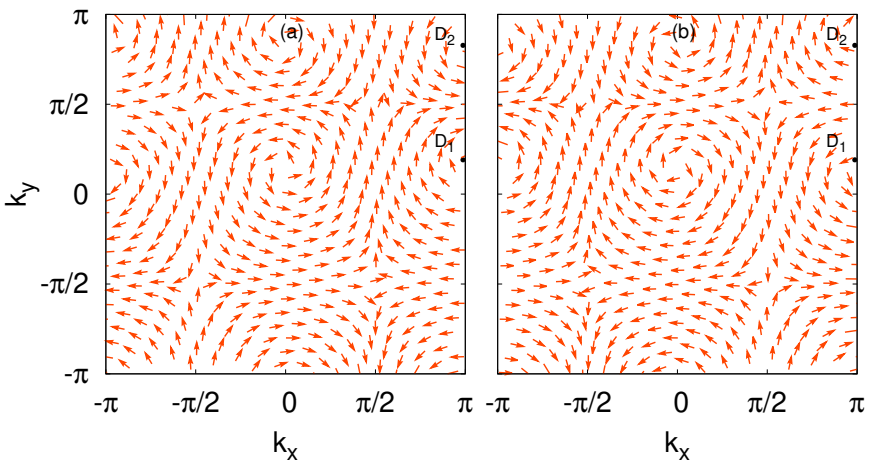

Figure 2.5: Berry connection plotted for the two individual bands in the whole Brillouin for the AFM-DSM state. The two DPs shown in Fig. 2.4(b) are denoted by D_1 and D_2. The Berry connection for the different but degenerate bands has opposite signs as indicated by the clockwise and counterclockwise rotations in the two plots.

or equivalently as a line integral due to Stoke's theorem. The Berry connection for the n^{th} band is

$$\mathbf{A}_n(\mathbf{k}) = i\langle\psi_{n\mathbf{k}}|\nabla_{\mathbf{k}}|\psi_{n\mathbf{k}}\rangle. \tag{2.5.3}$$

$\psi_{n\mathbf{k}}$ denotes the eigenfunctions of the Hamiltonian (2.3.10) for the n^{th} band.

Fig. 2.5(a) and (b) show the Berry connection plotted for the AFM-DSM state in the entire Brillouin zone. The rotation of the Berry connection for the two degenerate bands around each of DPs are opposite to each other whereas the chirality of one of the bands is -1 while for the other it is 1. Thus, the total Chern number vanishes for the degenerate bands, $\phi = \sum_n \phi_n = 0$ for each DPs.

2.6 Edge states

The edge states, in the topological insulators, are pairs of states with opposite spins propagating in directions opposite to each other. The dispersion of the edge state crosses the Fermi level and appears as a bridge between the bands corresponding to valence and conduction electrons [8]. They are also supported in systems such as Dirac and Weyl semimetals. There are numerous examples including the localized flat edge states in the quasi-one-dimensional graphene ribbons of zigzag shape [9–13]. While the edge states in graphene are attributed to the Dirac cones, these states may even be found in their absence when degeneracy occurs at high symmetry points [14, 16, 29]. Recent studies have explored the edge states in the Weyl semimetals without any magnetic order when the time-reversal symmetry is broken in the nonsymmorphic

system [17].

Here, we examine the edge-state dispersion in the Dirac semimetallic state with AFM order in quasi-one dimensional system. It may be noted that the nature of the edge state may depend on how the in-plane magnetic moments are oriented with respect to the ribbon length, as the four-fold rotation symmetry is broken. First, we consider a ribbon of width W lying along the y direction so that k_y becomes a good quantum number. The ribbon Hamiltonian H_{Rby} is constructed in the sublattice and spin basis as $(1A\uparrow, 1A\downarrow, 2B\uparrow, 2B\downarrow, \cdots)$, where the indices $1, 2, \cdots$ denote the chain numbers across the finite direction. The system is assumed to be finite along the x-axis and translationally invariant (infinite) along the y-axis, which renders the Hamiltonian pseudo-real.

To exploit the translational symmetry along y, the hopping and interaction terms in that direction are Fourier transformed, while the terms along the finite x-direction are retained in real space. This mixed representation leads to a block Hamiltonian of dimension $2W \times 2W$ where W is the number of atomic chains in the ribbon. The resulting Hamiltonian takes the form:

$$H_{Rby}(\mathbf{k}) = \begin{pmatrix} H_{1+} & H_2 & H_3 & O & \cdots \\ H_2^\dagger & H_{1-} & H_2 & H_3 & \cdots \\ H_3^\dagger & H_2^\dagger & H_{1+} & H_2 & \cdots \\ O & H_3^\dagger & H_2^\dagger & H_{1-} & \cdots \\ \vdots & \vdots & \vdots & \vdots & \ddots \end{pmatrix}, \tag{2.6.1}$$

where

$$H_{1\pm} = \begin{pmatrix} 0 & \pm(-2\lambda \sin k_y + \Delta_x) \\ \pm(-2\lambda \sin k_y + \Delta_x) & 0 \end{pmatrix},$$

$$H_2 = \begin{pmatrix} 2t\cos(k_y/2) & 0 \\ 0 & 2t\cos(k_y/2) \end{pmatrix}$$

and

$$H_3 = \begin{pmatrix} 0 & -\lambda \\ \lambda & 0 \end{pmatrix}.$$

$H_{1\pm}$ is the element in a matrix form of Hamiltonian corresponding to a single chain while H_2 and H_3 matrices connect a chain to the nearest and the next-nearest neighbor chains.

Fig. 2.6 shows the edge states obtained for three different cases when the number of chains is even. The results are the same for an odd number of chains. In the DSM

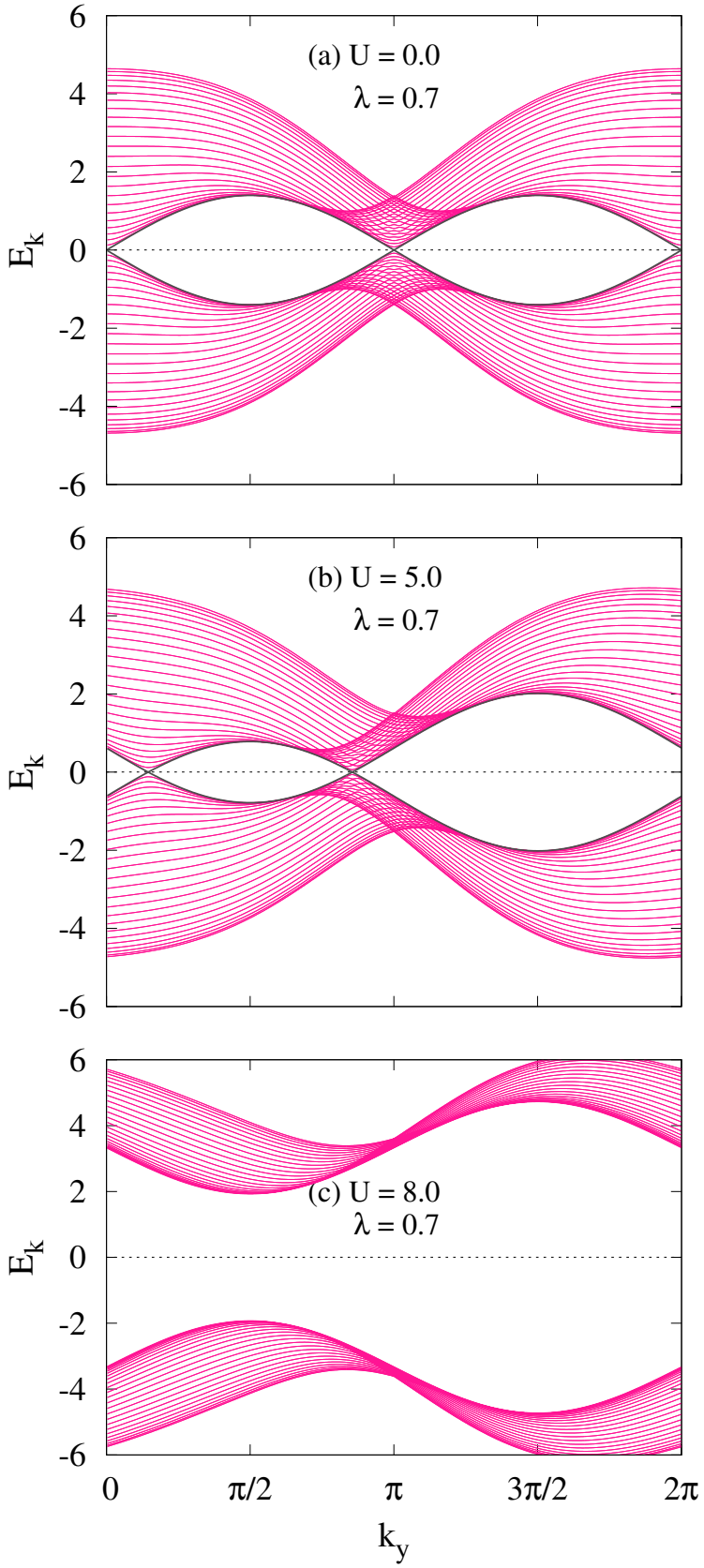

Figure 2.6: Edge-state dispersions and bulk bands for a ribbon of width $W = 50$ lying along y direction and projected onto a one-dimensional Brillouin zone for $\lambda = 0.7$ and (a) $U = 0.0$, (b) 5.0 and (c) 8.0. The edge-state dispersion crosses each other at the same points as the bulk bands at the Fermi level and disappear beyond U_s, which indicates appearance of a normal insulator.

state without AFM order, when the Hubbard interaction $U = 0$, the edge states cross the Fermi energy at $k_y = 0$, π and 2π. However, in the DSM state with AFM order, the crossing points shift away towards a point in between $k_y = 0$ and π. There exists a special U_s for a given value of λ, where the crossing coincides. Beyond that U_s, i.e., in the insulating state, there are no states crossing the Fermi energy, indicating the appearance of a normal insulator.

Next, we consider a ribbon of width W lying along the x-direction. The Hamiltonian matrix corresponding to this ribbon also has size $2W \times 2W$ and it is given by

$$H_{Rbx}(\mathbf{k}) = \begin{pmatrix} H'_{1+} & H'_2 & H'_3 & O & \cdots \\ H'^{\dagger}_2 & H'_{1-} & H'_2 & H'_3 & \cdots \\ H'^{\dagger}_3 & H'^{\dagger}_2 & H'_{1+} & H'_2 & \cdots \\ O & H'^{\dagger}_3 & H'^{\dagger}_2 & H'_{1-} & \cdots \\ \vdots & \vdots & \vdots & \vdots & \ddots \end{pmatrix}, \tag{2.6.2}$$

where

$$H'_{1\pm} = \begin{pmatrix} 0 & \pm(-2i\lambda \sin k_x + \Delta_x) \\ \pm(2i\lambda \sin k_x + \Delta_x) & 0 \end{pmatrix},$$

$$H'_2 = \begin{pmatrix} 2t\cos(k_x/2) & 0 \\ 0 & 2t\cos(k_x/2) \end{pmatrix}$$

and

$$H'_3 = \begin{pmatrix} 0 & i\lambda \\ i\lambda & 0 \end{pmatrix}.$$

$H'_{1\pm}$, H'_2 and H'_3 are matrices as described before except that now they are part of the Hamiltonian for a ribbon oriented along x axis.

Fig. 2.7 shows the edge states obtained when the chains as well as the magnetic moments are oriented along the x direction. In the DSM state without any AFM order, the nature of the edge state, as expected, is the same as the case when the ribbon was oriented along the y axis. However, we find that the edge state crosses the Fermi level at $k_x = \pi$ in the DSM state with AFM order. The location of the crossing does not change upon increasing U, which is not unusual as the DPs are found along high-symmetry direction for $k_x = \pi$ although the size of the magnetic moments increases with interaction. Finally, the crossing disappears at U_s and beyond.

It may be noted that there exists an anisotropy in the edge-state spectra in the x and y directions for a finite U. In the AFM-DSM state, the magnetic moments are aligned along the x-direction, which introduces directional anisotropy in the band-

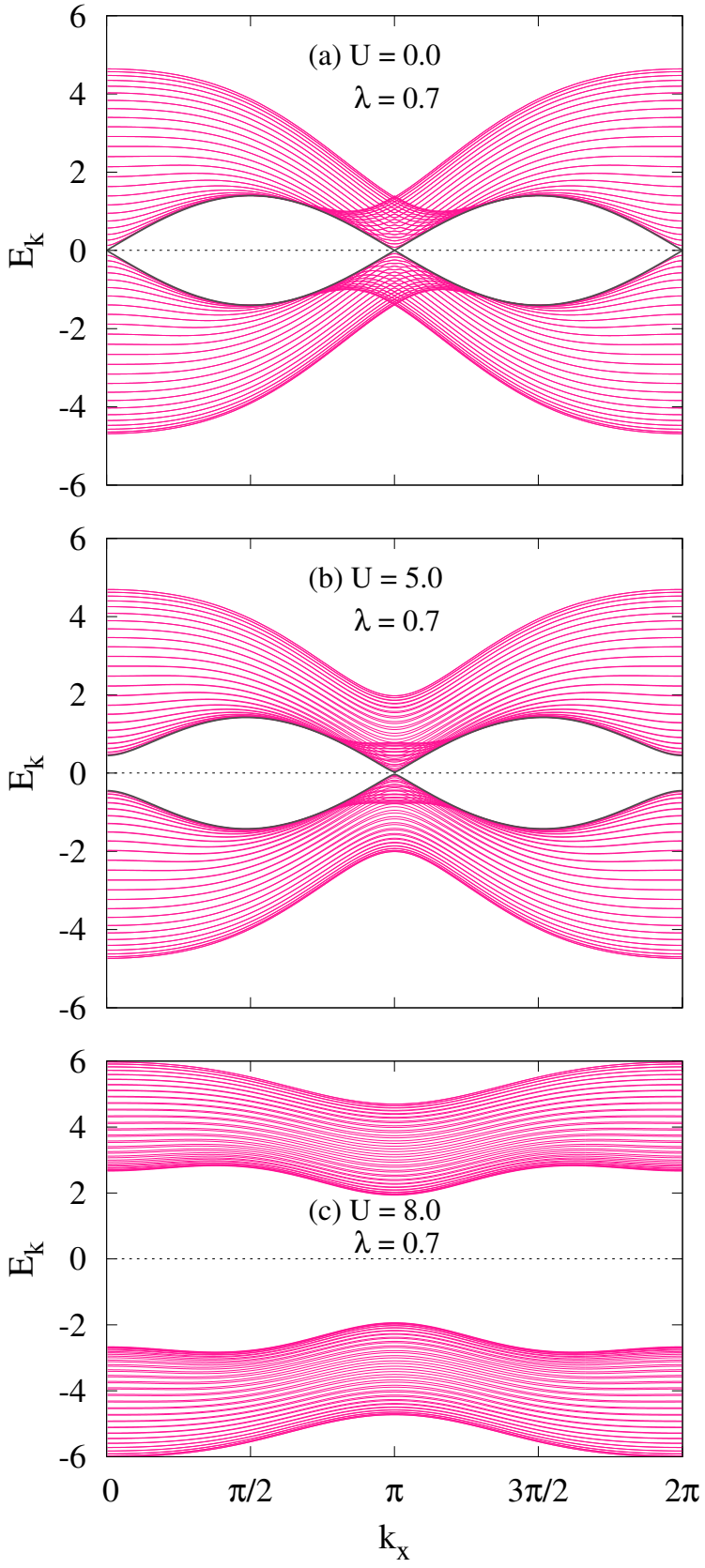

Figure 2.7: Edge-state dispersions for a ribbon of width $W = 50$ oriented along x direction compared to the bulk bands, which are projected onto a one-dimensional Brillouin zone for $\lambda = 0.7$ and (a) $U = 0.0$, (b) 5.0 and (c) 8.0.

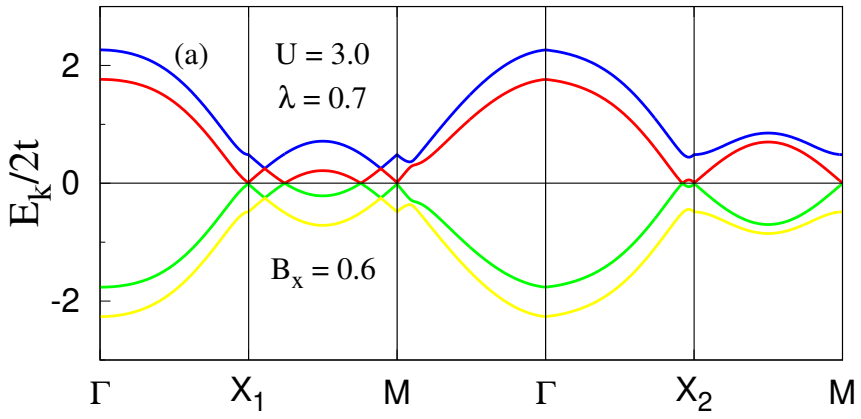

Figure 2.8: Electronic dispersion is plotted along the high symmetry directions (a) when the magnetic field-like term is applied along the x axis for the parameters $\Delta_x \approx 0.45$ and $B_x = 0.6$. The Dirac points are split into Weyl nodes along X_1-M and an additional pair of Weyl nodes emerge along Γ-X_2 as a result of perturbation.

structure. When the ribbon is extended along the x-direction, the magnetic moments are aligned parallel or antiparallel to the chain direction. In contrast, for ribbons extended along the y-direction, the magnetic moments are oriented perpendicular to the chain. This directional dependence leads to the anisotropy.

2.7 Weyl points

Next, we address the question of whether a semimetallic state can be obtained in the presence of a magnetic-field like term. In this case, the $\mathcal{PT}$ symmetry effected by $i\sigma_y\mathcal{K}\tau_1$ is preserved, where $\mathcal{K}$ is the complex conjugation operator. The consequence of a magnetic field-like term on the electronic dispersion can be obtained by incorporating the term

$$\mathcal{H}_m = B_x\sigma_x \otimes \tau_0 \tag{2.7.1}$$

into the Hamiltonian ((2.3.10)), where B_x is a parameter corresponding to the strength of the magnetic field-like term. Then, the electronic dispersion is given by

$$\begin{aligned} E_{\mathbf{k}} &= \\ &\pm \sqrt{\pm 2\sqrt{B_x^2(\varepsilon_{\mathbf{k}}^2 + \Delta_{x\mathbf{k}}'^2)} + B_x^2 + \varepsilon_{\mathbf{k}}^2 + \Delta_{x\mathbf{k}}'^2 + \Delta_{y\mathbf{k}}'^2 + \Delta_z^2}. \end{aligned} \tag{2.7.2}$$

The dispersion is plotted in Fig. 2.8 for $\Delta_x \approx 0.45$, $\lambda = 0.7$, and $B_x = 0.6$. All the three DPs in the presence of any exchange field and magnetic field-like term are split into Weyl points. One pair of Weyl points $X_{2\pm}$ are located along $k_x = 0$ at k_{y0}

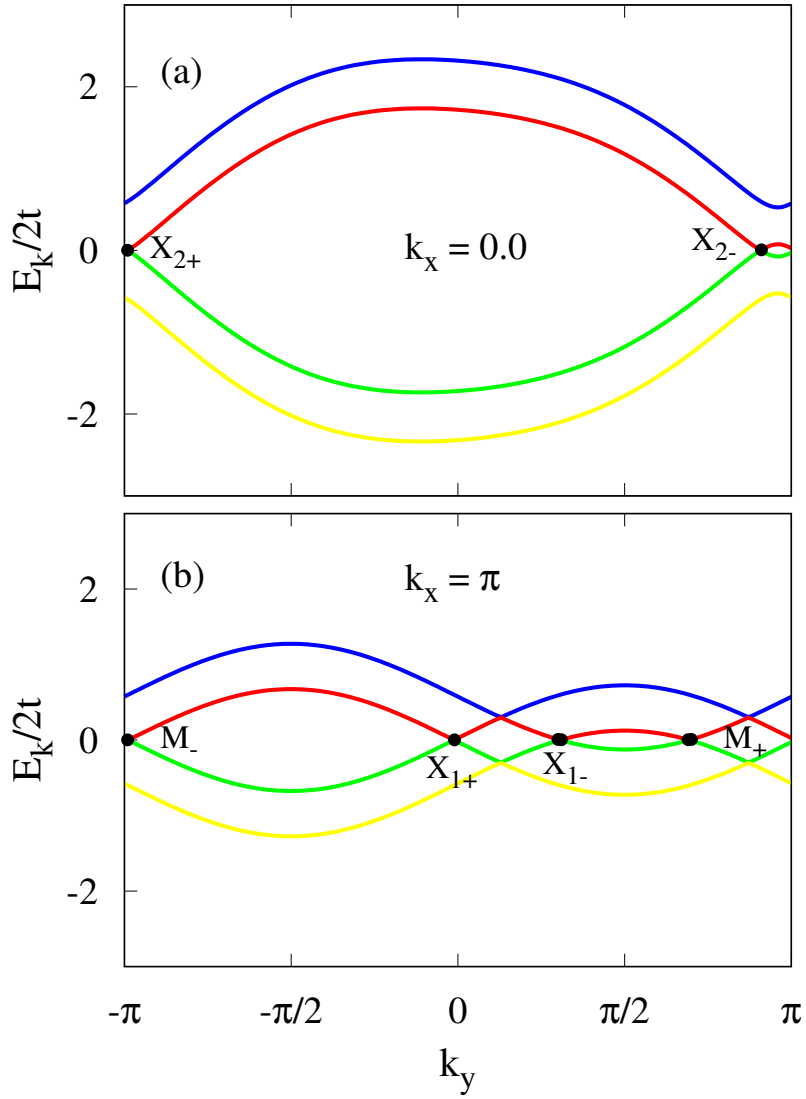

Figure 2.9: To highlight the Weyl points, the dispersion in Fig 2.8 is replotted for (a) $k_x = 0$ and (b) $k_x = \pi$ separately when k_y is varied from $-\pi$ to π. In addition to the two DPs, which are split into two Weyl points, an additional pair of Weyl points may also be noticed.

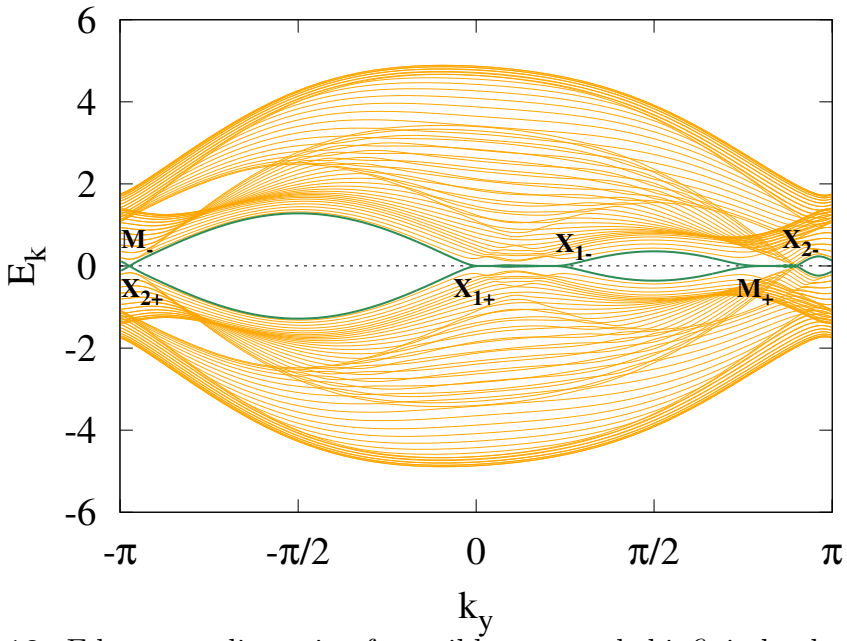

Figure 2.10: Edge-state dispersion for a ribbon extended infinitely along y direction and having a finite width $W = 50$ in the presence of magnetic field-like term. $\Delta_x \approx 0.45$ and $B_x = 0.6$

determined by the condition

$$16\cos^2 k_y/2 + (\Delta_x - 2\lambda \sin k_y)^2 = B_x^2 \tag{2.7.3}$$

provided that the solution exists. On the other hand, two pairs of Weyl points $X_{1\pm}$ and $M_\pm$ are found at k_{y0}s given by $k_{y0} = \arcsin(\pm B_x + \Delta_x)/2\lambda$ and $k_{y0} = \pi - \arcsin(\pm B_x + \Delta_x)/2\lambda$ along X_1-M for $k_x = \pi$ ((Fig. 2.9(a) and (b)). The Weyl points along $k_x = 0$ and π are accidental as they are not protected by any symmetry, particularly, the nonsymmorphic symmetry $\{C_{2y}|0\frac{1}{2}\}$ is already broken. Whether the DPs are split into Weyl points or the state turns into a normal insulator is determined by presence of magnetic field-like term or the Hubbard on-site interaction U. Moreover, the accidental degeneracy expected to occur along X_2-M in the absence of AFM order is absent [17]. Formation of Weyl points is accompanied by the edge states, which are shown in Fig. 2.10 for a ribbon of infinite length along the y axis and having a finite width $W = 50$ along x axis. The edge states are the projections of the Weyl points in the bulk which are accompanied by the flat bands connecting the Weyl nodes with opposite Chern numbers. They are distinctly seen to be present for each pair of Weyl points.

In order to compute the Chern number, the Hamiltonian in the presence of magnetic field-like term can reduced to a simple form by the following unitary transfor-

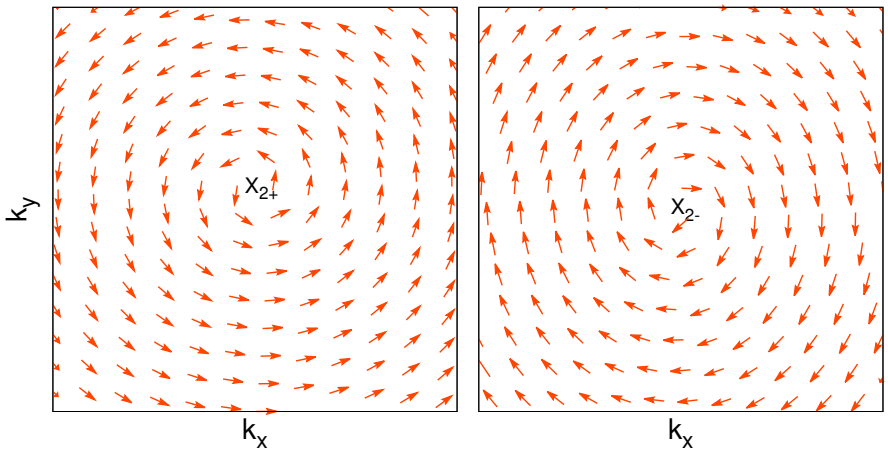

Figure 2.11: Berry connection plotted for a pair of Weyl points X_{2+} and X_{2-} obtained when an external magnetic field-like term is applied along x-direction. The Weyl points for the given pair possess winding numbers -1 and +1 depending on the clockwise and anticlockwise rotations.

mation

$$U = \frac{1}{\sqrt{2}} \begin{pmatrix} \sigma_0 & \sigma_x \\ \sigma_z & -i\sigma_y \end{pmatrix}. \tag{2.7.4}$$

After the transformation, the Hamiltonian becomes

$$\mathcal{H}' = U^{-1}\mathcal{H}U = \begin{pmatrix} H_- & B_x\sigma_0 \\ B_x\sigma_0 & H_+ \end{pmatrix}. \tag{2.7.5}$$

Here, $H_+ = H_-^\dagger = \mathbf{d}\cdot\sigma$ with $\mathbf{d} = \{\Delta'_{x\mathbf{k}}, \Delta'_{y\mathbf{k}}, \epsilon_{\mathbf{k}}\}$ and σ_is are the Pauli matrices. The above Hamiltonian $\mathcal{H}'$ reduces to the block diagonal form in the absence of any external magnetic field-like term. This form of the Hamiltonian can be used to calculate the Chern number for the various Weyl points.

The Berry connection for a pair of Weyl points X_{2+} and X_{2-} is shown in Fig 2.11. Each Weyl point has a winding number as -1 or +1 depending on the clockwise or counterclockwise rotations of the Berry connection. As expected, the total rotation of a single pair of Weyl point vanishes.

2.8 Summary

To summarize, we have examined the possible existence of Dirac semimetallic state with AFM ordering within one-orbital Hubbard model with second-neighbor spin-orbit coupling and nearest-neighbor hopping. In the non-symmorphic symmetry, when the magnetic moments are directed along the x axis in the antiferromagnetic arrange-

ment, we obtain the phase diagram in the interaction vs spin-orbit coupling parameter space. The nature of edge states is uncovered for different relative orientations of magnetic moments with respect to ribbon geometry. Our findings also suggest that the topological semimetallic state with AFM order may not be stabilized unless the magnetic moments are forced to align along the line segments joining nearest neighbor atoms in a particular sublattice. On the other hand, a Weyl semimetal is obtained when a magnetic field-like term is incorporated along a direction which is the same as that of magnetic moments.

There is no significant qualitative change in the $U - \lambda$ phase diagram when the temperature is varied. This is because, in the static meanfield theoretic approach, a phase transition from magnetic to non-magnetic order occurs through the melting of magnetic moment, i.e. the magnetic moment for a given set of parameter decreases with increase in temperature and vanishes at the critical temperature. Therefore, the effect of increase in temperature is expected to shift the phase boundaries, i.e., both the phase boundaries, separating DSM-NM and DSM-AFM, and separating DSM-AFM and AFM-I will shift downwards in the λ vs U phase diagram. Secondly, for large U, a more refined treatment for the phase diagram can be obtained with Gutzwiller approximation (GA). The main consequence of GA is to renormalize U, which leads to the reduction in the range of U for which the magnetically ordered phase will be stabilized [18]. The effect of renormalization may get enhanced when the frustration in the hopping process is incorporated.

Bibliography

[1] Hubbard J *et al* 1963 *Proc. R. Soc. A* **276** 237

[2] Imada M, Fujimori A, and Tokura Y 1998 *Rev. Mod. Phys.* **70** 1039

[3] Kane C L and Mele E J 2005 *Phys. Rev. Lett.* **95** 146802

[4] Kane C L and Mele E J 2005 *Phys. Rev. Lett.* **95** 226801

[5] Mukherjee A *et al* 2014 *Phys. Rev. B* **90** 205133

[6] Wang J 2017 *Phys. Rev. B* **95** 115138

[7] Ghosh A and Singh A 2015 *New J. Phys.* **17** 063009

[8] Tanaka Y, Shoman T, Nakayama K, Souma S, Sato T, Takahashi T, Novak M, Segawa K, and Ando Yoichi 2013 *Phys. Rev. B* **88** 235126

[9] Nakada K, Fujita M, Dresselhaus G and Dresselhaus M S 1996 *Phys. Rev. B* **54** 17954

[10] Fujita M, Wakabayashi K, Nakada K and Kusakabe K 1996 *J. Phys. Soc. Japan* **65** 1920

[11] Wakabayashi K, Fujita M, Ajiki H and Sigrist M 1999 *Phys. Rev. B* **59** 8271

[12] Wakabayashi K, Sasaki K, Nakanishi T and Enoki T 2010 *Sci Technol. Adv. Mater.* **11** 5

[13] Crépieux A, Pangburn E, Haurie L, Awoga O A, Black-Schaffer A M, Sedlmayr N, Pépin C, and Bena C 2023 *Phys. Rev. B* **108** 134515

[14] Fertig H A and Brey L 2006 *Phys. Rev. Lett.* **97** 116805

[15] Lau A and Timm C 2013 *Phys. Rev. B* **88** 165402

[16] Lado J L, García-Martínez N and Fernández-Rossier J 2015 *Synth Met.* **210** 56

[17] Matveeva P G, Aristov D N, Meidan D and Gutman D B 2019 *Phys. Rev. B* **99** 075409

[18] Markiewicz R S, Lorenzana J and Seibold G 2010 *Phys. Rev. B* **81** 014510

Chapter 3

Collective excitations in a TSM state with AFM order in a non-symmorphic crystal

In this chapter, we investigate the collective excitation spectrum—specifically, the optical conductivity and quasiparticle interference—in a topological semimetallic phase exhibiting antiferromagnetic (AFM) order in a two-dimensional crystal possessing nonsymmorphic symmetry.

3.1 A Comprehensive Overview

Collective excitations constitute a cornerstone of condensed matter physics, as they encapsulate the emergent electronic, magnetic, and optical properties arising from many-body interactions. These excitations originate from the correlated dynamics of multiple degrees of freedom and cannot be adequately described within a single-particle framework. In contrast to elementary excitations involving individual electrons, phonons, or spins, collective modes emerge from the cooperative behavior of charge, spin, lattice, and orbital degrees of freedom. As a result, they play a decisive role in governing a wide range of physical phenomena, including unconventional superconductivity, magnetic ordering, charge transport, optical responses, and the realization of topological phases of matter [1]. Such excitations are ubiquitous across diverse classes of materials, ranging from conventional metals and semiconductors to strongly correlated electron systems and topological materials.

In systems with nontrivial band topology, collective excitations often acquire distinctive characteristics due to the interplay between topology and fundamental interactions such as electron–electron correlations, electron–phonon coupling, and spin–orbit interaction [2, 3]. For example, the protected boundary modes in topological insulators and topological semimetals can be viewed as collective manifestations of the underlying bulk topology. Similarly, topological superconductors host zero-energy Majorana modes at their surfaces or interfaces, which represent emergent collective excitations with non-Abelian statistics and are of considerable interest for fault-tolerant quantum computation [4,5]. In topological semimetals, including Dirac,

Weyl, and nodal-line semimetals, collective excitations arise from low-energy quasiparticles associated with symmetry-protected band crossings and strongly influence transport, magnetic, and optical properties [6].

The importance of collective excitations is further amplified in materials exhibiting magnetic order and additional broken symmetries, such as time-reversal symmetry. In magnetically ordered systems, spin-dependent collective modes—most notably magnons and spin-wave excitations—emerge as a consequence of long-range magnetic order [7]. In iron-based pnictides, the parent compounds typically exhibit a spin-density-wave (SDW) ground state, where the reconstructed electronic structure hosts low-energy collective excitations that strongly couple to itinerant electrons [8]. Experimental and theoretical studies have revealed the presence of Dirac-like quasiparticles in the SDW phase of iron pnictides, highlighting a nontrivial interplay between magnetism, band topology, and collective modes [9, 10]. These excitations significantly modify the low-energy electronic spectrum and leave clear signatures in optical, magnetic, and transport responses.

Among the experimental probes available to investigate collective excitations, *optical conductivity* and *quasiparticle interference* (QPI) have emerged as particularly powerful and complementary techniques, especially in strongly correlated systems such as iron-based superconductors, high-T_c cuprates, and heavy-fermion materials [11]. In the following, we briefly discuss their relevance for probing low-energy dynamics.

1. **Optical Conductivity**: Optical conductivity characterizes the linear response of a material to an external electromagnetic field over a broad frequency range and is formally derived from the current–current correlation function. It provides direct access to charge dynamics and collective modes [12].

    - At low frequencies (infrared to terahertz), optical conductivity captures intraband transitions, Drude response (free carrier motion), and collective modes (e.g., plasmons).
    - It reflects low-energy gap openings such as superconducting gap, pseudogap, electronic states in the vicinity of the Fermi level, inelastic scattering processes and many-body renormalizations.

    In iron pnictides, optical conductivity measurements have played a crucial role in identifying SDW-induced gap openings, Dirac-like linear dispersions, and the evolution of electronic correlations across magnetic and superconducting phase transitions [13, 14].

2. **Quasiparticle Interference**: Quasiparticle interference arises in scanning tunneling microscopy and spectroscopy (STM/STS) experiments as a result of the elastic scattering of quasiparticles from impurities or defects, leading to spatial modulations in the local density of states (LDOS). Fourier transformation of these real-space modulations yields momentum-resolved information about quasiparticle scattering processes [15].

   - QPI maps out the dispersion of quasiparticles near the Fermi surface.
   - Used to study superconducting gap symmetry, bandstructure near the Fermi level, electron-phonon coupling effects at low energies, etc.

   Owing to the sub-meV energy resolution achievable in STM/STS experiments, QPI provides a highly sensitive probe of low-energy quasiparticle and collective excitations, making it particularly suitable for investigating Dirac fermions and SDW-related band reconstruction in iron-based superconductors [16].

In the following analysis, we examine the optical conductivity and quasiparticle interference (QPI) patterns of a two-dimensional (2D) Dirac semimetal exhibiting antiferromagnetic (AFM) order. This magnetic phase was previously explored in the context of a 2D AFM-ordered crystal possessing non-symmorphic symmetry. To this end, we consider a square lattice with a single orbital per site. The unit cell consists of two distinct atomic species, forming a bipartite (two-sublattice) structure with lattice vectors defined as $\vec{a} = (1, 0, 0)$ and $\vec{b} = (0, 1, 0)$.

To introduce non-symmorphic symmetry, atoms labeled A and B within the unit cell are displaced slightly along the perpendicular $\pm z$ directions by equal fractions of the lattice constant. This structural configuration facilitates the presence of next-nearest-neighbor spin–orbit coupling (SOC). Additionally, when the magnetic moments are oriented along the line connecting atoms of the same sublattice, the resulting Dirac points are preserved by the combined action of time-reversal and inversion symmetries, despite the fact that each symmetry is individually broken. The corresponding real-space Hamiltonian was presented earlier in Eq. (2.2.2). The mean-field decoupled Hamiltonian, along with its Fourier-transformed counterpart in momentum space, is provided in the set of equations eqs. (2.3.7) to (2.3.11).

Different states may emerge in the U-*vs*-λ parameter space when the magnetic moments are aligned along the x-direction, including antiferromagnetically ordered Dirac semimetal (AFM-DSM) protected by glide mirror symmetry $\{M_{\hat{x}}|\frac{1}{2}0\}$, DSM with nonmagnetic order (DSM-NM), and AFM insulating (AFM-I) states. In the following, we use $\Delta_x = 0.62, 0$, and 1.9 in the unit of t, respectively, for the AFM-DSM, DSM-NM, and AFM-I states. On the other hand, when another symmetry

breaking term equivalent to a magnetic field along the x-direction is incorporated, Dirac points split into pairs of Weyl nodes, forming a Weyl semimetallic state. The chosen set of parameters is $\Delta \approx 0.45$, $\lambda = 0.7$, and $B_x = 0.6$. In that case, the Hamiltonian is modified by incorporating the term given by Eq. 2.7.1 in Eq. 2.3.10.

3.2 Optical conductivity

The low-energy part of different types of excitations for a TSM is expected to be strongly influenced by the presence of topologically protected band crossings at the Fermi level. To explore the impact, we investigate charge dynamics by studying the optical conductivity in the two orthogonal directions, σ_ν ($\nu = x, y$), using Kubo's formula [12, 17], which is defined as the real part of the current-current correlation function, expressed as

$$\sigma_{\mu\nu}(\omega) = \frac{1}{\omega}\mathrm{Im}\Pi^R_{\mu\nu}(\omega + i0^+) \tag{3.2.1}$$

where $\Pi^R_{\mu\nu}(\omega)$ is the retarded current-current correlation function. $\mu, \nu \in \{x, y, z\}$ denote the Cartesian coordinates. The current-current correlator in the Matsubara frequency space can be computed as

$$\Pi^R_{\mu\nu}(i\omega_n) = \int_0^\beta d\tau e^{i\omega_n\tau}\langle T_\tau[\hat{J}_\mu(\tau), \hat{J}_\nu(0)]\rangle \tag{3.2.2}$$

Here $\beta = \frac{1}{kT}$ is the inverse temperature. $\omega_n = 2\pi n/\beta$ are bosonic Matsubara frequencies and $\hat{J}_\mu(t)$ denotes the current operator. $i\omega_n = \omega + i0^+$ is used for analytic continuation.

For a system described by a Hamiltonian $\mathcal{H}_\mathbf{k}$ with AFM ordering (given by Eq. (2.3.10)), the real part of the optical conductivity in a direction ν at zero temperature can be written in terms of single particle bands as [17, 18]

$$\begin{aligned}\sigma_\nu(\omega) &= D_\nu\delta(\omega) + \frac{\pi}{N}\sum_{\mathbf{k},n\neq n'}\frac{|j^\nu_{nn'}(\mathbf{k})|^2}{\varepsilon_{n'\mathbf{k}} - \varepsilon_{n\mathbf{k}}} \\ &\times \theta(\varepsilon_{n'\mathbf{k}})\theta(-\varepsilon_{n\mathbf{k}})\delta(\omega - \varepsilon_{n'\mathbf{k}} + \varepsilon_{n\mathbf{k}}),\end{aligned} \tag{3.2.3}$$

where D_ν denotes the Drude weight given by

$$\begin{aligned}\frac{D_\nu}{2\pi} &= \frac{\pi}{2N}\sum_\mathbf{k} T^\nu_{nn}(\mathbf{k})\theta(-\varepsilon_{n\mathbf{k}}) - \frac{\pi}{N}\sum_{\mathbf{k},n\neq n'}\frac{|j^\nu_{nn'}(\mathbf{k})|^2}{\varepsilon_{n'\mathbf{k}} - \varepsilon_{n\mathbf{k}}} \\ &\times \theta(\varepsilon_{n'\mathbf{k}})\theta(-\varepsilon_{n\mathbf{k}}).\end{aligned} \tag{3.2.4}$$

$\varepsilon_{n\mathbf{k}}$ represents the single-particle energy, θ is the step function, and n (or n') denotes

the band index. Furthermore, the kinetic energy (T^{μ}_{nn}) and the current ($j^{\mu}_{nn'}$) operators along different directions can be written as the double and single derivatives of the Hamiltonian matrix, defined as:

$$T^{\nu}_{nn} = \sum_{\sigma\sigma'} T^{\nu:\sigma\sigma'}_{nn} = \sum_{\mathbf{k},\sigma,\sigma'} \frac{\partial^2 \mathcal{H}_{\sigma\sigma'}(\mathbf{k})}{\partial k_\nu^2} c^*_{\mathbf{k}n\sigma} c_{\mathbf{k}n\sigma'},$$
$$j^{\nu}_{nn'} = \sum_{\sigma\sigma'} j^{\nu:\sigma\sigma'}_{nn'} = -\sum_{\mathbf{k},\sigma,\sigma'} \frac{\partial \mathcal{H}_{\sigma\sigma'}(\mathbf{k})}{\partial k_\nu} c^*_{\mathbf{k}n\sigma} c_{\mathbf{k}n'\sigma'}. \tag{3.2.5}$$

$c_{\mathbf{k}n\sigma}$ represents the matrix element belonging to the unitary transformation that maps the spin and sublattice basis onto the band basis. The Hamiltonian, defined by Eq. (2.3.10)) can be rewritten as $\hat{\mathcal{H}}_{\sigma\sigma'}(\mathbf{k}) = \varepsilon_{\mathbf{k}}\sigma_0\tau_0 + (\mathbf{g}_{\mathbf{k}} \cdot \boldsymbol{\sigma}) \otimes \tau_z + \Delta_x\sigma_x \otimes \tau_z$. Here, $\varepsilon_{\mathbf{k}} = 4t\cos(k_x/2)\cos(k_y/2)$ and $\mathbf{g}_{\mathbf{k}} \cdot \boldsymbol{\sigma} = (-2\lambda \sin k_y, 2\lambda \sin k_x, 0)$ belonging to the AFM ordered system. It may be noted that the Hamiltonian $\hat{\mathcal{H}}(\mathbf{k})$ breaks both time-reversal symmetry ($\boldsymbol{\mathcal{T}}$) and inversion symmetry ($\boldsymbol{\mathcal{P}}$). In the numerical evaluation, the δ-function is approximated by a Lorentzian with a small broadening parameter, which is chosen to be the same along both directions.

Fig. 3.1 shows the electronic band dispersion, density of states (DOS), and optical conductivity in the Dirac-semimetallic state of the unordered state of a non-symmorphic crystal. The Dirac points occur at the high-symmetry points X (π, 0), Y (0, π), M (π, π). The DOS has four peaks in the whole energy range, which are placed symmetrically across the Fermi level ($\omega = 0$). The nearest and farthest peaks are located at $|\omega| \sim 2$ and ~ 4, respectively. This aspect is also reflected in the optical conductivity ($\sigma(\omega)$), which exhibits peaks near $\omega \sim 4$ and 8. These peaks arise because of the interband transition between the states associated with the band extrema located near a point such as Γ and a point in the middle of X and M. Moreover, as expected, the almost constant low-energy characteristics of the optical conductivity follow those of a typical topological semimetal. No anisotropy exists without magnetic order as $\sigma_x(\omega) = \sigma_y(\omega)$.

Next, we consider the case of the AFM-DSM state with magnetic moments aligned along the x direction. In this state, the Dirac fermions at Y become massive, and the dispersion becomes gapped. On the other hand, the Dirac points originally at X and M move towards each other along X-M. This is displayed in Fig. 3.2, which shows electronic band dispersion along X $(\pi, 0) \rightarrow$ M (π, π) in the AFM-DSM state that hosts two distinct Dirac points, labeled D_1 and D_2. Each of these points exhibits a two-dimensional Dirac character, with linear dispersion in the vicinity of the crossing along two mutually perpendicular momentum directions. This linear behavior is explicitly

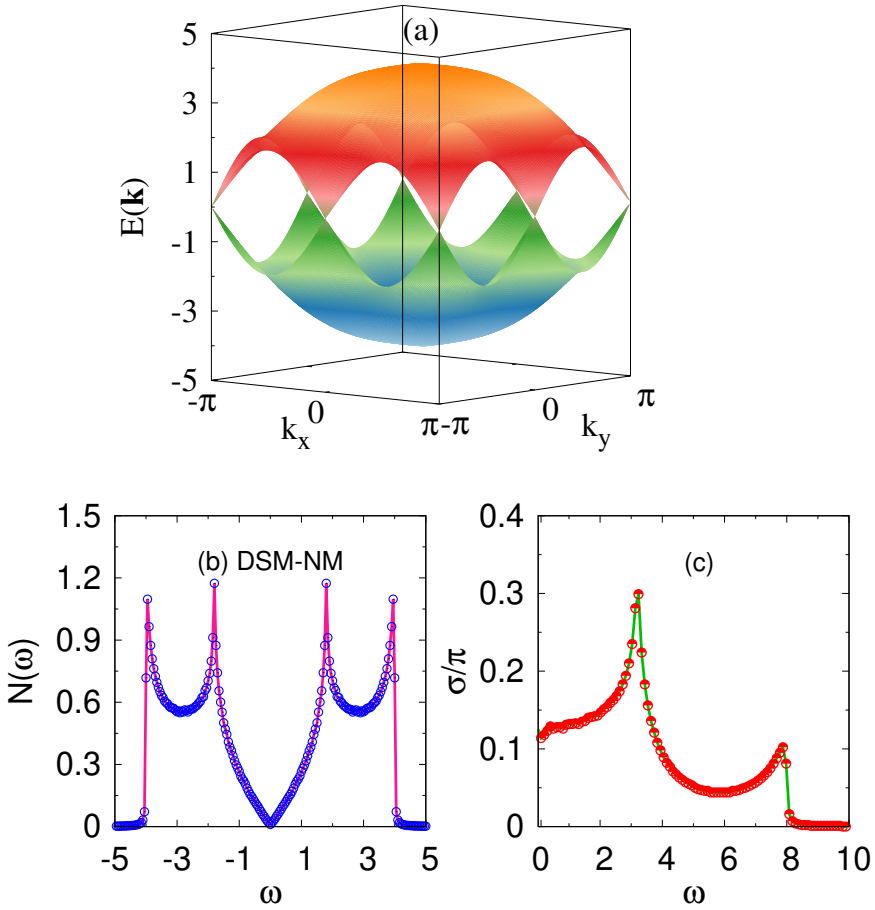

Figure 3.1: (a) Band dispersion in the DSM-NM state. DPs are obtained at high-symmetry points such as $(0, \pi)$, $(\pi, 0)$, (π, π). (b) DOS ($N(\omega)$) and (c) optical conductivity as a function of ω in the unordered state. x and y-components of conductivity have the same magnitudes.

illustrated in the inset panels, where (a) and (b) correspond to the momentum cuts through D_1, and (c) and (d) correspond to those through D_2. Such linear dispersion in both principal directions is a defining feature of Dirac quasiparticles, in clear contrast to semi-Dirac systems, which display linear dispersion along one momentum direction but quadratic dispersion along the other.

An important consequence of the AFM order is the suppression of the peak in DOS at $|\omega| \sim 4$ (Fig. 3.3(a)) because of the reduction in flatness of the dispersion around Γ. The peak near $|\omega| \sim 2$ is split into two because of the asymmetry induced by the AFM order along Γ-X and Γ-Y. An additional very small cusp near $\omega \sim 0.8$ arises due to the interband transition between the extrema of bands along X-M (not shown).

One remarkable feature of the optical conductivity in the AFM-DSM state is that it is highly anisotropic, i.e., $\sigma_x(\omega) \neq \sigma_y(\omega)$. $\sigma_y < \sigma_x$ for smaller as well as larger ω,

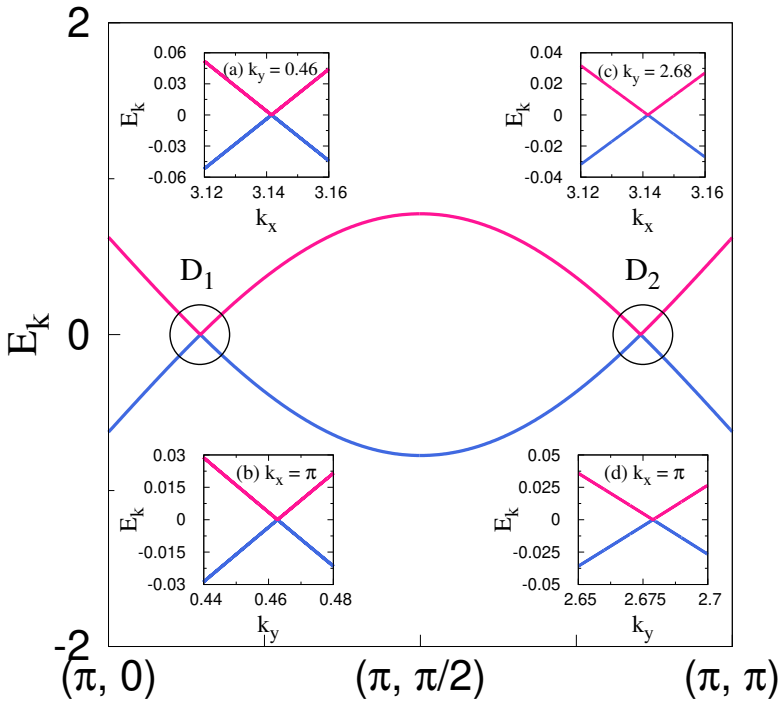

Figure 3.2: Two Dirac points along the high-symmetry path $(\pi, 0) \rightarrow (\pi, \pi)$ are labeled as D_1 and D_2. The inset panels show the dispersions near each Dirac point along the x- and y-momentum directions: panels (a) and (b) correspond to D_1. In contrast, panels (c) and (d) correspond to D_2.

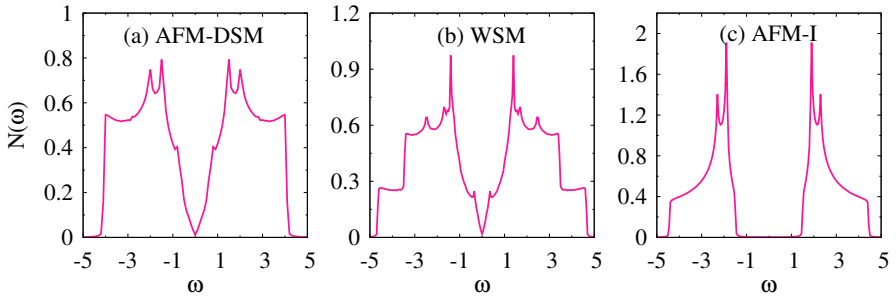

Figure 3.3: DOS as a function of ω in the (a) AFM-DSM, (b) WSM, and (c) AFM-I states.

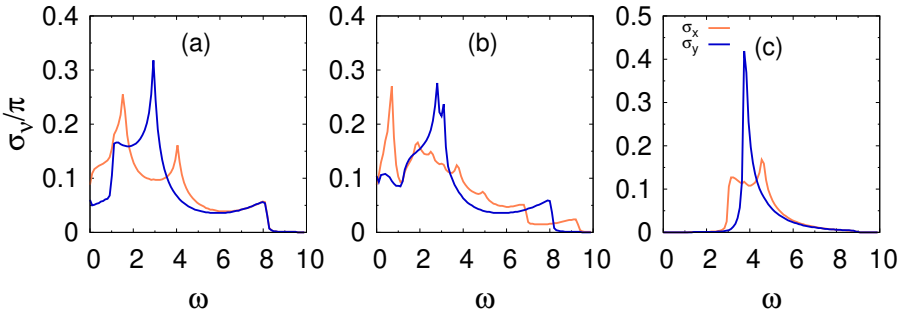

Figure 3.4: Direction dependent optical conductivity varying with energy ω in the (a) AFM-DSM, (b) WSM, and (c) AFM-I states.

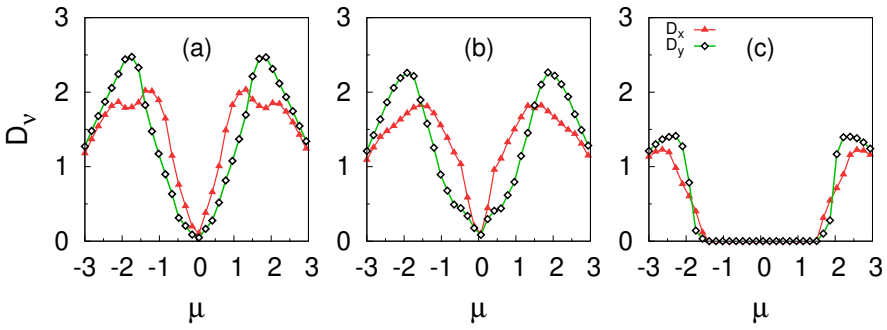

Figure 3.5: The figure demonstrates Drude weights along x and y-directions as a function of chemical potential in the (a) AFM-DSM, (b) WSM, and (c) AFM-I states.

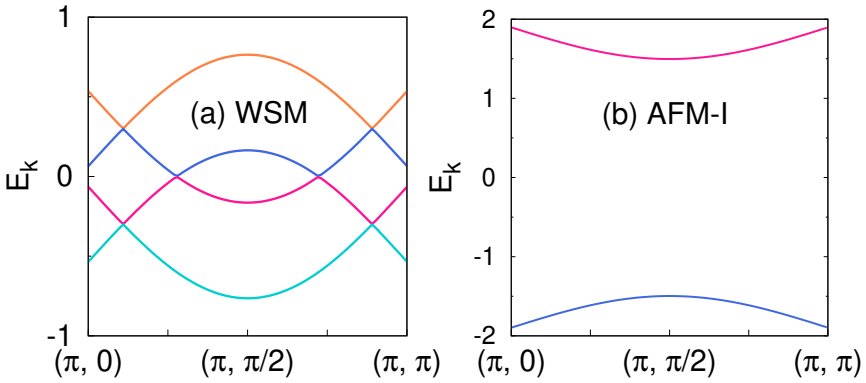

Figure 3.6: Electronic band dispersion along $(\pi, 0) \rightarrow (\pi, \pi)$ in the (a) WSM state and (b) AFM-I state.

whereas the nature of anisotropy reverses in the intermediate range of ω (Fig. 3.4(a)). Here, it is worthwhile to note that there is no anisotropy in the absence of spin-orbit coupling despite the fact that magnetic moments are aligned along the x direction. This is not surprising, as in that case, four-fold rotation symmetry associated with the nearest-neighbor hopping has been considered, and $SU(2)$ symmetry is also present. Thus, the orientation of magnetic moments in the AFM-ordered state does not introduce anisotropy when there is $SU(2)$ rotation symmetry in the absence of SOC. Thus, the interplay between SOC and the direction of magnetic moments is responsible for anisotropy in the optical conductivity. Even in the DSM state with antiferromagnetic order, low-energy characteristics of optical conductivity, typical of DSM state without magnetic order, persists.

Fig. 3.5(a) shows the Drude weight as a function of the chemical potential along x and y directions. On the expected line, it is also anisotropic. However, the degree of anisotropy is not as pronounced as in the low-frequency region of optical conductivity. The overall behavior of the anisotropy of the Drude weights quantified by the ratio D_x/D_y as a function of μ, it is not far away from $\sim$ 1.0 in a major region with

$|\mu| \gtrsim 1$, in contrast with the anisotropy in optical conductivity for smaller frequency ($\sigma_x/\sigma_y \sim 2$). It is only when μ is small, $D_x/D_y \to 2$.

It may be noted that, in the Dirac semimetallic state, the density of states at the Fermi level becomes vanishingly small. Consequently, the Drude weights in both directions are suppressed; however, the ratio $D_x/D_y \sim 1.7$ while $\sigma_x/\sigma_y \sim 2$. Thus, as ω moves away from 0, the anisotropy contributions from ω-dependent parts become increasingly important. Furthermore, the nature of anisotropy gets reversed at $|\mu| \approx 1.5$.

In the presence of a term like $\sigma_x \otimes \sigma_0$ given by Eq. (2.7.1), the band degeneracy is lifted and each Dirac point splits into a pair of Weyl points. One such pair emerging along the $(\pi, 0) \to (\pi, \pi)$ direction is illustrated in Fig. 3.6(a). The dispersion in the vicinity of these Weyl points is linear. A second pair of Weyl nodes appears along the $\Gamma(0,0) \to Y(0,\pi)$ direction. As a consequence, the number of cusps in the DOS is nearly doubled (Fig. 3.3(b)), which is also reflected in the form of multiple peaks in the optical conductivity (Fig. 3.4(b)). The locations of split peaks are slightly shifted, and the anisotropy continues to exist with nearly the same degree and nature. The low-energy peaks obscure low-energy behavior of the optical conductivity, and therefore, the constant behavior is not so evident. The Drude-weight anisotropy is negligible for $\mu \sim 0$ (Fig. 3.5(b)). When $|\mu|$ is increased, the anisotropy first rises and then diminishes afterward; the behavior is more or less similar to that in the AFM-DSM state.

Figs. 3.3(c) and 3.6(b) show DOS and band dispersion in the AFM-I state in the absence of any magnetic field. The existence of conductivity anisotropy, even in this state, indicates that it is not exclusively a characteristic of the TSM state (Fig. 3.4(c)). Like the topological semimetallic states, it arises because of the interplay between SOC and the orientation of magnetic moments. The conductivity anisotropy is large in the vicinity of $\omega \sim 4.0$. The Drude weight anisotropy is weak. It is non-vanishing only for significant chemical potential and is seen to be weakly anisotropic Fig. 3.5(c)).

3.3 Quasiparticle Interference due to a single impurity

Quasiparticle interference is another powerful tool that can reveal the nature of electronic states in the vicinity of Fermi surfaces. In particular, it can provide important insight into the orientation of electronic spin as one moves along the constant-energy surfaces in the vicinity of symmetry-protected band crossing of topologically non-

trivial nature. In the vicinity of Dirac/Weyl points, the back-scattering process in the quasiparticle interference is not allowed. However, the scenario is considerably simplified when such topological systems are accompanied by magnetic order and can be responsible for interesting QPI patterns.

Theoretically, QPI can be studied by analyzing the modulation in the density of states (DOS) induced by a single impurity, which requires the use of Green's function formalism. The change in the Green's function due to the impurity atom with a δ-potential can be obtained by using the T-matrix approximation [19, 20], which is given by

$$\delta\hat{G}(\mathbf{k}_1, \mathbf{k}_2, \omega) = \hat{G}^0(\mathbf{k}_1, \omega)\hat{T}(\omega)\hat{G}^0(\mathbf{k}_2, \omega), \tag{3.3.1}$$

where $\hat{G}^0(\mathbf{k}, \omega) = (\hat{I}(\omega + i\eta) - \hat{\mathcal{H}}_{\sigma\sigma'}(\mathbf{k}))^{-1}$ is the free particle Green's function. The scattering matrix $\hat{T}$ is obtained from the Lippmann-Schwinger equation and is expressed in terms of the Green's function and impurity potential as:

$$\hat{T}(\omega) = (\hat{I} - \hat{V}^m\hat{\mathcal{G}}^0(\omega))^{-1}\hat{V}^m, \tag{3.3.2}$$

where the Green's function summed over all momenta in the Brillouin zone is defined as:

$$\hat{\mathcal{G}}^0(\omega) = \frac{1}{N}\sum_{\mathbf{k}} \hat{G}^0(\mathbf{k}, \omega). \tag{3.3.3}$$

We consider scattering in both the magnetic and nonmagnetic channels. Furthermore, we consider the scenario in which the single impurity is placed on any of the two sublattices, possibly leading to different QPI patterns. Thus, impurity scattering matrix V_i^m is defined as

$$\hat{V}_i^m = \hat{V}_1 \otimes \hat{\sigma}_i,$$

where the form of $\hat{V}_1$ depends on whether the impurity is placed on sublattice A or B, defined as

$$\hat{V}_1 = V_o \begin{pmatrix} 1 & 0 \\ 0 & 0 \end{pmatrix} \qquad \text{(sublattice A)} \tag{3.3.4}$$

and

$$\hat{V}_1 = V_o \begin{pmatrix} 0 & 0 \\ 0 & 1 \end{pmatrix} \qquad \text{(sublattice B)}, \tag{3.3.5}$$

Thus, the matrix V_i^m becomes a 4×4 scattering matrix, expressed in terms of Pauli matrices $\sigma_i (i = 1, 2, 3)$ or σ_0 is a 2×2 identity matrix. The former corresponds to a magnetic impurity and latter to the nonmagnetic one. In case, one considers only σ_i, it means that the magnetic impurity has spin pointing along x direction. We set the scattering potential parameter $V_o = 0.1$ for subsequent analysis. Finally, the change

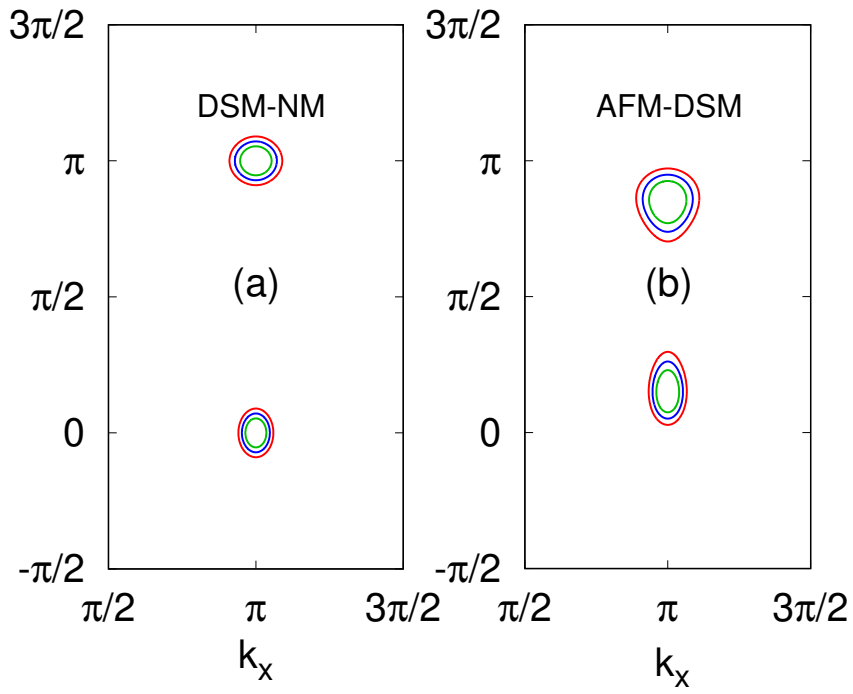

Figure 3.7: The constant-energy contours at different energies for (a) DSM-NM and (b) AFM-DSM states. The innermost contour corresponds to the energy $\omega = 0.3$ while the outermost to $\omega = 0.5$.

in DOS, $\delta\rho(\mathbf{q}, \omega)$, caused by impurity scattering is given by

$$\delta\rho(\mathbf{q}, \omega) = -\frac{1}{\pi}\mathrm{Im}\sum_{\mathbf{k}} \mathrm{Tr}\left[\hat{G}^0(\mathbf{k}, \omega)\hat{T}(\omega)\hat{G}^0(\mathbf{k}+\mathbf{q}, \omega)\right] \tag{3.3.6}$$

The above expression represents the Fourier-transformed modulation of the local density of states arising from elastic scattering processes between quasiparticle states with momenta $\mathbf{k}$ and $\mathbf{k}+\mathbf{q}$. The quantity $\delta\rho(\mathbf{q}, \omega)$ thus encodes the interference pattern generated by multiple scattering channels allowed in the system. The imaginary part in Eq. (3.3.6) corresponds to the dissipative (spectral) component of the LDOS modulation and is directly related to the experimentally measurable differential conductance in Fourier-transform scanning tunneling spectroscopy (FT-STS) experiments.

Peaks in $\delta\rho(\mathbf{q}, \omega)$ signify dominant scattering vectors $\mathbf{q}$ connecting regions of high spectral weight on the constant-energy contours of the band structure. These vectors correspond to elastic scattering processes between equal-energy quasiparticle states and thus provide a direct mapping of the underlying Fermi surface topology and the anisotropy of low-energy excitations.

Figure 3.7 shows the constant-energy contours in the vicinity of Dirac points at different energies in the (a) DSM-NM and (b) AFM-DSM states. A notable distinction

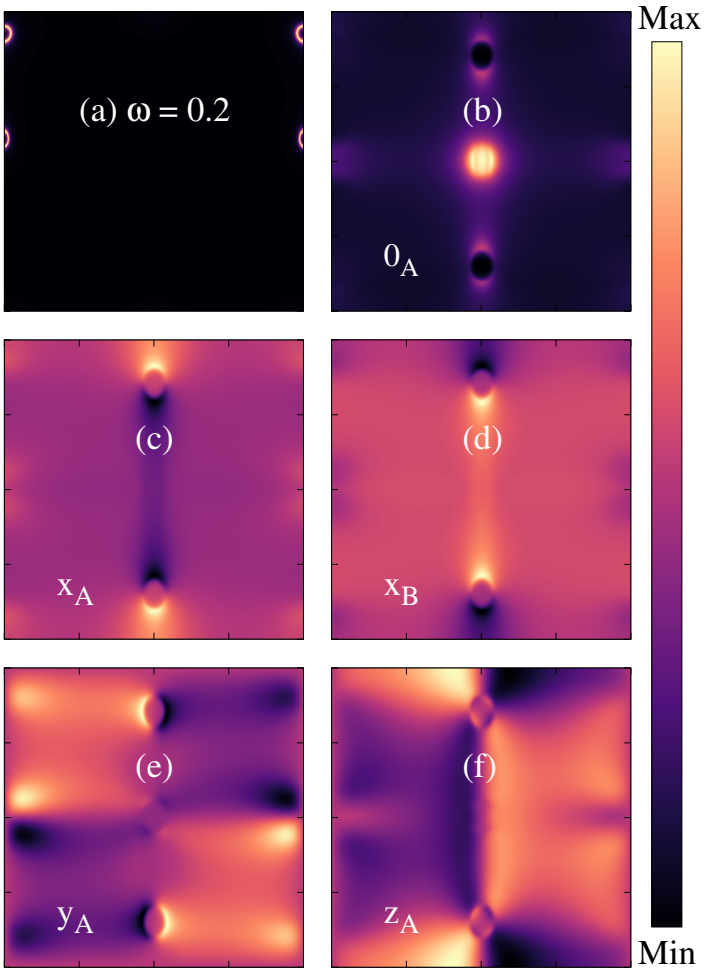

Figure 3.8: (a) The spectral function $\mathcal{A}(\mathbf{k}, \omega)$ and (b) the corresponding QPI pattern for a nonmagnetic impurity placed inside a sublattice A. The second row displays the QPI patterns for a spin-polarized impurity oriented along the x-direction, with the impurity situated on (c) sublattice A and (d) on sublattice B. The third row shows the QPI patterns for spin polarization along the (e) y-axis and (f) z-axis, respectively. All calculations are carried out at a fixed energy of $\omega = 0.2$ in the AFM-DSM state.

exists in the ellipticity of pockets in these two cases. In the DSM-NM phase, the pockets around $(\pi, 0)$ expand uniformly while maintaining nearly constant ellipticity, which results from unequal coefficients of q_x and q_y, and it can easily be noticed from the effective Hamiltonian. The contours are nearly circular around (π, π) as these coefficients are equal. On the other hand, in the AFM-DSM phase, the constant-energy contours show more deviation from the circular shape and a simultaneous increase in both the size and ellipticity of the pockets with energy. These variations in pockets' morphology can be instrumental in understanding the features of QPI patterns.

Understanding the QPI patterns purely from the distribution of A or B sublattice contributions along CECs or from the electronic spin contributions is tedious. The complication results from using real and momentum-space basis together to construct the Hamiltonian and its eigenvectors to examine the nature of the quasiparticle states along the contours. There is no continuous distribution of sublattices along the CECs. For the same reason, we find no continuous distribution of spin orientation along the CECs.

Fig. 3.8(a) shows the constant energy surface for $\omega = 0.2$ in the AFM-DSM state. There are two pairs of pockets, one pair along $\mathrm{X}_1(\pi, 0) \rightarrow \mathrm{M}_1(\pi, \pi)$, and the other pair along $\mathrm{X}_2(-\pi, 0) \rightarrow \mathrm{M}_2(-\pi, \pi)$. It may be noted that the electronic spin can be oriented either along positive or negative x axis only.

First, we examine the role of a nonmagnetic impurity placed inside a sublattice A, on the QPI patterns (Fig. 3.8(b)). A nonmagnetic impurity does not change the spin state of an electron getting scattered; i.e., an electron with a particular spin state will scatter to a spin state with the same orientation. This is possible for both the intra- and inter-pocket scattering processes. The pattern appearing near Γ results from the intrapocket scattering, while the other two result from the interpocket scattering.

Next, we consider QPI patterns generated by an impurity placed inside a sublattice: A or B. Note that the patterns resulting in the two cases are not identical. Figs. 3.8(c) and (d) show the QPI patterns generated by the magnetic impurity when it is aligned along the x-axis. It may be noted that when σ_x operates on a spinor, the result is a spinor with switched components. Thus, if the magnetic impurity is aligned along the x direction, then the strongest scattering will be allowed only when a state to which the quasiparticle scatters exists with a spinor having maximum possible inner product with the spinor of quasiparticles with switched components. The patterns generated because of the magnetic impurity are similar when the impurity was nonmagnetic. However, there are several important differences with respect to the case of nonmagnetic impurities. There is no pattern near Γ, and for the patterns

along Γ-Y_1 and Γ-Y_2, upper and lower parts have modulations of opposite sign. The patterns are modified in such a way that the sign of density modulation is reversed when the same impurity is placed in the sublattice B.

Fig. 3.8(e) shows the QPI patterns when the magnetic impurity is oriented along the y direction. When σ_y operates on a spinor state, it not only switches components but also introduces an important phase difference. The result is a much more complex pattern, which consists of a pocket-like structure near Γ and along Γ-Y_1 and Γ-Y_2. Again, the sign of density modulation reverses if the impurity atom is placed inside the sublattice B. Similarly when the impurity is oriented along the z direction, similar complexity continues to exist (Fig. 3.8(f)), however, in this case, there does not exist any difference which is dependent on whether the impurity atom is placed in the sublattice A or B.

3.4 Summary

The work carried out here provides important insight into the low-energy charge dynamics and quasiparticle scattering phenomena in a two-dimensional topological semimetal with a checkerboard-type antiferromagnetic (AFM) order realized in a non-symmorphic crystal. By employing a Hubbard Hamiltonian incorporating nearest-neighbor hopping, next-nearest-neighbor spin–orbit coupling (SOC), and on-site Coulomb interactions, we have demonstrated how the interplay between the magnetic moment ordering and SOC gives rise to pronounced anisotropy in both the optical conductivity and quasiparticle interference (QPI) responses.

The optical conductivity analysis reveals a distinct anisotropy between $\sigma_x(\omega)$ and $\sigma_y(\omega)$, which is absent in the nonmagnetic DSM phase. It is noted that the SOC alone does not generate anisotropy if magnetic moments vanish. Similarly, the anisotropy is absent when AFM order exists in the absence of SOC. This indicates that anisotropy originates solely from the interplay between SOC and the orientation of AFM moments, rather than from magnetic ordering alone. The emergence of optical anisotropy thus directly offers a clear experimental signature of the coupling between spin–orbit interaction and magnetic order in two-dimensional topological semimetals.

When the band degeneracy is lifted as a result of the application of magnetic field along the magnetization direction, Dirac nodes split into pairs of Weyl points, driving a DSM-WSM crossover. This transition is manifested in multiple additional peaks in the optical conductivity and a doubling of density-of-states features, representing the optical fingerprints of Weyl physics in two dimensions. Importantly, the optical anisotropy persists across this transition, indicating that the fundamental

symmetry-breaking mechanism remains operative even after the topological nature of the quasiparticles changes.

Interestingly, the AFM insulating phase likewise retains finite optical anisotropy despite the absence of gapless excitations. This persistence highlights that anisotropy is not an exclusive property of the semimetallic state but a generic outcome of rotational-symmetry breaking induced by SOC–magnetism coupling. Nevertheless, the magnitude and spectral profile of the anisotropy differ substantially between the insulating and semimetallic regimes, offering a clear spectroscopic distinction between them.

The QPI analysis further corroborates the anisotropic character of the electronic structure. The constant-energy contours acquire an elliptical form in the AFM–DSM phase, and the resulting QPI patterns reflect this band anisotropy for nonmagnetic impurities. In contrast, spin-polarized impurities selectively probe spin-resolved scattering channels, unveiling the underlying spin texture of the quasiparticles, while sublattice-selective scattering leads to measurable intensity variations. These findings suggest that spatially resolved STM measurements can serve as a powerful experimental tool to detect the anisotropic Dirac cones.

To conclude, we have investigated the anisotropy in the electronic properties of TSM with magnetic order and non-symmorphic symmetry. Despite a checkerboard-type AFM order, the optical conductivity differs in two orthogonal directions, which we believe originates from a subtle interplay between the particular orientation of magnetic moments and SOC. The anisotropic behavior is further seen to exist in the quasiparticle interference patterns when the impurity atoms are magnetic or non-magnetic. Thus, the present study bridges the gap between nonmagnetic topological semimetals and magnetically ordered correlated systems, revealing how controlled variations in SOC strength, Coulomb interaction, and magnetic orientation can be exploited to engineer diverse topological and transport phenomena.

Bibliography

[1] Coleman P *Introduction to Many-Body Physics* (Cambridge University Press, 2015)

[2] Hasan M Z and Kane C 2010 *Rev. Mod. Phys.* **82** 3045

[3] Qi X -L and Zhang S -C 2011 *Rev. Mod. Phys.* **83** 1057

[4] Kitaev A 2001 *Phys. -Usp.* **44** 131

[5] Alicea J 2012 *Rep. Prog. Phys.* **75** 076501

[6] Armitage N P, Mele E J, and Vishwanath A 2018 *Rev. Mod. Phys.* **90** 015001

[7] White R M *Quantum Theory of Magnetism,* 3rd ed. (Springer, Berlin, 2007).

[8] Dai P 2015 *Rev. Mod. Phys.* **87** 855

[9] Ran Y, Wang F, Zhai H, Vishwanath A, and Lee D -H 2009 *Phys. Rev. B* **79** 014505

[10] Richard P *et al* 2010 *Phys. Rev. Lett.* **104** 137001

[11] Basov D N, Averitt R D, Marel D van der, Dressel M, and Haule K 2011 *Rev. Mod. Phys.* **83** 471

[12] Dagotto E 1994 *Rev. Mod. Phys.* **66** 763

[13] Hu W Z, Dong J, Li G, Li Z, Zheng P, Chen G F, Luo J L, and Wang N L 2008 *Phys. Rev. Lett.* **101** 257005

[14] Nakajima M *et al* 2010 *Phys. Rev. B* **81** 104528

[15] Hoffman J E, McElroy K, Lee D -H, Lang K M, Eisaki H, Uchida S, and Davis J C 2002 *Science* **297** 1148

[16] Allan M P *et al* 2013 *Nat. Phys.* **9** 220

[17] Valenzuela B, Calderón M J, León G, and Bascones E 2013 *Phys. Rev. B* **87** 075136

[18] Mahan G D 1990 *Many particle physics*, Springer

[19] Balatsky A V, Vekhter I, and Zhu J -X 2006 *Rev. Mod. Phys.* **78** 373

[20] Hirschfeld P J, Vollhardt D, and Woelfle P 1986 *Solid State Commun.* **59** 111

Chapter 4

Dirac semimetallic state in the striped spin-density wave order

In the following chapter, we examine the possible existence of a Dirac semimetallic state with $(\pi, 0)$ spin-density wave (SDW) order in iron pnictides for realistic interaction parameters. By tuning the orbital splitting parameter, one can obtain a Dirac semimetallic state with Dirac points at the Fermi level while simultaneously suppressing additional Fermi pockets. We derive the necessary conditions—governed by the band slopes and their orbital character—that facilitate the persistence of a semimetallic state.

4.1 Introduction

Iron-based multiband superconductors have attracted considerable attention in recent times because of their complex band structure [1,2] and a variety of phases they can exhibit including unconventional superconductivity, nematic order, and other novel phases [3,4]. However, a renewed interest has been generated largely because of the signatures of topological states obtained in this class of superconducting materials [5,6].

Evidences of Dirac cones in the four-fold rotational symmetry broken metallic spin-density wave (SDW) state have been obtained through ARPES [7] and quantum oscillation measurements [8], which was predicated to be gapless [9]. The SDW state, with a collinear or striped magnetic order, consists of chains of magnetic moments pointing along the same direction while the moments of the neighboring chains are aligned along the opposite directions [10,11] [Fig. 4.1(a)]. This state, with an ordering wavevector $(\pi, 0)$, is considered widely to be a consequence of the inherent Fermi-surface instability as there exists a very good nesting in between the hole- and electron-pockets around Γ at $(0, 0)$ and X at $(\pi, 0)$ points, respectively [12–15].

The robustness of the Dirac cones and nodes originates from three symmetries associated with the metallic SDW state: collinearity of the magnetic order, inversion symmetry about an iron atom and another symmetry which combines together the

time reversal and inversion of magnetic moments [9]. These cones in the SDW state are not far away from the Fermi level [7]. Thus, there is a strong possibility of obtaining a Dirac semimetallic (DSM) state with SDW order by tuning parameters accessible through experiments, an aspect that remained unexplored in iron pnictides.

Evidence of topological features, such as dispersing surface states, has been obtained both in the paramagnetic and metallic SDW phases, making iron pnictides a promising platform for exploring topological semimetallic states [16]. A DSM state is characterized by a linear band crossing of conduction and valence bands at the Fermi level [17, 18]. The band-crossing point, also known as the Dirac point (DP), is four-fold degenerate. The massless fermion in the vicinity of the DP, with several novel electronic behavior [19–21], is described by the Dirac equation.

Therefore, in the following, we investigate the coexisting DSM with SDW order within a minimal two-orbital model of iron pnictides. Among several parameters whose variation do not affect the symmetries required for the stable Dirac cones, we demonstrate that the position of the Dirac points relative to the Fermi level can be controlled through the orbital splitting between the d_{xz} and d_{yz} orbitals, in addition to the band filling. Experimentally, the latter can be controlled by charge carrier doping but one cannot possibly remove the additional band crossings. In contrast, the former can be achieved by applying in-plane stress on the sample. Another consequence of orbital splitting is that the additional Fermi pockets, apart from the ones associated with the Dirac cones, may disappear so that the resulting state has only Dirac cones crossing the Fermi level leading to tiny Fermi pockets or DPs. In the latter case, the state is a semimetallic SDW state, for which we calculate necessary conditions dependent on orbital splitting and other parameters. In addition, linearized dispersions are obtained near the Dirac points and the nature of associated edge states is also studied.

4.2 Model and method

Iron pnictides exhibit a quasi-two-dimensional crystal structure, in which the square lattices of Fe and As atoms are interleaved such that the As atoms are slightly displaced above and below the center of each Fe square plane. As a result, the crystallographic unit cell contains two Fe and two As atoms. The Fe $3d$ orbitals hybridize with the As $4p$ orbitals, leading to a more intricate band structure. Band structure calculations show that the primary contributions to the density of states (DOS) at the Fermi level arise from the d_{xz}, d_{yz}, and d_{xy} orbitals [14]. In the following, we focus on a tight-binding Hamiltonian based on a minimal two-orbital model that incorporates

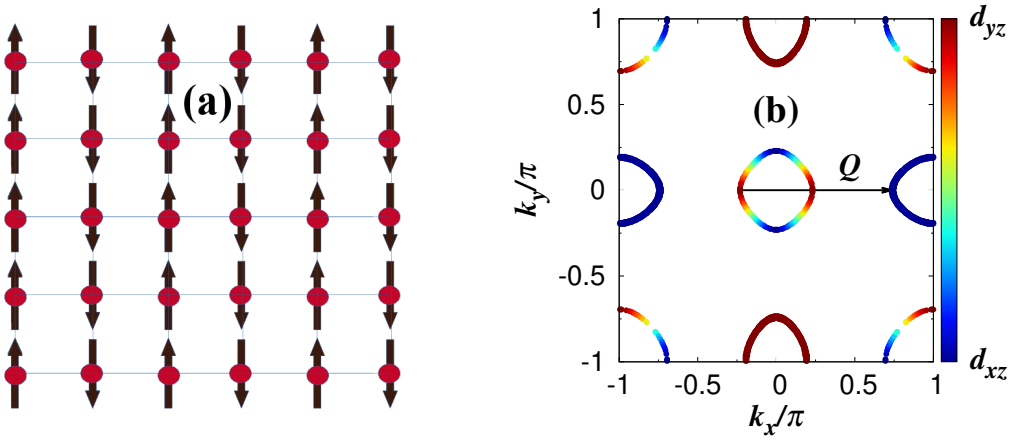

Figure 4.1: (a) Schematic representation of spin arrangements in the $(\pi, 0)$ SDW state. (b) Fermi surfaces in the unordered state within the two-orbital model. The nesting vector $\mathbf{Q} = (\pi, 0)$ connects the hole pocket at $\Gamma = (0, 0)$ to the electron pocket at $X = (\pi, 0)$. The color palette shows the variation of orbital-charge densities for the d_{xz} and d_{yz} orbitals.

only the d_{xz} and d_{yz} orbitals [13].

$$H_k = \sum_{\mathbf{ij}} \sum_{\mu,\nu} \sum_{\sigma} t_{\mathbf{ij}}^{\mu\nu} d_{\mathbf{i}\mu\sigma}^{\dagger} d_{\mathbf{j}\nu\sigma} - \delta \sum_{\mathbf{i},\sigma} (d_{\mathbf{i}xz\sigma}^{\dagger} d_{\mathbf{i}xz\sigma} - d_{\mathbf{i}yz\sigma}^{\dagger} d_{\mathbf{i}yz\sigma}) \tag{4.2.1}$$

Here, $t_{\mathbf{ij}}^{\mu\nu}$ represent the hopping amplitudes between orbitals μ and ν, including both intra-orbital and inter-orbital processes up to first- and second-nearest neighbors. The operators $d_{\mathbf{i}\mu\sigma}^{\dagger}$ and $d_{\mathbf{i}\mu\sigma}$ create and annihilate, respectively, an electron with spin σ in orbital μ at lattice site $\mathbf{i}$. The second term with parameter δ takes into account the orbital splitting (OS) between the two orbitals, which has been observed to exist up to a very high temperature even beyond the SDW transition temperature [22, 23].

The standard on site Coulomb interaction terms are

$$\begin{aligned} H_i &= U \sum_{\mathbf{i}\mu} n_{\mathbf{i}\mu\uparrow} n_{\mathbf{i}\mu\downarrow} + \left(U' - \frac{J}{2}\right) \sum_{\mathbf{i}} n_{\mathbf{i}\mu} n_{\mathbf{i}\nu} \\ &- 2J \sum_{\mathbf{i}} \mathbf{S}_{i\mu} \cdot \mathbf{S}_{i\nu} + J \sum_{\mathbf{i},\sigma} d_{\mathbf{i}\mu\sigma}^{\dagger} d_{\mathbf{i}\mu\bar{\sigma}}^{\dagger} d_{\mathbf{i}\nu\bar{\sigma}} d_{\mathbf{i}\nu\sigma} \end{aligned} \tag{4.2.2}$$

The first two contributions correspond to the intra-orbital and inter-orbital Coulomb interactions, respectively, where $n_{\mathbf{i}\mu\sigma} = d_{\mathbf{i}\mu\sigma}^{\dagger} d_{\mathbf{i}\mu\sigma}$ and $n_{\mathbf{i}\mu} = \sum_{\sigma} d_{\mathbf{i}\mu\sigma}^{\dagger} d_{\mathbf{i}\mu\sigma}$. The remaining two terms account for Hund's exchange interaction and the pair-hopping process, with the local spin operator defined as $S_{i\mu}^{j} = \sum_{\sigma\sigma'} d_{\mathbf{i}\mu\sigma}^{\dagger} \sigma_{\sigma\sigma'}^{j} d_{\mathbf{i}\mu\sigma'}$ and $\bar{\sigma}$ denotes the spin anti-parallel to σ. The relation $U = U' + 2J$ is ensured to keep the rotational symmetry intact.

Various interaction terms in the Hamiltonian can be meanfield decoupled in the

SDW state, which yield terms bilinear in the electron creation (or annihilation) operator for the SDW state. These terms, when the magnetic moments are oriented along z direction, are

$$\begin{aligned} H^i_{\rm mf} &= \frac{U}{2}\sum_{\mathbf{k}\mu\sigma}\Big(-s\sigma m_\mu + n_\mu\Big)d^\dagger_{\mathbf{k}\mu\sigma}d_{\mathbf{k}\mu\sigma} \\ &+ \Big(U' - \frac{J}{2}\Big)\sum_{\mathbf{k},\mu\neq\nu,\sigma} n_\nu d^\dagger_{\mathbf{k}\mu\sigma}d_{\mathbf{k}\mu\sigma} \\ &- \frac{J}{2}\sum_{\mathbf{k},\mu\neq\nu,\sigma}\sigma s m_\nu d^\dagger_{\mathbf{k}\mu\sigma}d_{\mathbf{k}\mu\sigma}. \end{aligned} \tag{4.2.3}$$

n_μ and m_μ are the orbital-resolved charge density and sublattice magnetization for the orbital μ, respectively. s and σ are equal to 1 (-1) for A (B) sublattice and $\uparrow$ spin ($\downarrow$ spin), respectively. The magnetic moments point in the upward (downward) direction in the sublattice A (B), where the magnetic moments are considered to be oriented along z direction, for simplicity. Thus, the unit cell in the SDW state consists of two atoms each one from the A and B sublattices. The summation over $\mathbf{k}$ is in the reduced Brillouin zone (Figs. 4.2(b) and (d)).

After combining the kinetic, OS, and meanfield decoupled interaction parts, the Hamiltonian for the (π, 0) SDW state in two sublattice basis is

$$\mathcal{H}_{mf} = \sum_{\mathbf{k}\sigma}\Psi^\dagger_{\mathbf{k}\sigma}(\hat{T}_{\mathbf{k}\sigma} + \hat{M}_{\mathbf{k}\sigma})\Psi_{\mathbf{k}\sigma}, \tag{4.2.4}$$

where the matrix elements $T^{\mu\nu}_{\mathbf{k}\sigma}$ and $M^{\mu\nu}_{\mathbf{k}\sigma} = -s\Delta_{\mu\nu} + \frac{5J-U}{2}n_\mu\delta^{\mu\nu}$ are the kinetic and interaction part contributions. s is $+/-$ on A/B sublattice. The electron-field operator is $\Psi^\dagger_{k\sigma} = (d^\dagger_{A\mathbf{k}1\sigma}, d^\dagger_{A\mathbf{k}2\sigma}, \cdots d^\dagger_{B\mathbf{k}1\sigma}, d^\dagger_{B\mathbf{k}2\sigma}, \cdots)$ and the exchange fields are $2\Delta_{\mu\nu} = U\, m_\mu\delta^{\mu\nu} + J\delta^{\mu\nu}\sum_{\mu\neq\nu} m_\nu$. The charge density n_μ and magnetization m_μ are calculated self consistently by diagonalizing the Hamiltonian matrix presented in Eq.(4.2.4). We have ignored the pair-hopping term as the contribution arising due to it is negligibly small.

4.3 Two-orbital model

In the two-orbital model, the meanfield SDW Hamiltonian in the two sublattice basis A with majority spin up and B with majority spin down is given by

$$H_{\rm MF} = \sum_{\mathbf{k},\sigma}\Psi^\dagger_{\mathbf{k}\sigma}H_{\rm SDW}(\mathbf{k})\Psi_{\mathbf{k}\sigma}, \tag{4.3.1}$$

where

$$H_{\rm SDW}(\mathbf{k}) = \begin{pmatrix} H^{\sigma}_{\alpha\alpha}(\mathbf{k}) & H^{\sigma}_{\alpha\beta}(\mathbf{k}) \\ H^{\sigma\dagger}_{\alpha\beta}(\mathbf{k}) & H^{\sigma}_{\beta\beta}(\mathbf{k}) \end{pmatrix} \tag{4.3.2}$$

$\Psi^{\dagger}_{\mathbf{k}\sigma} = (d^{\dagger}_{A\mathbf{k}\alpha\sigma}, d^{\dagger}_{B\mathbf{k}\alpha\sigma}, d^{\dagger}_{A\mathbf{k}\beta\sigma}, d^{\dagger}_{B\mathbf{k}\beta\sigma})$, where the sub- or super-scripts α and β are used to denote the orbitals d_{xz} and d_{yz}, respectively, throughout. The matrices in (4.3.2) are

$$H^{\sigma}_{\alpha\alpha}(\mathbf{k}) = \begin{pmatrix} \epsilon^{\alpha\alpha}_{y} - \sigma\Delta_{\alpha} - \delta + N_{\alpha} & \epsilon^{\alpha\alpha}_{x} + \epsilon^{\alpha\alpha}_{xy} \\ \epsilon^{\alpha\alpha}_{x} + \epsilon^{\alpha\alpha}_{xy} & \epsilon^{\alpha\alpha}_{y} + \sigma\Delta_{\alpha} - \delta + N_{\alpha} \end{pmatrix}, \tag{4.3.3}$$

$$H_{\alpha\beta}(\mathbf{k}) = \begin{pmatrix} 0 & \epsilon^{\alpha\beta}_{xy} \\ \epsilon^{\alpha\beta}_{xy} & 0 \end{pmatrix}, \tag{4.3.4}$$

and δ has a positive sign in $H^{\sigma}_{\beta\beta}(\mathbf{k})$. The intra- and inter-orbital hopping parameters along x and y directions for different orbitals are given by

$$\begin{aligned} \epsilon^{\alpha\alpha}_{x} &= -2t_1 \cos k_x, \;\; \epsilon^{\beta\beta}_{x} = -2t_2 \cos k_x \\ \epsilon^{\beta\beta}_{y} &= -2t_1 \cos k_y, \;\; \epsilon^{\alpha\alpha}_{y} = -2t_2 \cos k_y \\ \epsilon^{\alpha\alpha}_{xy} &= \epsilon^{\beta\beta}_{xy} = -4t_3 \cos k_x \cos k_y \\ \epsilon^{\alpha\beta}_{xy} &= -4t_4 \sin k_x \sin k_y \end{aligned} \tag{4.3.5}$$

The hopping parameters t_1 and t_2 link similar orbitals corresponding to the nearest neighbor σ and π bonds respectively, while the the next-nearest neighbour hopping parameters t_3 and t_4 denote the overlap amplitude between two similar and dissimilar orbitals, respectively. Various hopping parameters considered for our calculations are t_1 = -1.0, t_2 = 1.3, $t_3 = t_4$ = -0.85 [13]. Herefrom, we set $|t_1|$ as the unit of energy. The exchange field $\Delta_{\alpha/\beta}$ and charge-density dependent $N_{\alpha/\beta}$ are given by

$$\Delta_{\alpha/\beta} = (U m_{\alpha/\beta} + J m_{\beta/\alpha})/2, \;\; N_{\alpha/\beta} = (5J - U) n_{\alpha/\beta}/2 \tag{4.3.6}$$

where $m_{\alpha/\beta}$ and $n_{\alpha/\beta}$ are magnetization and charge density for $d_{xz/yz}$ orbital, respectively. The Hamiltonian $H_{\rm SDW}$ is invariant under two symmetry operations: (i) $T' = \mathcal{T}\mathcal{S}$, time reversal symmetry ($\mathcal{T}$) combined with spin reversal symmetry ($\mathcal{S}$) and (ii) inversion symmetry (P). Thus, $T' H_{\rm SDW}(\mathbf{k}) T'^{-1} = H_{\rm SDW}(\mathbf{k})$ and $P H_{\rm SDW}(\mathbf{k}) P^{-1} = H_{\rm SDW}(\mathbf{k})$.

We will first examine the parameter space in the theory of SDW state to search for the DSM state coexisting with SDW state. All the on-site Coulomb interaction parameters are fixed unless stated otherwise. We have chosen $U/|t_1| \sim 4$ or $U \sim W/3$ with W being the bandwidth [24] and $J \sim 0.18U$ nearly in the middle of the range $0.15U \lesssim J \lesssim 0.25U$ in accordance with various estimates [25, 26]. The chemical

potential is fixed throughout so that the band filling corresponds to the total electronic occupancy $n = 2$ per site, i.e., half filling in the two-orbital model.

4.3.1 Bulk dispersion

Fig. 4.2 shows the quasiparticle dispersion and Fermi surface in the SDW state for different values of OS parameter δ. For $\delta = 0$ [Fig. 4.2(a)], there exist two pairs of Dirac cones D_1 and D_2, D_1 along $(0,0) \rightarrow (\pi/2, 0)$ and D_2 along $(0,\pi) \rightarrow (\frac{\pi}{2}, \pi)$ directions. Former is below the Fermi level while the latter one is above it. The orbital distribution of the Fermi pockets are largely similar for both the pair of Dirac cones. As noticed, the face of the pockets towards $k_x = 0$ is dominated by d_{xz} orbital whereas by d_{yz} orbital towards $k_x = \pm\pi/2$ [Fig. 4.2(b)].

One of the parameters which can control the location of Dirac cones with respect to the Fermi level is the band filling. However, it will shift both the Dirac cones either up or down together so that the Fermi pocket associated with one of the cones will increase in size while the other will decrease. Thus, the DSM-SDW state cannot be obtained by merely doping charge carriers. On the other hand, we find that by increasing OS parameter δ, D_1 and D_2 simultaneously can be pushed up and down, respectively, so that both the associated DPs may approach the Fermi level together, as required to achieve the coexisting DSM with SDW order [Fig. 4.2(c) and (e)]. Fig. 4.2(d) shows the Fermi pockets obtained for $\delta \sim 0.2$, where both DPs associated with D_1 and D_2 can be seen at the Fermi level as indicated by the Fermi pockets turning into the Fermi points in the reduced-Brillouin zone.

The shifting up or down of the DPs can be understood with the help of the slope of the bands dominated either by the d_{xz} orbital or by the d_{yz} orbital, which cross each other to generate DPs. For D_1, the ratio R of the absolute value of the slope of the bands dominated by d_{xz} orbital and d_{yz} orbital is $R > 1$. Thus, a positive δ, which lowers the energy of d_{xz} orbital and elevate the energy of d_{yz} orbital, will shift D_1 upward. Similarly, it may be noted that $R < 1$ for D_2. Therefore, when the energy of d_{xz} orbital is lowered, the band dominated by d_{xz} orbital will shift down, which will, in turn, bring down D_2. Both D_1 and D_2 approach Fermi level when the splitting δ increases. In this way, the location of Dirac points can be controlled with the help of OS parameter δ. The bandwidth is $W \sim 4$eV for the iron-based superconductors as estimated by various bandstructure calculations [27]. In the two-orbital model, $W = 12t_1$ in terms of t_1, which on comparison with 4eV yields $t_1 \sim 350$meV. Therefore, $\delta \sim 0.2t_1 \sim 70$ meV which is not very large in comparison to what has been reported experimentally in the states with the broken four-fold rotation symmetry [22].

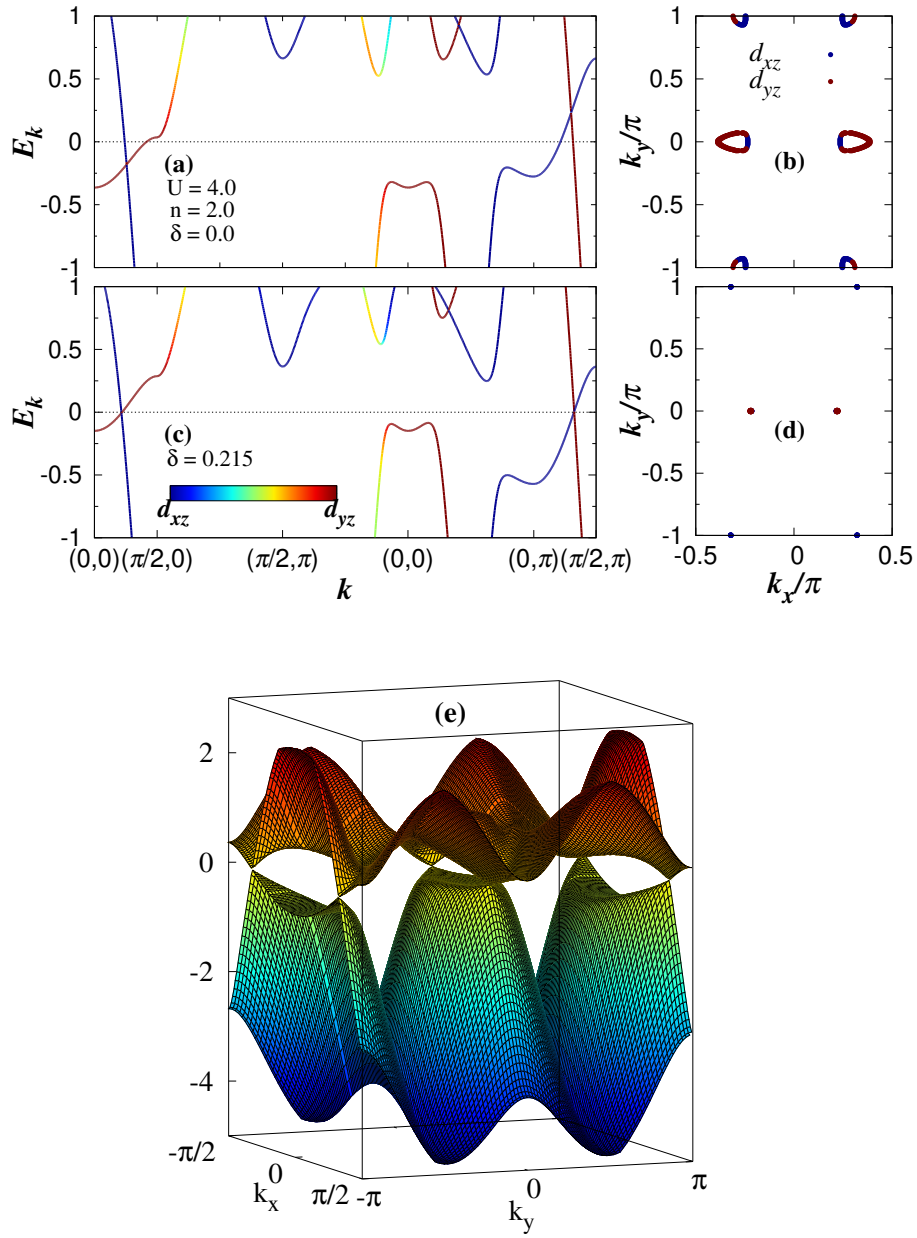

Figure 4.2: Energy dispersions along the high-symmetry directions in the SDW state with $U = 4$ and $J = 0.18U$ when the OS parameters are (a) $\delta = 0.0$ and (c) $\delta = 0.215$. The varying color scheme used for the dispersion curve represents orbital-charge density. Corresponding Fermi surfaces are shown in figures (b) and (d), respectively. The same color scheme also shows the dominating orbital along the Fermi surfaces. (e) The energy dispersion in the reduced Brillouin zone.

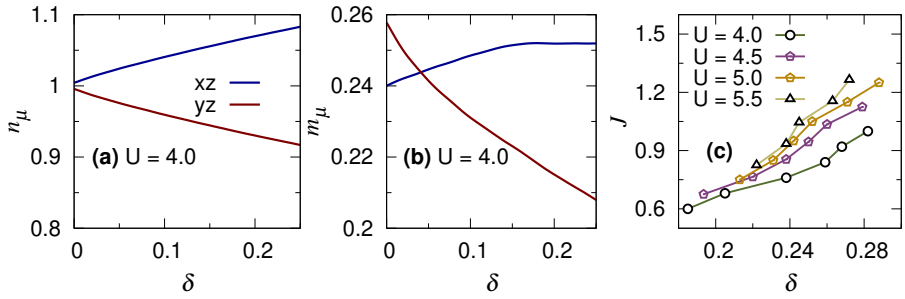

Figure 4.3: Orbital-resolved (a) charge density and (b) magnetization as functions of OS parameter δ between d_{xz} and d_{yz} orbitals in the ordered state for $U = 4$ and $J = 0.18U$. (c) Self-consistently obtained DSM-SDW states for various Us in J-δ space for band filling $n = 2$.

Fig. 4.3 shows self-consistently obtained orbital-resolved magnetization and charge density as functions of OS parameter δ. As expected, the d_{xz} and d_{yz} orbital charge density increases and decreases with δ, respectively. However, the behavior of magnetization is in contrast with what is expected conventionally. When the orbital filling continues to increase beyond unity, the magnetization is expected to decrease. Similarly, when the orbital filling continues to drop below unity then the magnetization is expected to rise. On the contrary, one notices that the d_{xz} orbital magnetization m_{xz} first increases slightly and then becomes nearly constant whereas m_{yz} shows a relatively sharper decline. This arises because of a subtle interplay between band-structure and correlation effect, as the largest interaction $U \sim 4$ is not in the strong but intermediate coupling regime. The itinerant character of d_{xz} orbital electrons appears to be reduced as the orbital is pushed further below the Fermi level with increased orbital splitting.

The self-consistently obtained curves denoting the existence of DSM-SDW state for different Us are shown in the J-δ space [Fig. 4.3(c)] subjected to the condition $U = U' + 2J$ to ensure the rotational symmetry. Then, for a given U, the parameters J and δ are varied so that the Dirac points D_1 and D_2 appear at the Fermi energy. It may be noted that for all Us considered, J increases with δ within the range $0.15U \lesssim J \lesssim 0.25U$. The range of J is dependent on U, for this reason, J is in the unit of $|t_1|$ in the plot. We note that the range of δ shrinks as U increases, which implies more sensitivity to any change in δ for higher U. However, for $U = 4$ a value close to various estimates, we find a relatively broad range of δ with value extending from $\delta = 0.18$ to 0.27.

4.3.2 DSM-SDW conditions

In order to obtain the DSM-SDW state, the self-consistency should be achieved subjected to conditions, which will be discussed below. First of all, we focus along the direction $k_y = 0$ or π in the Brillouin zone, where $H_{\alpha\beta}$ becomes a null matrix. Therefore, $H_{\rm MF}$ takes a block diagonal form with two block Hamiltonians $H_{\alpha\alpha}(\mathbf{k})$ and $H_{\beta\beta}(\mathbf{k})$ corresponding to each orbital with size 2×2 matrices, which can be readily diagonalized. The energy eigenvalues are given by

$$E^x_{r\pm} = (\epsilon^{rr}_y \pm \delta + N_r - \mu) \pm \sqrt{(\epsilon^{rr}_x + \epsilon^{rr}_{xy})^2 + \Delta^2_r} \tag{4.3.7}$$

with setting $k_y = 0$ or π. r refers to α or β orbitals. Superscript x denotes the fact that the energy is essentially a function of k_x only for $k_y = 0$ or π, while subscript r merely indicates that the dispersion is dominated by either of the orbitals. Two dispersions $E^x_{\alpha+}$ and $E^x_{\beta-}$ cross each other at the Fermi level when $E_{\alpha+} = E_{\beta-} = 0$, which requires

$$\begin{aligned} \cos k^0_{x1/x2} &= \frac{\sqrt{(\mp 2t_2 - \delta + N_\alpha - \mu)^2 - (\Delta_\alpha)^2}}{2(t_1 \pm 2t_3)} \\ &= \mp \frac{\sqrt{(\mp 2t_1 + \delta + N_\beta - \mu)^2 - (\Delta_\beta)^2}}{2(t_2 \pm 2t_3)}. \end{aligned} \tag{4.3.8}$$

Here, k^0_{x1} and k^0_{x2} give the locations of DPs associated with the Dirac cones D_1 and D_2 along $\Gamma(0,0)$-X$(\frac{\pi}{2},0)$ and X$'(0,\pi)$-M$(\frac{\pi}{2},\pi)$ directions, respectively. It may also noted that $k^0_{y1} = 0$ and $k^0_{y2} = \pi$.

4.3.3 Linearized dispersion

Using Taylor expansions of $E^x_{\alpha+}$ and $E^x_{\beta-}$ around DPs along k_x with the help of (4.3.5), one obtains linearized dispersion $E^x_{r\mp} = c^x_{r1/r2} q_x$, where the constant $c^x_{r1/r2}$ is given by

$$\begin{aligned} c^x_{\alpha 1/\alpha 2} &= \mp \frac{2(t_1 \pm 2t_3)^2}{|\mp 2t_2 - \delta + N_\alpha - \mu|} \sin 2k^0_x \\ c^x_{\beta 1/\beta 2} &= \pm \frac{2(t_2 \pm 2t_3)^2}{|\mp 2t_1 + \delta + N_\beta - \mu|} \sin 2k^0_x. \end{aligned} \tag{4.3.9}$$

Note that the subscript 1 and 2 in $c^x_{\alpha 1/\alpha 2}$ refer to the DPs D_1 and D_2, respectively.

$H_{\rm SDW}$ is not in the block-diagonal form along k_y-direction. Moreover, the Hamiltonian for $\uparrow$-spin electron is two-fold degenerate at the DPs. Therefore, the degenerate

perturbation theory yields the following corrections to the energies near DPs along k_y

$$E_{\pm}^{y} = \pm\left(\frac{\Delta_\alpha - e_\alpha}{b_\alpha} + \frac{\Delta_\beta + e_\beta}{b_\beta}\right)\epsilon_{xy}^{\alpha\beta} \tag{4.3.10}$$

when $\epsilon_{xy}^{\alpha\beta}$ is very small. Note that the subscript r has been dropped here because the band along k_y is not far away from an even mixture of both the orbitals. $b_\alpha = \epsilon_x^{\alpha\alpha} + \epsilon_{xy}^{\alpha\alpha}$ and $e_\alpha = \sqrt{b_\alpha^2 + \Delta_\alpha^2}$. The linear dependence of the energy dispersion near the DP is readily obtained from $\epsilon_{xy}^{\alpha\beta}$, where $\sin q_y$ can be approximated by q_y for small q_y so that $E_{r1/r2}^{y} = d_{r1/r2} q_y$. $d_{r1/r2}$ is a constant given by

$$d_{r1/r2} = \pm 4t_4 \sin k_x^0 (f_{\alpha 1/\alpha 2} + f_{\beta 1/\beta 2}), \tag{4.3.11}$$

where

$$\begin{aligned} f_{\alpha 1/\alpha 2} &= \frac{\Delta_\alpha - |\mp 2t_2 - \delta + N_\alpha - \mu|}{\sqrt{(\mp 2t_2 - \delta + N_\alpha - \mu)^2 - \Delta_\alpha^2}} \\ f_{\beta 1/\beta 2} &= \frac{\Delta_\beta + |\mp 2t_1 + \delta + N_\beta - \mu|}{\sqrt{(\mp 2t_1 + \delta + N_\beta - \mu)^2 - \Delta_\beta^2}}. \end{aligned} \tag{4.3.12}$$

Upper and lower sign correspond to the Dirac cones D_1 and D_2, respectively. Eqns. (4.3.7)-(4.3.11) provide conditions for the coexistence of Dirac semimetallic and SDW state as well as the linear energy dispersion in the vicinity of DPs. Finaly, the effective model Hamiltonian in the vicinity of Dirac points is given by

$$\begin{aligned} H_{\mathrm{SDW}}(\mathbf{k_0} + \mathbf{q}) = &\frac{1}{2}(-2t_2 \cos k_y^0 + N_\alpha)(\tau_0 + \tau_3) \otimes s_0 \\ &+ \frac{1}{2}(-2t_1 \cos k_y^0 + N_\beta)(\tau_0 - \tau_3) \otimes s_0 \\ &- \frac{1}{2}\sigma\Delta_\alpha(\tau_0 + \tau_3) \otimes s_3 - \frac{1}{2}\sigma\Delta_\beta(\tau_0 - \tau_3) \otimes s_3 \\ &- (\cos k_x^0 - q_x \sin k_x^0)(t_1 + 2t_3 \cos k_y^0)((\tau_0 + \tau_3) \otimes s_1) \\ &+ \frac{1}{2}(t_2 + 2t_3 \cos k_y^0)((\tau_0 - \tau_3) \otimes s_1) \\ &- \delta\tau_3 \otimes s_0 - 4t_4 q_y \sin k_x^0 \tau_1 \otimes s_1, \end{aligned} \tag{4.3.13}$$

where $k_y^0 = 0$ or π, k_x^0 is given by Eq. (4.3.8), and s and τ are the Pauli matrices in the sublattice and orbital bases, respectively.

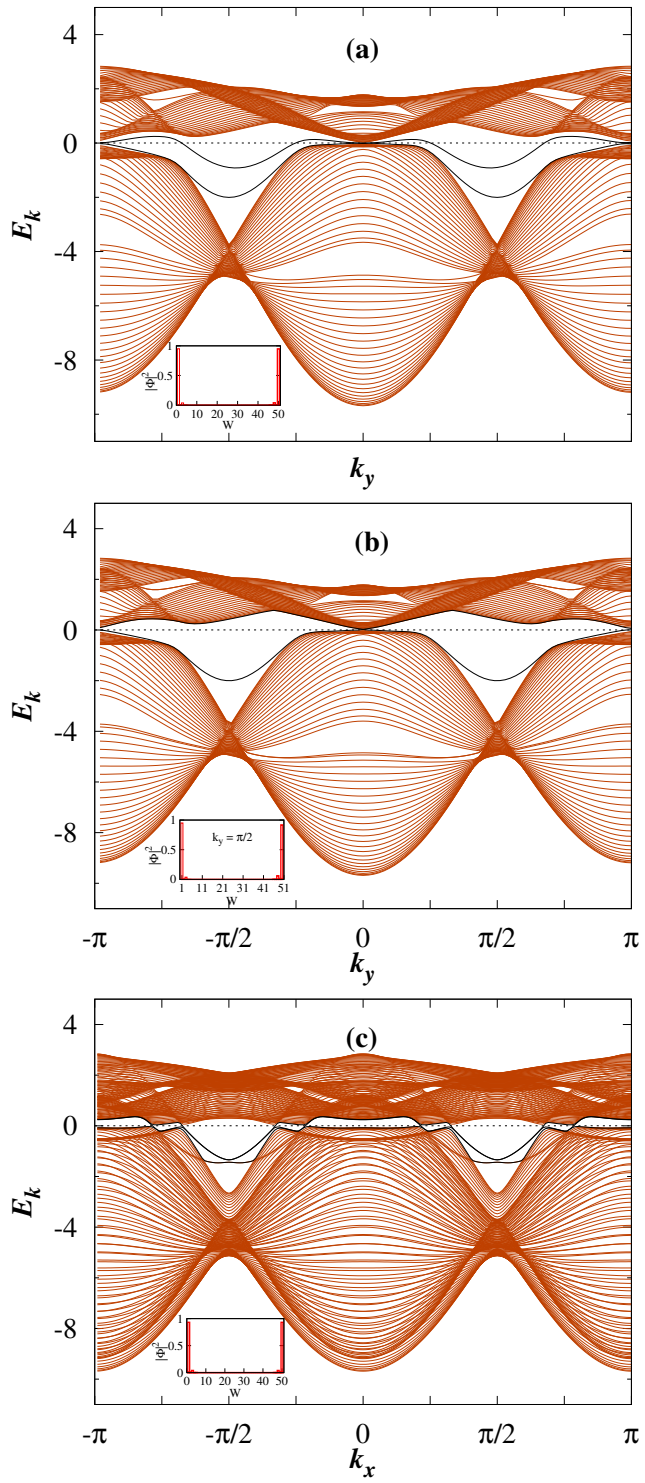

Figure 4.4: Energy bands for the DSM-SDW state for a ribbon of width (a) $W = 50$, (b) $W = 51$ considered along x-direction and (c) $W = 50$ considered along y-direction for $U = 4$ and $J = 0.18U$, for which, the orbital charge densities are $n_\alpha = 1.14$ and $n_\beta = 0.86$ whereas the magnetic-exchange fields are $\Delta_\alpha = 0.58$ and $\Delta_\beta = 0.53$. The inset shows the edge state density over different chains for $k_y = \pi/2$.

4.3.4 Edge states

An edge state may exhibit behavior that can differ from those of the bulk bands as in the case of topological insulator where the bulk bands are gapped while charge transport occurs by topologically protected surface states [28]. In iron pnictides, there exists localized edge states in the high temperature phase even without long-range order [29]. It may be noted that these edge states, nearly degenerate, are not associated with any Dirac cones, which are absent in the paramagnetic state. Similar edge states are also obtained in the metallic as well as SDW states [16]. For a given k_y, these edge states are bonding and antibonding mixture of states localized at the edges of a ribbon/strip extending along y direction. They result from the fact that a one-dimensional Hamiltonian for a given k_y can be deformed continuously to one which has a topologically protected winding number, while the edges states are preserved in the deformation process.

Next, we examine the edge states in the DSM-SDW state with ribbons oriented either along x or y directions. First, a ribbon of width W (W atomic sites) lying along y direction is considered so that k_y is a good quantum number. The ribbon Hamiltonian with dimension $2W \times 2W$ is given by

$$H_{Rby}(k_y) = \begin{pmatrix} H_+ & H' & O & \cdots \\ H'^\dagger & H_- & H' & \cdots \\ O & H'^\dagger & H_+ & \cdots \\ \vdots & \vdots & \vdots & \ddots \end{pmatrix} \tag{4.3.14}$$

where

$$H_\pm(k_y) = \begin{pmatrix} \epsilon_y^{\alpha\alpha} \mp \Delta_\alpha - \delta + N_\alpha - \mu & 0 \\ 0 & \epsilon_y^{\beta\beta} \mp \Delta_\beta + \delta + N_\beta - \mu \end{pmatrix}$$

and

$$H'(k_y) = \begin{pmatrix} -t_1 - 2t_3 \cos k_y & -2it_4 \sin k_y \\ -2it_4 \sin k_y & -t_2 - 2t_3 \cos k_y \end{pmatrix}.$$

Similarly, when the ribbon's length is oriented along x direction so that k_x is a good quantum number, the Hamiltonian $H_{Rbx}(k_x)$ with size $4W \times 4W$ has a form similar to that of H_{Rby}. However, $H_\pm$ and H' have size 4×4 instead. These matrices are given by

$$H_+ = H_- = H = \begin{pmatrix} h_{AA} & h_{AB} \\ h_{BA} & h_{BB} \end{pmatrix}$$

with

$$h_{AA}(k_x) = \begin{pmatrix} -\Delta_\alpha - \delta + N_\alpha - \mu & 0 \\ 0 & -\Delta_\beta + \delta + N_\beta - \mu \end{pmatrix}$$

and

$$h_{AB}(k_x) = \begin{pmatrix} \epsilon_x^{\alpha\alpha} & 0 \\ 0 & \epsilon_x^{\beta\beta} \end{pmatrix}$$

while

$$H'(k_x) = \begin{pmatrix} -t_2 & 0 & -2t_3 \cos k_x & -2it_4 \sin k_x \\ 0 & -t_1 & -2it_4 \sin k_x & -2t_3 \cos k_x \\ -2t_3 \cos k_x & -2it_4 \sin k_x & -t_2 & 0 \\ -2it_4 \sin k_x & -2t_3 \cos k_x & 0 & -t_1 \end{pmatrix}.$$

There exists nearly degenerate two edge states for the ribbon in the paramagnetic state which may or may get clearly separated in the presence of magnetic order depending on whether W is odd or even.

Figures 4.4(a) and 4.4(b) illustrate the edge-state dispersion for ribbons oriented along the y-direction in the $(\pi, 0)$ spin-density-wave state. In this geometry, adjacent chains belong to alternating sublattices. For an even number of chains ($W = 50$), the two end chains belong to opposite sublattices and experience magnetic exchange fields opposite in sign. In this case, one of the edge states is below the Fermi level, while the other one crosses the Fermi level several times. The spatial profile of the probability amplitude is shown in the inset panel of Fig. 4.4(a), which confirms its nature as an edge state.

For an odd number of chains ($W = 51$), the two edge states cross the Fermi level at $k_y = 0$ and $\pm\pi$ (Fig. 4.4(b)). In this case, both terminating chains belong to the same sublattice and experience identical magnetic exchange fields. This factor is responsible for the differences in $W = 50$ and $W = 51$ cases. These edge states in the DSM-SDW state are dispersing unlike those in graphene, which are flat [30].

Fig. 4.4(c) shows the dispersion in a ribbon oriented along the x direction. As expected, they are symmetric about $k_x = -\pi/2$ and $\pi/2$ because of the two-sublattice structure along the ribbon extending infinitely along x. None of the edge-state dispersion is flat and both can be noticed to cross the Fermi surface. It is worthwhile to note that a flat dispersion in graphene is associated with the chiral symmetry, when only nearest-neighbor hopping is considered. When the next-nearest neighbor hopping is incorporated as required in real graphene, the particle-hole symmetry is broken, and the chiral symmetry is removed [17]. The tight-binding model considered in the present study does not exhibit any particle–hole symmetry.

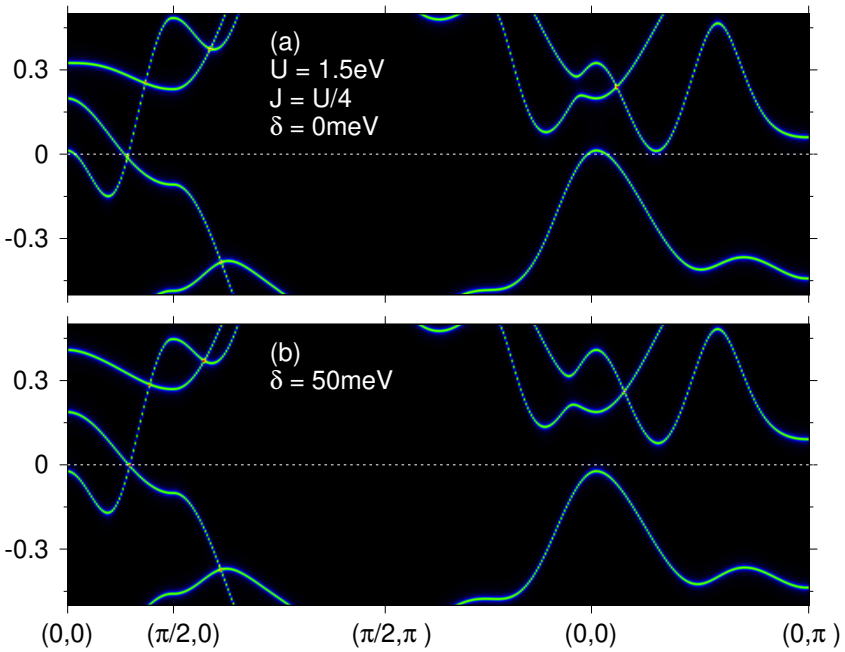

Figure 4.5: Electron dispersion in the $(\pi, 0)$ SDW state of five-orbital model of Graser *et al.* when (a) $\delta = 0$ (b) $\delta = 50$meV, where $U = 1.5eV$ and $J = 0.25U$. The hole pocket at Γ disappears in the presence of OS δ =50meV.

4.4 DSM-SDW state in five-orbital model

Finally, we discuss DSM-SDW state in a five-orbital model which describes the band structure more realistically. We consider the five-orbital model due to Graser *et al.* In the unordered state, it has similarities as well as differences from the two-orbital model. There is a hole pocket around Γ and an electron pocket around X while the hole pocket around M is absent. The electron pocket is mostly dominated by d_{xy} orbital [13, 14].

Fig. 4.5 shows the electronic dispersion in a self-consistently obtained SDW state for $U = 1.5$eV and $J = 0.25U$ with and without orbital splitting. The ratio $U/W \sim 0.25$ with $W \sim 6$eV being bandwidth is in accordance with various estimates [24]. The OS parameter δ is taken to be 50meV, which is nearly of similar order as observed in the experiments. The evidence of the splitting already present in the high-temperature phase comes from transport [31], ARPES [32, 33] and magneto-torque measurements [23].

It may be noted that unlike the two-orbital model, there is a large hole pocket around Γ and a tiny hole pocket located not far away from Γ along Γ-X. With increasing OS parameter δ, which lowers the energy of d_{xz} orbital, the d_{xz}-dominated bands such as the hole pocket around Γ will be pushed down below the Fermi level as shown in Fig. 4.5 (a) and (b). There are two important differences from the two-orbital

model with regard to the Dirac cone. First, the difference in magnitude of slopes of the crossing bands at DPs are not as large as in the two-orbital model. Second, along k_x, one of the crossing bands is largely dominated by d_{xz} while the other one by d_{xy} orbital unlike the d_{yz} orbital. Therefore, when δ is changed, the corresponding shift in the positions of DPs is relatively small in comparison to the two-orbital model. However, the DPs are already very close to the FS even in the absence of OS. Thus, the important role of OS δ is to suppress the hole pocket around Γ point, which is necessary to obtain the DSM-SDW state.

4.5 Summary

In the two-orbital model, two pairs of Dirac cones in the SDW state are located away from the Fermi surface. While one pair is above, the other one is below. The separation of these pairs with respect to the Fermi surface can be minimized with the help of OS. Inclusion of OS pushes up the Dirac cone found below the Fermi level and pushes down the one above it, which is possible because of a sharp difference in the slopes of crossing bands dominated largely by a single orbital. For a given OS parameter, an overall small shift away from the Fermi surface may also occur despite both pairs of DPs being at the same energy level. However, such a shift can be overcome by either doping holes or electrons. The signature of shifting of DPs can be observed through various experiments such as transport measurements, quantum oscillation, ARPES etc. [31].

In the current work, a detailed study of the DSM-SDW state was carried out in the two-orbital model because of its simplicity, as it allows for obtaining conditions for the DSM-SDW state in an analytical form. However, DSM-SDW state can also exist in a more realistic five-orbital model in a region of interaction and OS parameter space, which is illustrated for such a particular set within the range in accordance with various estimates. However, there are several important differences from the two-orbital model in terms of orbital content of the Dirac cone and presence of hole pocket around Γ point. Another major difference exists in terms of the number of pairs of Dirac cones. There is only one pair of Dirac cones close to the Fermi level in the five-orbital model [7], for which, it may relatively be easier to bring DPs at the Fermi level. Overall, we find that, the OS pushes hole pocket around Γ below and secondly it may also shift the DPs. As a result, it is not only possible to control electronic properties including the charge transport by tuning the OS, thus, in turn, regulate the contribution of Dirac cone but it is also feasible to realize DSM-SDW state.

Our study has focused on $T = 0$ K case. With an increase in temperature, the orbital-resolved magnetic moments will decrease. In that case, the location of DP will be shifted. Then, δ for having the DP at Fermi level and the coefficient of linear momentum in the expansion of the quasiparticle energy will be modified. These changes can again be described with the help of equations (4.3.7)-(4.3.12), which involve $\Delta_{\alpha/\beta}$ dependent on the magnetic moments. It may be noted that the band shift and renormalization caused by the spin fluctuations can also lead to the disappearance of relatively smaller hole pockets in the electron overdoped region [34]. But, in the undoped iron pnictides, the size of hole pocket is nearly as large as that of the electron pocket. The renormalization caused by the spin fluctuations is expected to introduce minor change in the hole pocket. Thus, correspondingly, a small shift of DPs as well as a small change in the quasiparticle velocity may occur.

In summary, we have examined the possible existence of spin-density wave state with Dirac points at the Fermi level in iron pnictides such that the state is essentially a Dirac semimetal without any other band crossings. We find that such a state indeed can be obtained in the presence of finite OS. While the interaction parameters are not tunable experimentally, charge carrier doping may shift entire bands up or down, the OS of otherwise degenerate d_{xz} and d_{yz} orbitals, on the other hand, can suppress other bands crossing the Fermi level while leaving the Dirac points close to the Fermi level. Thus, the OS, tunable experimentally with the help of in-plane mechanical stress, can be used to modify the electronic states near the Fermi surface in order to control the electronic properties as well as in obtaining DSM-SDW state. A semimetallic state with magnetic order considered here can be used to explore low-energy collective excitations to gain insight into the role of Dirac cones and nodes in correlated systems.

Bibliography

[1] Andersen O K and Boeri L 2011 *Ann. Phys.* **523** 8

[2] Kordyuk A A, Zabolotnyy V B, Evtushinsky D V, Yaresko A N, Buechner B, and Borisenko S 2013 *J. Supercond. Nov. Magn.* **26** 2837

[3] Stewart G R 2011 *Rev. Mod. Phys.* **83** 1589

[4] Kordyuk A A 2012 *Phys.* **38** 888

[5] Zhang P Wang *et al* 2019 *Nat. Phys.* **15** 41

[6] Zhang P *et al* 2018 *Science* **360** 182

[7] Richard P *et al* 2010 *Phys. Rev. Lett.* **104** 137001

[8] Sutherland M *et al* 2011 *Phys. Rev. B* **84** 180506(R)

[9] Ran Y, Wang F, Zhai H, Vishwanath A, and Lee D -H 2009 *Phys. Rev. B* **79** 014505

[10] Lumsden M D and Christianson A D 2010 *J. Phys.: Condens. Matter* **22** 203203

[11] Johnston D C 2010 *Adv. Phys.* **59** 803

[12] Korshunov M M and Eremin I 2008 *Europhys. Lett.* **83** 67003

[13] Raghu S, Qi X -L, Liu C -X, Scalapino D J, Zhang S -C 2008 *Phys. Rev. B* **77** 220503(R)

[14] Graser S, Maier T A, Hirschfeld P J and Scalapino D J 2010 *New J. Phys.* **11** 025016

[15] Brydon P M R, Daghofer M and Timm C 2011 *J. Condens. Mat. Phys.* **23** 246001

[16] Lau A and Timm C 2013 *Phys. Rev. B* **88** 165402

[17] Neto A H Castro, Guinea F, Peres N M R, Novoselov K S, and Geim A K 2009 *Rev. Mod. Phys.* **81** 109

[18] Hasan M Z and Kane C L 2010 *Rev. Mod. Phys.* **82** 3045

[19] Li P, Wu W, Wen Y, Zhang C, Zhang J, Zhang S, Yu Z, Yang S A, Manchon A, and Zhang X -X 2018 *Nat. Commun.* **9** 3990

[20] Wang Q, Li C -Z, Ge S, Li J -G, Lu W, Lai J, Liu X, Ma J, Yu D P, Liao Z -M, and Sun D 2017 *Nano Letters* **17** 834

[21] Lundgren R, Laurell P, and Fiete G A 2014 *Phys. Rev. B* **90** 165115

[22] Yi M *et al* 2011 *PNAS* **108** 6878

[23] Kasahara S *et al* 2012 *Nature* **486** 382

[24] Yang W L *et al* 2009 *Phys. Rev. B* **80** 014508

[25] Miyake T, Nakamura K, Aarita R and Imada M 2010 *J. Phys. Soc. Jpn.* **79** 044705

[26] Ishida H and Liebsch A 2010 *Phys. Rev. B.* **81** 054513

[27] Ikeda H, Arita R and Kuneš J 2010 *Phys. Rev. B* **81** 054502

[28] Cai S *et al* 2018 *npj Quant. Mater.* **3** 62

[29] Lau A and Timm C 2013 *Phys. Rev. B* **88** 165402

[30] Bernevig B Andrea *Topological Insulators and Topological superconductors* (Princeton University Press, 2013)

[31] Blomberg E C, Tanatar M A, Fernandes R M, Mazin I I, Shen B, Wen H -H, Johannes M D, Schmalian J, and Prozorov R 2013 *Nat. Commun.* **4** 1914

[32] Yi M *et al* 2011 *Proc. Natl. Acad. Sci. USA* **108** 6878

[33] Yi M *et al* 2019 *Phys. Rev. X* **9** 041049

[34] Rodriguez J P and Ronald M 2018 *J. Phys. Commun.* **2** 105011

Chapter 5

Collective excitations in the DSM state with striped spin-density wave order

This chapter focuses on the study of electronic properties by examining the nature of collective excitations by theoretically exploring quasiparticle interference and optical conductivity in the DSM state with $(\pi, 0)$ *spin-density wave order.*

5.1 Introduction

The anisotropic electronic properties in the SDW state of iron pnictides with ordering wave vector $(\pi, 0)$, whose evidence have been obtained with the help of experiments such as angle-resolved photoemission spectroscopy (ARPES) [3], transport measurements [1, 5], scanning tunneling microscopy (STM) [6], etc., which are not unusual as the four-fold rotational symmetry is already broken. However, the nature of anisotropy, especially, improved conductivity along the antiferromagnetic instead of ferromagnetic direction is in contradiction with conventional understanding.

In the SDW state, the emergence of anisotropic transport properties has conventionally been attributed to the orbital-weight redistribution along the reconstructed Fermi surface [10]. It can result into anisotropic impurity scattering [11, 12]. However, the quasiparticle interference (QPI) patterns obtained through the STM measurements [6, 13, 14] consist of nearly one-dimensional structure with a length scale of the order $\sim 6a - 8a$, where a is the lattice constant. Moreover, the anisotropic feature is not limited to the QPI patterns and transport properties, where a major contribution comes from the electronic states in the vicinity of the Fermi level; the optical spectra also show the anisotropy existing up to photonic energies ~ 2eV [17]. Various theoretical studies attribute the anisotropic patterns in the SDW state to the reconstructed electronic structure in the SDW state [11, 12].

Despite significant progress made in theoretical as well as experimental studies, the origin of highly-anisotropic electronic properties of the SDW state continues to be a long-standing problem. Particularly, the role of symmetry protected Dirac cones remained unexplored. It may be noted that the recent ARPES measurements appear

to suggest only very small circle-like Fermi surfaces separated by $\sim (\pi/4, 0)$ and perhaps associated with the Dirac cones [2, 3]. This leads to the question whether these small circle-like Fermi surfaces can give rise to the nearly one-dimensional nature of the QPI patterns.

The anisotropic behavior of the conductivity observed experimentally [5,19,20] was captured by theoretical studies [21,22], though the origin of its unconventional nature was attributed obscurely to the interplay of correlation effects and bandstructure [23]. If the small circle-like structures in the Fermi surfaces are associated with Dirac cones [3, 24, 25], then it becomes crucial to understand their role in conductivity anisotropy. The orbital-weight distribution along the Dirac cone, especially in the vicinity of the Dirac point, may be highly anisotropic as compared to the portions of other bands which may cross the Fermi level.

In this chapter, we examine the anisotropic electronic properties in the SDW state of iron pnictides in order to understand the role of Dirac cones in anisotropy. We achieve this by examining Drude weight, optical conductivity, and quasiparticle interference in the Dirac semimetallic state within a minimal two-orbital model. An important advantage of the Dirac semimetallic state, which is easier to realize in the two-orbital model, is that there are no other bands crossing the Fermi level. Therefore, the contribution of Dirac cones in causing anisotropies in various electronic properties can distinctly be demarcated.

The minimal two-orbital model based on the orbitals d_{xz} and d_{yz} consists of two parts: the tight binding part and the interaction part, which are respectively given by the Eqs. (4.2.1) and (4.2.2). After decoupling various interaction terms, the resulting Hamiltonian in the $(\pi, 0)$ SDW state in two sublattice basis is represented by the Eq. 4.2.4.

The meanfield Hamiltonian for the SDW state takes a matrix form defined in the $\mathbf{k}$ and $\mathbf{k}+\mathbf{Q}$ basis described as

$$\begin{aligned}\hat{\mathcal{H}}_{mf} &= \sum_{\mathbf{k}\sigma} \Phi^{\dagger}_{\mathbf{k}\sigma} \begin{pmatrix} \hat{\varepsilon}_{\mathbf{k}} + \hat{N} - \delta\tau_z & \hat{\Delta}\mathrm{sgn}\,\bar{\sigma} \\ \hat{\Delta}\mathrm{sgn}\,\bar{\sigma} & \hat{\varepsilon}_{\mathbf{k}+\mathbf{Q}} + \hat{N} - \delta\tau_z \end{pmatrix} \Phi_{\mathbf{k}\sigma} \\ &= \sum_{\mathbf{k}\sigma} \Phi^{\dagger}_{\mathbf{k}\sigma} \hat{H}_{\mathbf{k}\sigma} \Phi_{\mathbf{k}\sigma}, \end{aligned} \tag{5.1.1}$$

where the basis set is $\Phi^{\dagger}_{\mathbf{k}\sigma} = (d^{\dagger}_{\mathbf{k}\alpha\sigma}, d^{\dagger}_{\mathbf{k}\beta\sigma}, d^{\dagger}_{\mathbf{k}+\mathbf{Q}\alpha\sigma}, d^{\dagger}_{\mathbf{k}+\mathbf{Q}\beta\sigma})$. α/β denote d_{xz}/d_{yz} orbitals of iron atom. Each matrix element in the above Hamiltonian is itself a 2×2 matrix in the orbital basis. The matrix elements $\hat{\varepsilon}_{\mathbf{k}}$ are momentum-dependent orbital energies, which are given by Eq. 4.3.5. τ is the Pauli matrix for the orbital basis. The exchange fields $\hat{\Delta}$ and $\hat{N}$, in terms of onsite interaction parameters, orbital magnetization, and

charge densities, are given by

$$\begin{aligned} 2\Delta_{\alpha\alpha} &= Um_\alpha + J\sum_{\alpha\neq\beta} m_\beta \\ 2N_{\alpha\alpha} &= (5J - U)n_\alpha, \end{aligned} \tag{5.1.2}$$

where the order parameters $m_{\alpha/\beta}$ and $n_{\alpha/\beta}$ are calculated self-consistently using eigenvalues and eigenvectors of the meanfield Hamiltonian $\hat{H}$, as outlined below.

$$\begin{aligned} n_\alpha &= \sum_{\mathbf{k}\sigma}\langle d^\dagger_{\mathbf{k}\alpha\sigma} d_{\mathbf{k}\alpha\sigma}\rangle \\ m_\alpha &= \sum_{\mathbf{k}\sigma}\langle d^\dagger_{\mathbf{k}+\mathbf{Q}\alpha\sigma} d_{\mathbf{k}\alpha\sigma}\rangle \mathrm{sgn}\,\sigma \end{aligned}$$

The following section describes methodologies to examine the low-energy collective excitations that include quasiparticle interference and optical conductivity in the SDW state.

5.2 Collective Excitations

5.2.1 Quasiparticle Interference using T-matrix approximation

Quasiparticle interference (QPI), which arises from the scattering of quasiparticles by impurity atoms, has been widely employed as a powerful probe of electronic structure, particularly near the Fermi energy. Theoretically, QPI can be studied by calculating modulation in the Green's function induced by scattering of the quasiparticle from an impurity potential. In the current work,we restrict ourselves to a single impurity with δ-potential such that the orbital state of the quasiparticle is preserved.

In the SDW state, a single particle Green's function is given by [12]

$$\hat{G}^0(\mathbf{k},\omega) = [(\omega + i\eta)\hat{I} - \hat{\mathcal{H}}_{mf}]^{-1} \tag{5.2.1}$$

where $\hat{I}$ is an identity matrix of dimension 4 and the basis chosen is $(d_{\mathbf{k}\,1\uparrow}, d_{\mathbf{k}\,2\uparrow}, d_{\mathbf{k}+\mathbf{Q}\,1\uparrow}, d_{\mathbf{k}+\mathbf{Q}\,2\uparrow})^T$. 1 and 2 refer to the d_{xz} and d_{yz} orbitals, respectively. The Hamiltonian matrix $\hat{\mathcal{H}}_{mf}$ is described by Eq. 5.1.1. The modification in the Green's function due to the scattering by a non-magnetic impurity can be obtained within the $\hat{T}$ matrix approximation as follows

$$\delta\hat{G}(\mathbf{k_1},\mathbf{k_2},\omega) = \hat{G}^0(\mathbf{k_1},\omega)\hat{T}(\omega)\hat{G}^0(\mathbf{k_2},\omega). \tag{5.2.2}$$

Here, $\hat{T}(\omega)$ matrix is given by

$$\hat{T}(\omega) = (\hat{I} - \hat{V}_{imp}\hat{\mathcal{G}}^0(\omega))^{-1}\hat{V}_{imp}. \tag{5.2.3}$$

$\hat{\mathcal{G}}^0(\omega)$ is obtained by summing over all the momenta in the Brillouin zone as follows

$$\hat{\mathcal{G}}^0(\omega) = \frac{1}{N}\sum_{\mathbf{k}} \hat{G}^0(\mathbf{k},\omega). \tag{5.2.4}$$

The impurity potential, owing to the orbital and momentum basis, also takes a 4 × 4 matrix form

$$\hat{V}_{imp} = V_0 \begin{pmatrix} \mathrm{I}_{2\times2} & \mathrm{I}_{2\times2} \\ \mathrm{I}_{2\times2} & \mathrm{I}_{2\times2} \end{pmatrix}.$$

$\mathrm{I}_{2\times2}$ is an identity matrix of dimension 2 and V_0 is the parameter denoting the strength of impurity potential.

The modification $\delta\rho(\mathbf{k},\omega)$ induced in the DOS by the impurity in the momentum space is obtained as

$$\delta\rho(\mathbf{q},\omega) \;=\; -\frac{i}{2\pi}\sum_{\mathbf{k}} g(\mathbf{k},\mathbf{q},\omega) \tag{5.2.5}$$

with

$$g(\mathbf{k},\mathbf{q},\omega) = Tr\delta\hat{G}(\mathbf{k},\mathbf{k}+\mathbf{q},\omega) - Tr\delta\hat{G}^*(\mathbf{k}+\mathbf{q},\mathbf{k},\omega).$$

The real space QPI pattern can be calculated via Fourier transform as follows

$$\delta\rho(\mathbf{r}_i,\omega) = \frac{1}{N}\sum_{\mathbf{k}} \delta\rho(\mathbf{q},\omega)e^{i\mathbf{k}\cdot\mathbf{r}_i}. \tag{5.2.6}$$

In the calculations, the impurity potential strength is fixed at $V_0 = 0.2$ and a mesh size of 300 × 300 is considered.

Fig. 5.1 shows constant-energy contours, QPI patterns, as well as modulations in the local density of states (LDOS) for an energy range spanning from ω = -0.05 to 0.05 with a step size of 0.05. The interaction parameters are chosen to be $U = 4.0$ and $J = 0.18U$ so as to obtain a Dirac semimetallic state in a self-consistent manner, which is possible near $\delta \approx 0.22$. In the Dirac semimetallic state, there are no additional bands that cross the Fermi level, unlike in the ordinary metallic SDW state. This makes the analysis possible for the contribution to the anisotropy that originates purely from the Dirac cone.

The first row shows the CECs with orbital distributions indicated by different colors. The cross sections of the Dirac cones appear to be of a single color in the vicinity

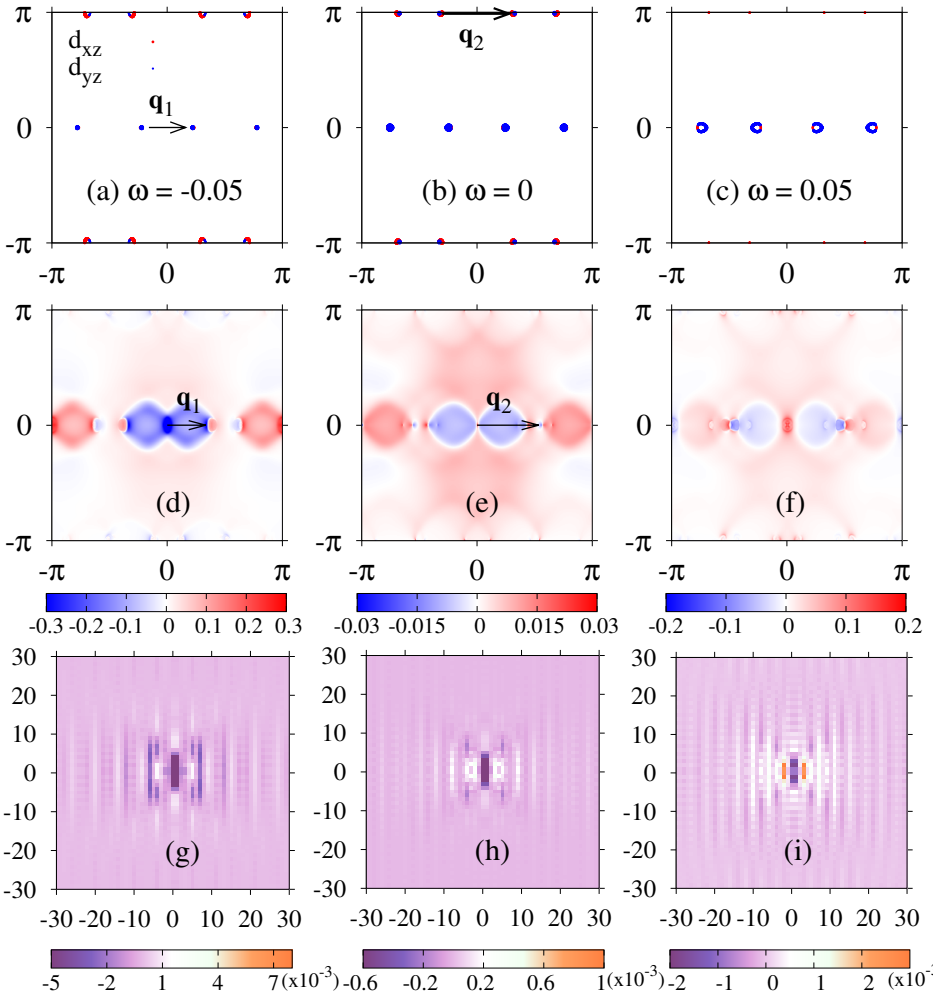

Figure 5.1: Constant energy contours (CECs) of the spectral function $\mathcal{A}(\mathbf{k}, \omega)$ plotted for energies (a) ω = -0.05, (b) $\omega = 0$, and (c) $\omega = 0.05$ in the semimetallic SDW state. $\mathbf{q}_1$ and $\mathbf{q}_2$ refer to the scattering vectors corresponding to intraorbital scattering for two pairs of Dirac cones located along $k_y = 0$ and $k_y = \pi$, respectively. Momentum-space and real-space QPI maps are shown in the second and third rows, respectively.

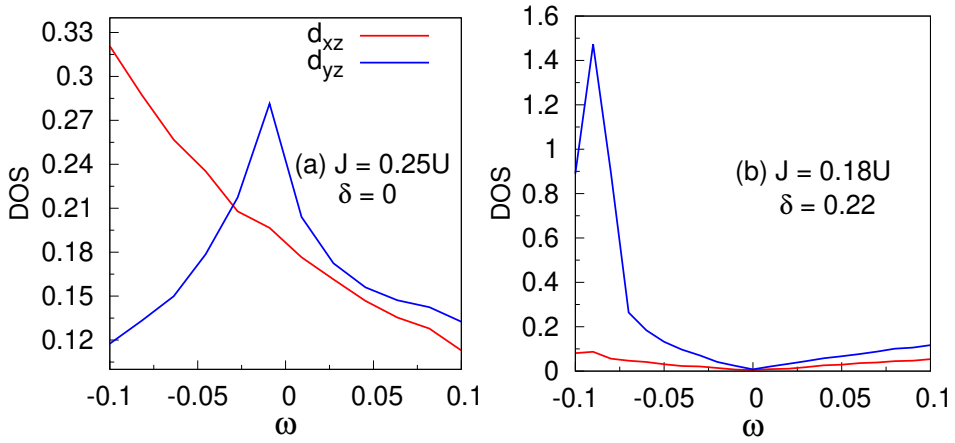

Figure 5.2: Orbital-resolved DOS as a function of energy ω for $U = 4.0$ in the (a) ordinary metallic state for $\delta = 0$ and (b) Dirac semimetallic state for $\delta = 0.22$.

of $\omega = 0$, though they are not. They appear so because of the non-circular shape of the pockets, which is not clearly visible because of their small size. Moreover, the weight of the two orbitals is also not equal for a given pair of Dirac cones, particularly when the orbital splitting is incorporated into the tight-binding part of the model in order to obtain the Dirac semimetallic SDW state. This can be seen from Fig. 5.2, which shows the orbital-resolved DOS as a function of ω. The orbital-resolved DOS is obtained as $\rho_\alpha(\omega) = \frac{1}{N}\sum_{\mathbf{k},n} |\langle \alpha \mid \psi_n(\mathbf{k})\rangle|^2 \, \delta\left(\omega - \varepsilon_n(\mathbf{k})\right)$, where $\psi_n(\mathbf{k})$ is the eigenvector corresponding to the band n and momentum $\mathbf{k}$. More clearly seen for higher ω, the pockets along $k_y = 0$ are primarily dominated by d_{yz} orbital, with a smaller contribution from d_{xz}. The two pairs of Dirac cones, one along $k_y = 0$ and the other along $k_y = \pi$, have opposite dominating orbitals. Therefore, it is expected that the inter-pair scattering of the Dirac cone is suppressed, which would otherwise have led to a modulation along the diagonal direction. Incidentally, there exists only a pair of Dirac cones in the SDW state obtained within most of the five-orbital models when a realistic-interaction parameter regime is chosen. Therefore, such complications do not arise there.

The dominance of a pair of Dirac cones along $k_y = 0$ is clearly visible in the QPI patterns (Fig. 5.1(d-f)). There exist strong modulating patterns along $q_y = 0$ arising as a result of the scattering vector $\mathbf{q}_1$ between the pair of Dirac cones along $q_y = 0$. There is another scattering vector $\mathbf{q_2}$, which may also be expected to contribute to the patterns as a result of the scattering between another pair of Dirac cones lying along $k_y = \pi$. However, $\mathbf{q_1}$ shows its dominance in the entire energy range considered, which is also reflected in the real space QPI patterns (Fig. 5.1 (g-i)), where the periodicity is determined solely by $\mathbf{q}_1$ scattering. This behavior can be understood in the context of orbital-resolved DOS as a function of energy (Fig. 5.2(b)). Notably, the contribution of d_{yz} orbital exceeds in comparison to the d_{xz} orbital in the whole considered energy regime (Fig. 5.2). As a result, the scattering between pockets with a dominant d_{yz} orbital character governs the overall QPI pattern.

At negative energy ($\omega = -0.05$), the pockets along $k_y = 0$ with a dominant d_{yz} contribution are separated by a distance of $\sim \pi/3$, resulting in a periodic modulation of $\sim 6a$ (Fig. 5.1 (g)). For the other two cases, the separation of the pockets along $k_y = 0$ changes slightly to $\sim \pi/2$, producing a modulation with periodicity $\sim 4a$ (Figs. 5.1 (h) and (i)). For the Dirac cone located along $k_y = 0$, the difference in the magnitude of the scattering vectors for positive and negative ω arises because the band dominated by the d_{xz} orbital is approximately given by $k_x \sim c$ in the vicinity of the Dirac points, while the other band dominated by the d_{yz} orbital has a slope $\sim \pi/3$ [26]. Thus, the d_{yz} dominated regions shift across the Dirac point as the energy

changes from negative to positive.

5.2.2 Optical Conductivity

To examine the influence of the Dirac cone on charge transport, we investigate the optical conductivity σ_l along $l = x$ or y directions with the antiferromagnetic and ferromagnetic arrangement of magnetic moments, respectively. The components of optical conductivity along different directions can be represented by the Eqs. 3.2.3 and 3.2.4 [27, 28].

The orbital dependent kinetic energy T^l_{nn} and current $j^l_{nn'}$ operators can be written in the following manner.

$$\begin{aligned} T^l_{nn} &= \sum_{\alpha\beta} T^{l;\alpha\beta}_{nn} = \sum_{\alpha\beta} \frac{\partial^2 \varepsilon_{\alpha\beta}(\mathbf{k})}{\partial k_l^2} c^*_{\mathbf{k}\alpha n} c_{\mathbf{k}\beta n} \\ j^l_{nn'} &= -\sum_{\alpha\beta} j^{l;\alpha\beta}_{nn'} = -\sum_{\alpha\beta} \frac{\partial \varepsilon_{\alpha\beta}(\mathbf{k})}{\partial k_l} c^*_{\mathbf{k}\alpha n} c_{\mathbf{k}\beta n}, \end{aligned} \tag{5.2.7}$$

where $c_{\mathbf{k}\alpha n}$ denotes the matrix element of the unitary transformation that connects the orbital and sublattice basis to the band representation.

In order to gain insight into the origin of anisotropy, we define orbital-dependent components of the Drude weight as follows.

$$\frac{D^{\alpha\beta}_l}{2\pi} = \frac{1}{2N} \sum_{\mathbf{k}} T^{l;\alpha\beta}_{nn}(\mathbf{k}) \theta(-\varepsilon_{n\mathbf{k}}) - \frac{1}{N} \sum_{\mathbf{k}, n\neq n'} \mathrm{Re} \frac{j^{l;\alpha\beta^*}_{nn'}(\mathbf{k}) j^l_{nn'}(\mathbf{k})}{\varepsilon_{n'\mathbf{k}} - \varepsilon_{n\mathbf{k}}} \theta(-\varepsilon_{n'\mathbf{k}}) \theta(\varepsilon_{n\mathbf{k}}). \tag{5.2.8}$$

We discuss the role of the Dirac cone in the contribution to anisotropy of optical conductivity. Fig. 5.3 shows the Drude weight along the x-direction with the magnetic moments ordered antiferromagnetically as well as along y-direction with magnetic moments ordered ferromagnetically. Fig. 5.3(a) shows Drude weight when the SDW state is an ordinary metal, while Fig. 5.3(b) shows the Drude weight when the SDW state is a Dirac semimetal. We find that in the ordinary metallic SDW state, the anisotropy parameter defined as a ratio of two Drude weights is nearly one, away from the chemical potential μ^* corresponding to the band filling of $n = 2$. μ^* is obtained through the self-consistent process whereas the variation of chemical potential is only for the illustration purpose where the self-consistently obtained parameters are fixed to be that corresponding to μ^*.

Notably, the band filling $n = 2$ in the unordered state of the two-orbital model reproduces the Fermi surfaces obtained via bandstructure calculations except for an

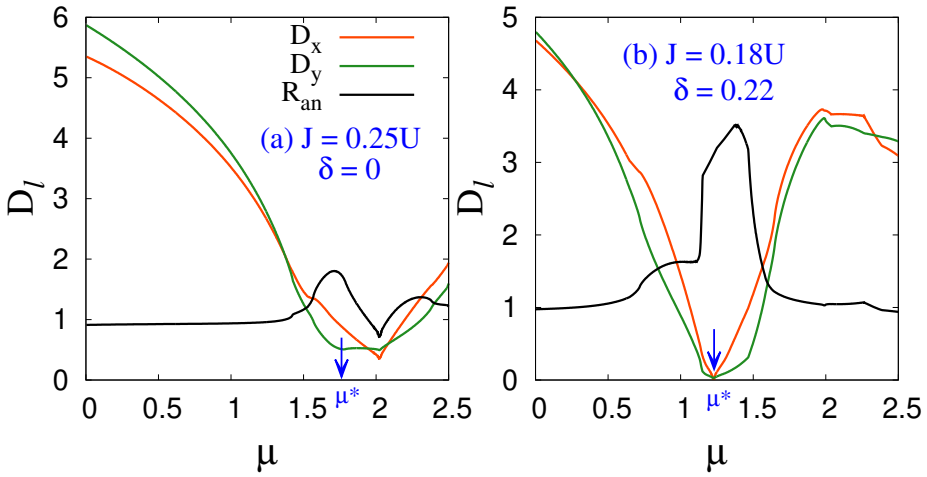

Figure 5.3: Drude weights along $l = x$- and y-directions with anisotropy parameter defined as $R_{an} = \frac{D_x}{D_y}$ in the (a) ordinary metallic and (b) Dirac semimetallic states.

extra pocket near (π, π) and significant contribution of d_{xy} orbital at the Fermi level. The anisotropy parameter deviates from unity only in the immediate vicinity of μ^*. More importantly, the Dirac points are also in the vicinity of the Fermi level corresponding to this band filling, though on the opposite of the Fermi level. In other words, if the Dirac points had been absent, the anisotropy in the Drude weight would have been weak. This can be seen in Fig. 5.3(b), where the Drude weight along different directions is plotted for the Dirac semimetallic SDW state with the Dirac points located at the Fermi level. In this case, the Drude-weight anisotropy maximizes in the vicinity of μ^*.

A much clearer insight into the origin of anisotropy can be obtained via Fig. 5.4, which shows individual components of the anisotropy such as D_x^{11}, D_x^{22}, etc. The superscripts 1 and 2 correspond to d_{xz} and d_{yz} orbitals, respectively. Along the x direction, in both D_x^{11} and D_x^{22}, there is a linear drop as one approaches μ^* and a rise thereafter. On the other hand, both get flattened near μ^* along y. An opposite trend is shown by D^{12}, however, the two contributions, each from D_x^{11} and D_x^{22} results in the Drude weight enhanced along x-direction as compared to y-direction. As expected, the difference in optical conductivity along the two orthogonal directions is more prominent in the low-energy region (see Fig. 5.5). Moreover, this difference is further enhanced in the Dirac semimetallic SDW state. However, one interesting point to be noted is that, near $\omega \sim 1$ and beyond, σ_y becomes larger than σ_x as one would have expected conventionally that the conductivity should be better along the ferromagnetic direction.

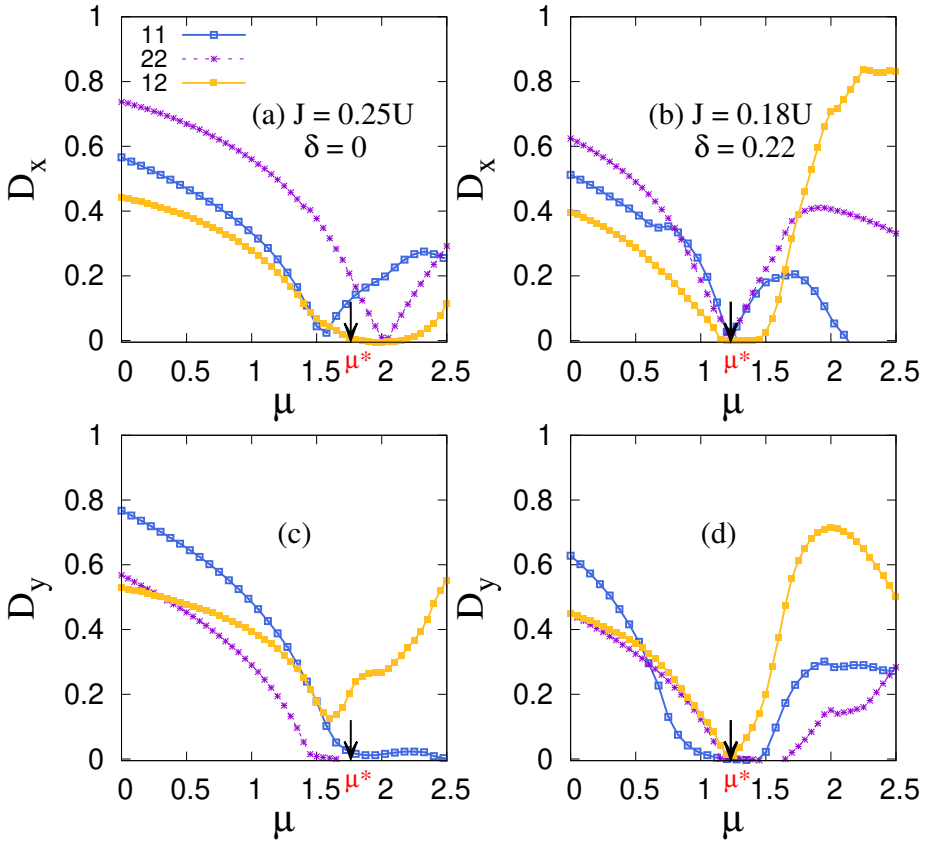

Figure 5.4: Various components of the Drude weights along the (a) x and (c) y-directions for the ordinary metallic state, while ((b) and (d)) correspond to those for the Dirac semimetallic state.

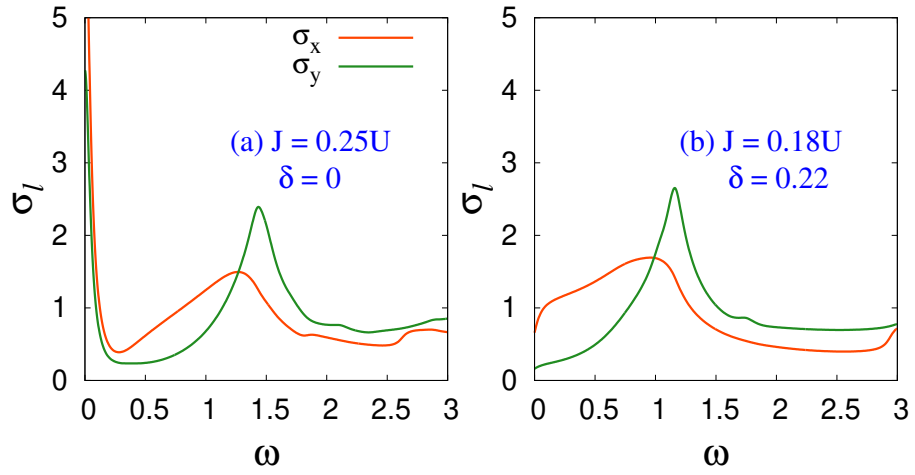

Figure 5.5: Conductivity along x- and y-direction in the (a) metallic and (b) semimetallic SDW states.

5.3 Summary

We find that the highly-anisotropic distribution of orbital weights in the vicinity of Dirac cones accompanied with anisotropic hoppings associated with d_{xz} and d_{yz} orbitals may be a significant contributor to the unusually large anisotropy in the optical conductivity and other electronic properties. An another important consequence of Dirac cones not being far away from the Fermi surface, we find nearly one-dimensional modulation for the quasiparticle interference though with modulation wavevector $\sim \pi/3 - \pi/2$ in the momentum space and nearly four to six times the interatomic distance between two nearest neighbor iron atoms.

To conclude, we used a minimal two-orbital model to demonstrate the contribution from Dirac nodes to the anisotropic electronic properties of the iron pnictides in the SDW state. This is achieved by introducing an orbital splitting, which further lowers the energy of d_{xz} orbital, and helps in bringing the Dirac point at the Fermi level, suppressing band crossings, and hence in obtaining a Dirac semimetallic state so that one can clearly demarcate the role of Dirac cones in contribution to anisotropy.

Bibliography

[1] Chu J -H, Analytis J G, Greve K De, McMahon P L, Islam Z, Yamamoto Y, and Fisher I R 2010 *Science* **329** 824

[2] Valenzuela B, Bascones E, and Calderón M J 2010 *Phys. Rev. Lett.* **105** 207202

[3] Fisher I R, Degiorgi L, and Shen Z X 2011 *Rep. Prog. Phys.* **74** 124506

[4] Richard P *et al* 2010 *Phys. Rev. Lett.* **104** 137001

[5] Tanatar M A, Blomberg E C, Kreyssig A, Kim M G, Ni N, Thaler A, Bud'ko S L, Canfield P C, Goldman A I, Mazin I I, and Prozorov R 2010 *Phys. Rev. B* **81** 184508

[6] Chuang T -M, Allan M P, Lee J, Xie Y, Ni N, Bud'ko S L, Boebinger G S, Canfield P C, and Davis J C 2010 *Science* **327** 181

[7] Blomberg E C, Tanatar M A, Kreyssig A, Ni N, Thaler A, Hu R, Bud'ko S L, Canfield P C, Goldman A I, and Prozorov R 2011 *Phys. Rev. B* **83** 134505

[8] Rosenthal E P, Andrade E F, Arguello C J, Fernandes R M, Xing L Y, Wang X C, Jin C Q, Millis A J, and Pasupathy A N 2014 *Nat. Phys.* **10** 225

[9] Song C -L *et al* 2011 *Science* **332** 1410

[10] Singh D K and Majumdar P 2018 *Phys. Rev. B* **98** 195130

[11] Knolle J, Eremin I, Akbari A, and Moessner R 2010 *Phys. Rev. Lett.* **104** 257001

[12] Singh D K and Majumdar P 2017 *Phys. Rev. B* **96** 235111

[13] Allan M P *et al* 2013 *Nat. Phys.* **9** 220

[14] Zhou X, Ye C, Cai P, Wang X, Chen X, and Wang Y 2011 *Phys. Rev. Lett.* **106** 087001

[15] Singh D K, Akbari A, and Majumdar P 2018 *Phys. Rev. B* **98** 180506(R)

[16] Plonka N, Kemper A F, Graser S, Kampf A P, and Devereaux T P 2013 *Phys. Rev. B* **88** 174518

[17] Nakajima *et al* 2011 *Proc. Natl. Acad. Sci. U.S.A.* **108** 12238

[18] Watson M D *et al* 2019 *npj Quantum Mater.* **4** 36

[19] Chu J -H, Analytis J G, Press D, Greve K De, Ladd T D, Yamamoto Y, and Fisher I R 2010 *Phys. Rev. B* **81** 214502

[20] Kobayashi T, Tanaka K, Miyasaka S, and Tajima S J 2015 *Phys. Soc. Jpn.* **84** 094707

[21] Sugimoto K, Kaneshita E, and Tohyama T J 2011 *Phys. Soc. Jpn.* **80** 033706

[22] Zhang X and Dagotto E 2011 *Phys. Rev. B* **84** 132505

[23] Blomberg E C, Tanatar M A, Fernandes R M, Mazin I I, Shen B, Wen H -H, Johannes M D, Schmalian J, and Prozorov R 2013 *Nat. Commun.* **4** 1914

[24] Ran Y, Wang F, Zhai H, Vishwanath A, and Lee D -H 2009 *Phys. Rev. B* **79** 014505

[25] Hasan M Z and Bernevig B A 2010 *Physics* **3** 27

[26] Goyal G and Singh D K 2023 *J. Phys.: Condens. Matter* **35** 365501

[27] Dagotto E 1994 *Rev. Mod. Phys.* **66** 763

[28] Valenzuela B, Calderón M J, León G, and Bascones E 2013 *Phys. Rev. B.* **87** 075136

Chapter 6

Collective excitations in DSM state with AFM order: a revisit to the two-orbital model of iron-based superconductor

This chapter uncovers the behavior of bulk electronic states within a two-orbital model when the second-nearest-neighbor intraorbital hopping is suppressed that leads to perfect nesting of the Fermi surface with (π, π) ordering.

6.1 Introduction

In the preceding chapters, we have investigated the Dirac semimetallic state in the $(\pi, 0)$ spin-density-wave state of iron pnictides using a multi-orbital Hubbard model. The existence of a Dirac cone in the SDW state is guaranteed by symmetries and therefore only the metallic state is stabilized for iron pnictides [1]. In addition, there exists residual Fermi surfaces often indicated in various studies. To realize a semimetallic phase in the presence of SDW order, an orbital splitting between the d_{xz} and d_{yz} orbitals was introduced. This splitting effectively aligns the Dirac nodes with the Fermi level and suppresses extraneous band crossings at the same energy. Moreover, a very recent angle resolved photoemission spectroscopy (ARPES) measurement appears to indicate the crossing of the Fermi level by Dirac cones only [2, 3].

Thus, a comprehensive and consistent picture from both sets of experiments and theories suggest that crossing of the Fermi level by Dirac nodes can play an important role in the anisotropic electronic properties of these systems. This proposal is further substantiated by QPI results obtained through our calculations, where only the Dirac cones cross the Fermi level. The quasiparticle interference and optical conductivity were investigated within the two-orbital Hubbard model in the semimetallic state which were found to be anisotropic in which Dirac cones play a dominant contribution. The model employed is based on the minimal two-orbital framework proposed by Raghu *et al.* [4], which includes the d_{xz} and d_{yz} orbitals and hopping terms were considered up to second-nearest neighbors.

A particularly noteworthy case arises when a perfectly nested (π, π)-ordered AFM

order is realized upon suppressing the second-neighbor intraorbital hopping. This behavior stands in contrast to the $(\pi, 0)$ SDW phase observed in the parent compounds of high-T_c iron pnictide superconductors, where perfect nesting is absent [5] and the orbital weight is distributed differently across the electron and hole pockets [6,7]. The observation naturally leads to the question of whether a robust topological semimetallic character can exist under the constraint of vanishing second nearest-neighbor intraorbital hopping. Furthermore, it is also of interest to investigate the band topology associated with the antiferromagnetic phase. If realized, this would constitute an additional instance where a topological semimetallic state emerges without requiring spin–orbit coupling.

The possibility of topologically protected edge states, optical conductivity, signature of electronic states through quasiparticle interference in such a system offers an additional avenue for probing the relationship between magnetic ordering and the underlying electronic structure. These questions provide the central motivation for the present chapter. In the following sections, we explore the realization of the semimetallic state in the (π, π) AFM phase when the next-nearest-neighbor intraorbital hopping is suppressed, and examine the resulting bulk and edge-state spectra within the two-orbital Hubbard model framework.

6.2 Model and Method

We consider a square lattice comprising two Fe atoms per unit cell and neglect interlayer coupling between neighboring iron planes. With the magnetic moments assumed to be oriented along the z-axis, we construct the mean-field decoupled Hamiltonian for the antiferromagnetic phase within a two-orbital model, excluding next-nearest-neighbor intraorbital hopping t_3. The Hamiltonian, expressed in the sublattice-orbital basis, takes the form:

$$H_{\mathbf{k}} = \sum_{\mathbf{k},\sigma} \Psi^{\dagger}_{\mathbf{k}\sigma} H_{AFM} \Psi_{\mathbf{k}\sigma}, \tag{6.2.1}$$

where

$$H_{AFM}(\mathbf{k}) = \begin{pmatrix} H^{\sigma}_{\alpha}(\mathbf{k}) & H^{\sigma}_{\alpha\beta}(\mathbf{k}) \\ H^{\sigma}_{\beta\alpha}(\mathbf{k}) & H^{\sigma}_{\beta}(\mathbf{k}) \end{pmatrix} \tag{6.2.2}$$

Here, each block is a 2×2 matrix defined for a spin σ. The intraorbital matrices H^{σ}_{α} and H^{σ}_{β} represent contributions from d_{xz} and d_{yz} orbitals, respectively, while $H^{\sigma}_{\alpha\beta}$ captures the interorbital hybridization. The basis for the above matrix constitutes $(A\alpha, B\alpha, A\beta, B\beta)$, where A and B denote two sublattices, associated with majority

spin-up and spin-down configurations, respectively.

The individual matrices are represented as

$$H_\alpha(\mathbf{k}) = \begin{pmatrix} -\Delta_\alpha + N_\alpha & 2t_1 \cos k_x + 2t_2 \cos k_y \\ 2t_1 \cos k_x + 2t_2 \cos k_y & \Delta_\alpha + N_\alpha \end{pmatrix}, \tag{6.2.3}$$

$$H_\beta(\mathbf{k}) = \begin{pmatrix} -\Delta_\beta + N_\beta & 2t_2 \cos k_x + 2t_1 \cos k_y \\ 2t_2 \cos k_x + 2t_1 \cos k_y & \Delta_\beta + N_\beta \end{pmatrix}, \tag{6.2.4}$$

and

$$H_{\alpha\beta}(\mathbf{k}) = \begin{pmatrix} -4t_4 \sin k_x \sin k_y & 0 \\ 0 & -4t_4 \sin k_x \sin k_y \end{pmatrix}. \tag{6.2.5}$$

The hopping parameters t_1 and t_2 correspond to nearest-neighbor intraorbital hopping along the x- and y-directions, respectively, while t_4 describes next-nearest-neighbor interorbital hopping. The next-nearest-neighbor intraorbital hopping term t_3 is neglected. In this work, all parameters are measured in units of $|t_1|$, with the chosen values $t_1 = -1$, $t_2 = 1.3$, and $t_4 = -0.85$.

The exchange field Δ_α and orbital-dependent potential N_α for an orbital α are given by:

$$\begin{aligned} 2\Delta_\alpha &= U m_\alpha + J m_\beta, \\ 2N_\alpha &= (5J - U) n_\alpha \end{aligned} \tag{6.2.6}$$

where m_α and n_α denote the magnetization and charge density for an orbital α, while U and J represent on-site Coulomb repulsion and Hund's coupling, respectively.

Figure 6.1 illustrates the electronic band dispersion of the two-orbital model proposed by Raghu *et al.* in the absence of magnetic ordering, with the second-nearest-neighbor intraorbital hopping parameter t_3 set to zero. In this nonmagnetic phase, the system exhibits metallic behavior. The band structure features an electron pocket centered at the $\Gamma(0, 0)$ point and a hole pocket at the $M(\pi, \pi)$ point. The corresponding Fermi surface is shown in Fig. 6.2.

It can be clearly noted that the omission of t_3 leads to a perfectly nested Fermi surface characterized by the nesting vector $\mathbf{Q} = (\pi, \pi)$. In this case, the electron pockets at $(\pi, 0)$ and $(0, \pi)$, which are present when t_3 is finite, disappear, yielding a highly symmetric Fermi surface with an identical orbital-weight distribution all along the Fermi surface for both the hole and electron pockets. Such a Fermi-surface topology is likely to support checkerboard-type antiferromagnetic order.

The Hamiltonian H_{AFM} respects two key symmetry operations [1]:

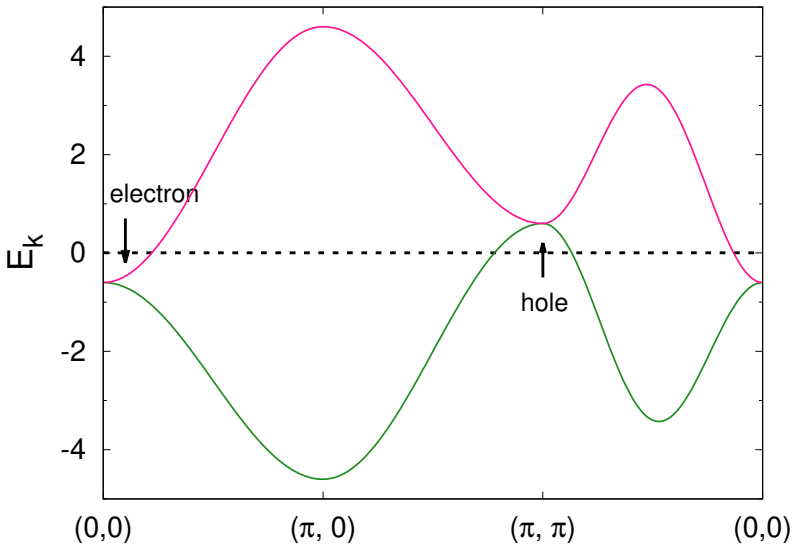

Figure 6.1: Electronic band dispersion along the high-symmetry directions in the unordered state with $t_3 = 0$ within a two-orbital model of Raghu *et al.* The corresponding state is metallic with hole and electron pockets explicitly indicated.

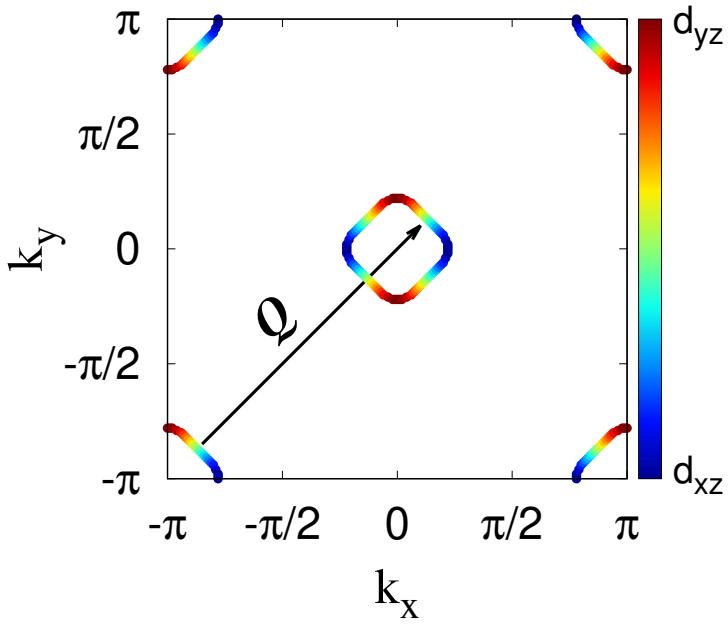

Figure 6.2: Fermi surface in the unordered state with $t_3 = 0$ within the two-orbital model of Raghu *et al.* The system exhibits perfect nesting between electron and hole pockets with ordering vector $\mathbf{Q} = (\pi, \pi)$. The color scale indicates the orbital character of the Fermi pockets.

- Inversion symmetry $\mathcal{I}$, requiring $H_{AFM}(-\mathbf{k}) = H_{AFM}(\mathbf{k})$ and
- Combined time-reversal ($\mathcal{T}$) and reversal of magnetic moments $\mathcal{S}$, denoted by $\mathcal{TS}' = \mathcal{T} \circ \mathcal{S}$, where $\mathcal{S}$ corresponds to flipping of the magnetization direction. This combined operation satisfies $\mathcal{TS}'^{-1} H_{AFM}(-\mathbf{k}) \mathcal{TS}' = H_{AFM}(\mathbf{k})$.

This set of symmetries, which are only slightly different from the one that protect the Dirac cones in the $(\pi, 0)$ SDW state, may support the Dirac cone in the checkerboard-type AFM order as to be discussed below. Another important difference from $t_3 \neq 0$ case is the absence of mismatch of vorticities for the hole and electron pockets. In the current case, the vorticity of both the hole and electron pockets are same. Despite that a Dirac semimetallic state can be supported.

Such Dirac points were indicated earlier in the spin-density-wave state with hidden magnetic order, featuring a nodal behavior in the quasiparticle excitation spectrum at the Fermi surface [8].

6.3 Bulk dispersion

In the antiferromagnetically ordered state obtained self-consistently, the well-nested Fermi pockets present in the unordered phase undergo a reconstruction, leading to the emergence of Dirac points (DPs), as illustrated in Fig. 6.3(a). The interaction strengths are chosen as $U = 4.0$ and $J = 0.25U$. Later, we will discuss the condition on the interaction parameter for obtaining Dirac semimetallic state with magnetic order. Each Dirac point receives non-uniform distribution of d_{xz} and d_{yz} orbitals, which does depend on the strength of interaction.

All Dirac points are aligned along the diagonal of the Brillouin zone, i.e., Γ–M direction. Of these, four are located at the vertices of a small square surrounding the Γ point, while the remaining four appear in the extended Brillouin zone near its corners. No additional band crossings occur at the Fermi level, confirming the realization of a Dirac semimetallic phase with antiferromagnetic order. The inset of Fig. 6.3(a) shows the linear energy dispersion near a representative Dirac point along the k_x direction, providing clear evidence of the topological character of these crossings. Since the Dirac points are situated along the $[1, 1]$ direction, where $k_x = k_y$, the dispersion along the k_y direction is identical.

Figures 6.3(b) and (c) present the constant-energy contours at $\omega = 0.2$ for interaction strengths $U = 4.0$ and $U = 6.5$, respectively. For $U = 4.0$ [Fig. 6.3(b)], the Fermi pockets exhibit contributions from both orbitals, with each orbital character dominating in distinct regions of momentum space. These pockets are symmetrically

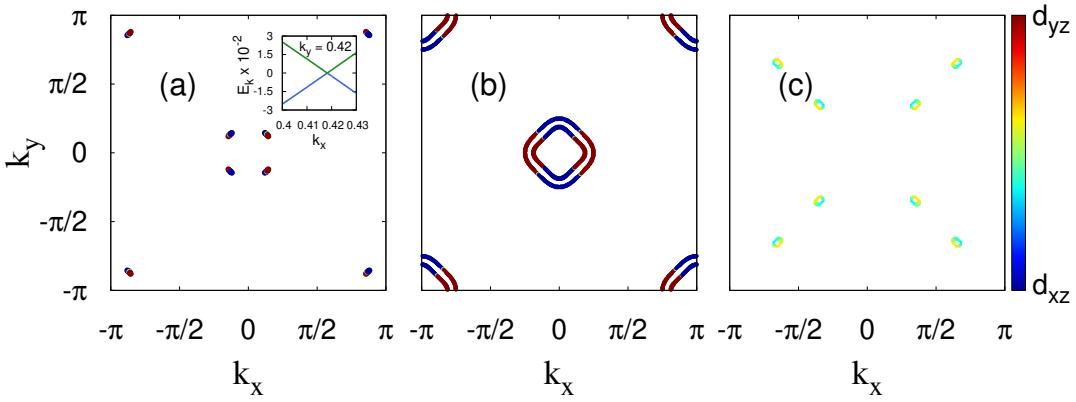

Figure 6.3: Evolution of constant energy contours (CECs) as a function of U in the (π, π) ordered state. (a) and (b) display CECs at $\omega = 0$ and 0.2, respectively, for $U = 4.0$ while (c) displays the result for $U = 6.5$ at $\omega = 0.2$. The Fermi pockets shrink to Dirac points for $U = 4.0$ with equal contributions from both d_{xz} and d_{yz} orbitals. The inset plot in (a) displays linearity of band dispersion in the vicinity of one of the DPs in k_x-direction. The Hund's coupling is taken as $J = 0.25U$. The color palette represents transition of the orbital character.

distributed across the Brillouin zone, in accordance with the underlying (π, π) magnetic ordering. As the interaction strength is increased to $U = 6.5$ [Fig. 6.3(c)], the portions of the pockets progressively lose their distinct orbital character and instead consist of a coherent admixture of both orbitals. Upon a further increase in U, the system transitions into an insulating phase, accompanied by the disappearance of the low-energy contours.

Notably, when the next-nearest-neighbor intraorbital hopping is absent, the resulting semimetallic phase is associated with a checkerboard pattern of magnetic moments corresponding to (π, π) ordering. This magnetic configuration is essential for the preservation of Dirac points. This stands in contrast to the $(\pi, 0)$ SDW state, where protection of the nodal Dirac points arises from the collinear magnetic order, the inversion operation about the iron atom, and the combined effect of time-reversal and spin-reversal operations.

To analyze the effect of interaction strength on the band structure, Fig. 6.4 shows the electronic dispersion for several values of U, with $J = 0.25U$ fixed. For $U = 4.0$ [Fig. 6.4(a)], the system exhibits linearly dispersing band crossings along the $M \to \Gamma$ path. The dispersion is shown for a single spin species; however, due to $\mathcal{TS}'$ symmetry, the bands remain spin-degenerate across the full Brillouin zone. Consequently, the band crossing points represent true Dirac nodes. The corresponding density of states (DOS) for this parameter set are shown in Fig. 6.5(a). The DOS displays multiple pronounced peaks over the considered energy window, symmetrically distributed

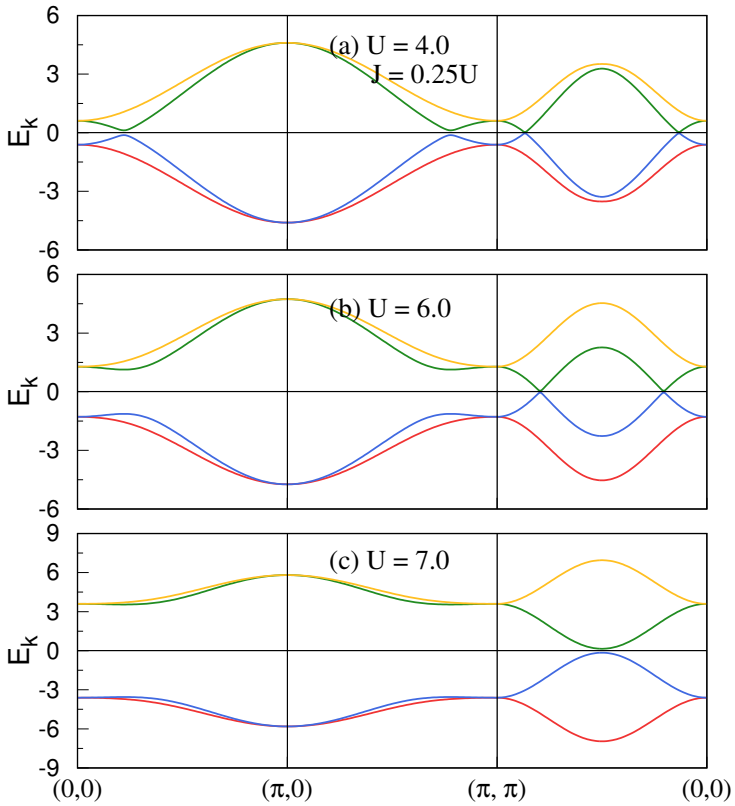

Figure 6.4: Electronic band dispersion in the (π, π) ordered state for varying U and $J = 0.25U$. (a) $U = 4.0$: Dirac cones with linearly dispersing nodes along (π, π) to $(0, 0)$. (b) $U = 6.0$: Dirac points shift in momentum space. (c) $U = 7.0$: a full gap opens, indicating an insulating phase.

about $\omega = 0$. The closest peaks appear at $|\omega| \sim 0.1$, followed by sharp peaks near $|\omega| \sim 3.5$, with a weak cusp around $\omega \sim 4.5$. The sharp peak features reflect the large availability of electronic states associated with the underlying band structure, in particular, they may correspond to band extrema.

Upon increasing the interaction strength to $U = 6.0$ [Fig. 6.4(b)], the Dirac points shift away from the high-symmetry points in the Brillouin zone. With a further increase to $U = 7.0$ [Fig. 6.4(c)], a gap opens at the Fermi level, signaling the collapse of the semimetallic phase and the emergence of an insulating state. The corresponding DOS for these cases are displayed in Figs. 6.5(b) and (c), respectively. In both cases, the DOS vanishes at $\omega = 0$; however, a clear distinction emerges in the immediate vicinity of $\omega = 0$. Specifically, the DOS is vanishingly small near $\omega = 0$ for $U = 6.0$, consistent with semimetallic behavior, whereas it is strictly zero for $U = 7.0$, shown in the inset plot of Fig. 6.5(c), confirming the insulating nature of the latter. Furthermore, due to the nature of magnetic ordering, the DOS contributions from the two orbitals are identical and therefore they overlap for each case.

Next, we study the behavior of optical conductivity in the three distinct regions

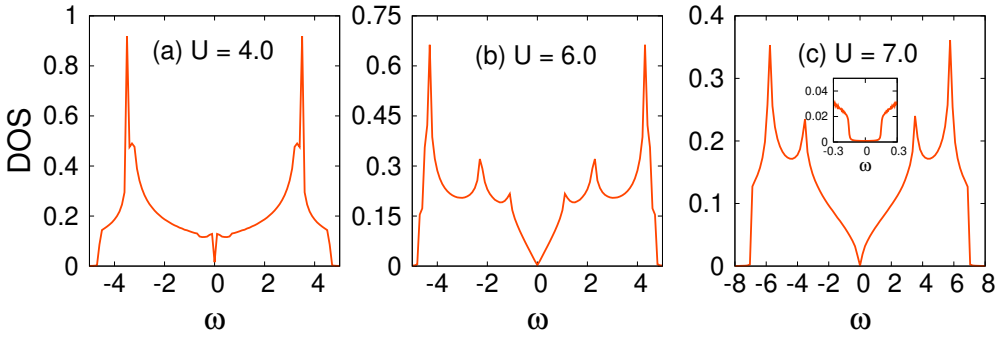

Figure 6.5: Density of states for three different Us corresponding to DSM ((a) and (b)) and insulating (c) states as in the Fig. 6.4.

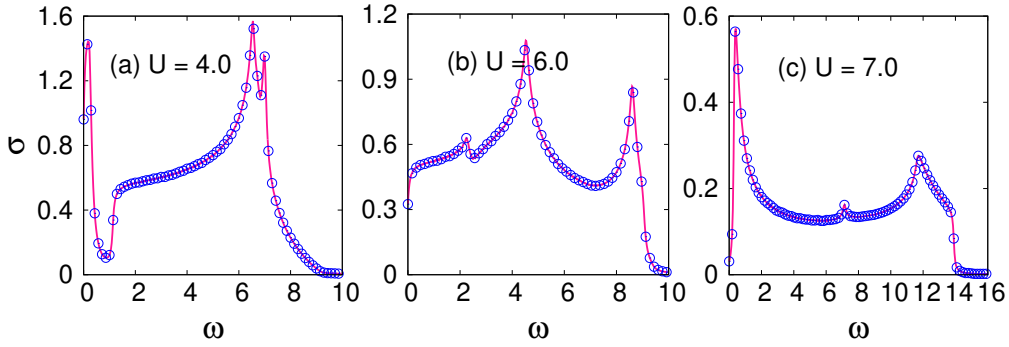

Figure 6.6: Optical conductivity for three different Us corresponding to DSM ((a) and (b)) and insulating (c) states as in the Fig. 6.4.

with set of parameters identified above. The optical conductivity components along two orthogonal directions are described by Eqs. (3.2.3)–(3.2.5), in which the Hamiltonian matrix is given by Eq. 6.2.1 and the corresponding spectra are presented in Fig. 6.6. Each prominent peak in the optical conductivity originates from interband transitions for the portions of bands containing their extrema, as substantiated by the corresponding peaks observed in the density of states. A large peak near $\omega \sim 0$ in the DSM state for $U = 4$ is indicative of large DOS available just slightly away from the Fermi surface because of the band extrema not being far away. In the DSM state with $U = 6.0$, the DOS or optical conductivity approaches zero as $\omega \to 0$ whereas the opening of gap at $\omega = 0$ for $U = 7$ can be clearly seen. However, a very sharp peak again arises due to the availability of band extrema close to the Fermi level. When no additional bands are present as in the case of $U = 6$, a constant behavior for smaller value of ω can be observed. Moreover, owing to the (π, π) magnetic ordering and the resulting absence of any four-fold rotation symmetry breaking, the optical conductivities are identical along the x- and y-directions as expected.

This observation indicates the existence of a critical interaction strength $U = U_c$, beyond which the system makes a transition to an insulating state. This means the semimetallic state is realized only within a finite window of interaction parameter. The precise condition and the specific range of interaction parameters required for the realization of a Dirac semimetallic state is obtained in the next section.

6.3.1 Necessary condition for DPs

In the (π, π) ordered state, the four-fold rotational symmetry remains intact even in the presence of magnetic ordering. Furthermore, in the absence of orbital anisotropy and orbital splitting, the orbital occupancies and orbital magnetization of the individual orbitals d_{xz} and d_{yz} become equal, i.e., $n_\alpha = n_\beta = 1.0$ and $m_\alpha = m_\beta$. Consequently, the exchange field and orbital-dependent potential become orbital-independent:

$$\Delta_\alpha = \Delta_\beta = \Delta, \;\; N_\alpha = N_\beta = N \tag{6.3.1}$$

Also, from Fig. 6.3, it is seen that the DPs are obtained along $[\pi, \pi]$, where $|k_x| = |k_y|$. By substituting this condition into the AFM ordered Hamiltonian [Eq.(6.2.2)], the eigenvalues can be obtained analytically which are expressed as:

$$\lambda_i = \pm\sqrt{a^2 + c^2} \pm d + b \tag{6.3.2}$$

where $i = 1, \ldots, 4$ labels the four eigenvalues of the Hamiltonian, and the following shorthand notations have been used:

$$a = \Delta, \;\; b = N, \;\; c = 2(t_1 + t_2)\, \cos k_x, \;\; d = -4t_4\, \sin^2 k_x \tag{6.3.3}$$

The presence of Dirac points at the Fermi level requires that the energy eigenvalue λ_i vanishes at specific momenta $\mathbf{k}_0 = (k_x^0, k_y^0)$. This leads to the equation:

$$(a^2 + c^2) = (b \pm d)^2 \tag{6.3.4}$$

Solving this equation for $\sin^2 k_x^0$ yields:

$$\sin^2 k_x^0 = -\frac{1}{8t_4^2}((t_1 + t_2)^2 \pm 2Nt_4) \pm \frac{1}{8t_4^2}\sqrt{(t_1 + t_2)^4 + 4t_4(4t_4 \pm N)(t_1 + t_2)^2 + 4\Delta^2 t_4^2} \tag{6.3.5}$$

where only those solutions satisfying $0 \leq \sin^2 k_x^0 \leq 1$ are physically admissible.

In Eq. (6.3.5), the second term in the square-root is strictly positive, whereas the first term can take either sign. Consequently, the value of $\sin^2 k_x^0$ is determined by the

combined contribution of the two terms. A physically valid solution requires this sum to be non-negative, which occurs either when the first term is positive or the second term should be sufficiently large to offset a negative first term. For the parameter set considered, at least one of these conditions is always met, ensuring $\sin^2 k_x^0 \geq 0$.

Imposing an additional constraint $\sin^2 k_x^0 \leq 1$ yields an inequality

$$\Delta \leq -(N + 4t_4) \tag{6.3.6}$$

This relation establishes the necessary condition for the existence of Dirac points at the Fermi level by explicitly linking the exchange field Δ, the orbital-dependent charge potential N, and the effective second-neighbor kinetic energy scale t_4. Violation of this condition leads to the annihilation of the Dirac points, thereby driving the system into an insulating phase. For the case $J = 0.25U$, the Dirac semimetallic phase is obtained within a finite interaction window, $4.0 \sim U \sim 7.0$. Below this range, the magnetic moment vanishes, while above it the necessary condition is no longer satisfied, resulting in a transition to an insulating state.

6.3.2 Effective Hamiltonian

To understand the low-energy excitations around the Dirac points (DPs), we derive an effective Hamiltonian in the vicinity of a nodal point located at momentum $\mathbf{k}_0 = (k_x^0, k_y^0)$. Introducing a small momentum deviation $\mathbf{q} = (q_x, q_y)$ such that $\mathbf{k} = \mathbf{k}_0 + \mathbf{q}$, we use a Taylor expansion to expand the AFM ordered Hamiltonian around a DP with momentum $\mathbf{k}_0$ to a linear order in $\mathbf{q}$.

The resulting low-energy effective Hamiltonian is given by:

$$\begin{aligned} H_{\text{eff}}(\mathbf{k}_0 + \mathbf{q}) = N(\tau_0 \otimes s_0) - \Delta(\tau_0 \otimes s_3) + (t_1 + t_2)(\cos k_x^0)(\tau_0 \otimes s_1) \\ -4t_4(\pm \sin^2 k_x^0)(\tau_1 \otimes s_0) - 4t_4(\sin k_x^0 \cos k_x^0)(q_y \pm q_x)(\tau_1 \otimes s_0) \\ \sin k_x^0[(-q_x t_1 \pm q_y t_2)((\tau_0 + \tau_3) \otimes s_1) + (\pm q_y t_1 - q_x t_2)((\tau_0 - \tau_3) \otimes s_1)] \end{aligned} \tag{6.3.7}$$

where τ_i and s_i are the Pauli matrices acting in the orbital and sublattice subspaces, respectively, and τ_0, s_0 are 2×2 identity matrices in their respective spaces. Here, $\pm$ sign indicates whether $k_x = k_y$ or $k_x = -k_y$.

This effective Hamiltonian encapsulates the anisotropic Dirac-like dispersion near the nodal points. Notably, both q_x and q_y appear linearly in the expansion, further confirming analytically the linearity of band dispersion in both directions around the DPs—characteristic of Dirac semimetals. However, the exact expression for the linearized dispersion is cumbersome due to the complexity of parameters involved,

but one can easily see the linearized dispersion numerically in the immediate vicinity of Dirac points (also shown in the inset plot of Fig. 6.3(a)).

6.4 Edge state dispersion

Now, we examine the edge state dispersion in the Dirac semimetallic state with AFM order by considering a ribbon geometry. The system is taken to be infinite along the x-direction and finite along the y-direction, resulting in open boundary conditions in the y-axis and periodicity along x. In this setup, k_x remains a good quantum number. The corresponding ribbon Hamiltonian $H_{\mathrm{Rbx}}(k_x)$ for a finite width $N = 50$ is constructed in the pseudo-real space in the sublattice and orbital basis $(1A\alpha, 1A\beta, 1B\alpha, 1B\beta, 2A\alpha, 2A\beta, 2B\alpha, 2B\beta, \cdots)$ whose block structure is written as

$$H_{Rbx}(k_x) = \begin{pmatrix} h_1 & h_2 & h_3 & h_4 & O & O & \cdots \\ h_2^* & -h_1 & h_4 & h_3 & O & O & \cdots \\ h_3^* & h_4^* & h_1 & h_2 & h_3 & h_4 & \cdots \\ h_4^* & h_3^* & h_2^* & -h_1 & h_4 & h_3 & \cdots \\ O & O & h_3^* & h_4^* & h_1 & h_2 & \cdots \\ O & O & h_4^* & h_3^* & h_2^* & -h_1 & \cdots \\ \vdots & \vdots & \vdots & \vdots & \vdots & \vdots & \ddots \end{pmatrix} \tag{6.4.1}$$

where h_1 contains elements that belong to the same chain and sublattice while h_2 connects the elements within the same chain but opposite sublattices. In contrast, h_3 and h_4 connects elements belonging to the neighboring chains combined with the same and different sublattices, respectively. Each sub-block of the Hamiltonian has the following matrix form:

$$h_1 = \begin{pmatrix} \Delta_\alpha & 0 \\ 0 & \Delta_\beta \end{pmatrix} \tag{6.4.2}$$

$$h_2 = \begin{pmatrix} 2t_1 \mathrm{cos}k_x & 0 \\ 0 & 2t_2 \mathrm{cos}k_x \end{pmatrix} \tag{6.4.3}$$

$$h_3 = \begin{pmatrix} 0 & -2it_4 \mathrm{sin}k_x \\ -2it_4 \mathrm{sin}k_x & 0 \end{pmatrix} \tag{6.4.4}$$

$$h_4 = \begin{pmatrix} t_2 & 0 \\ 0 & t_1 \end{pmatrix} \tag{6.4.5}$$

Figure 6.7 shows the edge state spectra for three different values of U, keeping

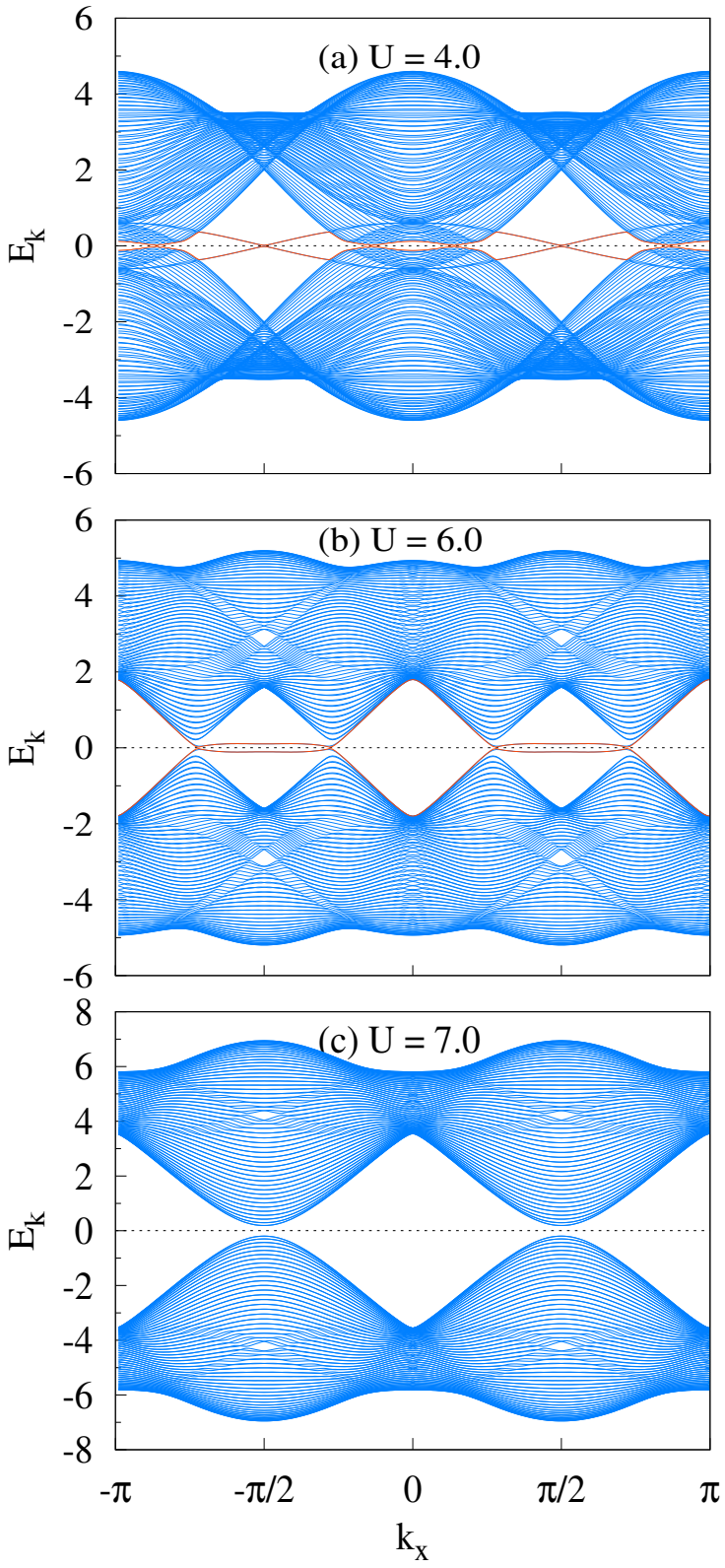

Figure 6.7: Edge state dispersion for a ribbon oriented along the x-direction with finite width $N = 50$ along y in the (π, π) SDW state. Results are shown for different interaction strengths: (a) $U = 4.0$, (b) $U = 6.0$, and (c) $U = 7.0$. Edge states (shown in orange) are distinguished from bulk bands (shown in blue).

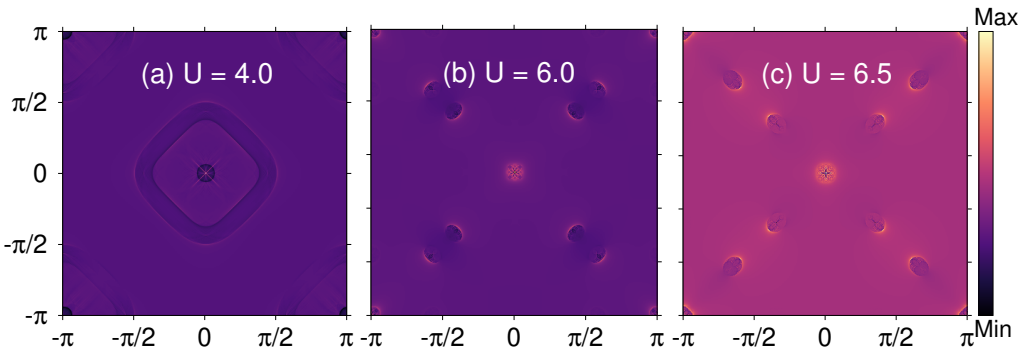

Figure 6.8: Momentum-space QPI patterns for the non-magnetic impurity in the DSM state for different U at $\omega = 0.2$.

$J = 0.25U$ fixed.

For $U = 4.0$ [Fig. 6.7(a)], three distinct pairs of edge states appear symmetrically around $k_x = 0$. These edge modes (highlighted in orange) are localized near the boundaries and clearly separated from the bulk bands (shown in blue). Notably, the edge states located near $k_x = 0$ and $k_x = \pi$ are the reflections of Dirac points observed in the bulk band structure (see Fig. 6.4(a)). An additional crossing at $k_x = \pm\pi/2$ emerges, likely resulting from the band folding effects.

As U increases to 6.0 [Fig. 6.7(b)], the edge states near $k_x = \pm\pi/2$ disappear, while those corresponding to the Dirac points persist and shift in momentum space in accordance with the evolution of bulk Dirac nodes. Interestingly, the edge states form loop-like structures around $k_x = \pm\pi/2$, indicating their topological origin.

When U exceeds the critical value U_c, the Dirac points annihilate and a bulk gap opens, as shown in Fig. 6.7(c) for $U = 7.0$. In this case, the edge states disappears, confirming the transition to a trivial insulating phase.

Due to the preserved lattice symmetry, the edge-state spectrum remains insensitive to a ribbon orientation along y or to the presence of an odd number of chains.

6.5 Quasiparticle Interference

To investigate the nature of the electronic states in the vicinity of the Fermi level, quasiparticle interference (QPI) serves as a powerful probe, as it captures interference patterns arising when the quasiparticles are scattered elastically from the impurity atoms. Theoretically, QPI can be analyzed within the T-matrix formalism, as outlined in Sec. 5.2.1. In the present study, we restrict our analysis to intra-orbital scattering processes, such that an electron initially occupying a given orbital scatters only into states with the same orbital character. The scattering potential V_0 is fixed at a value

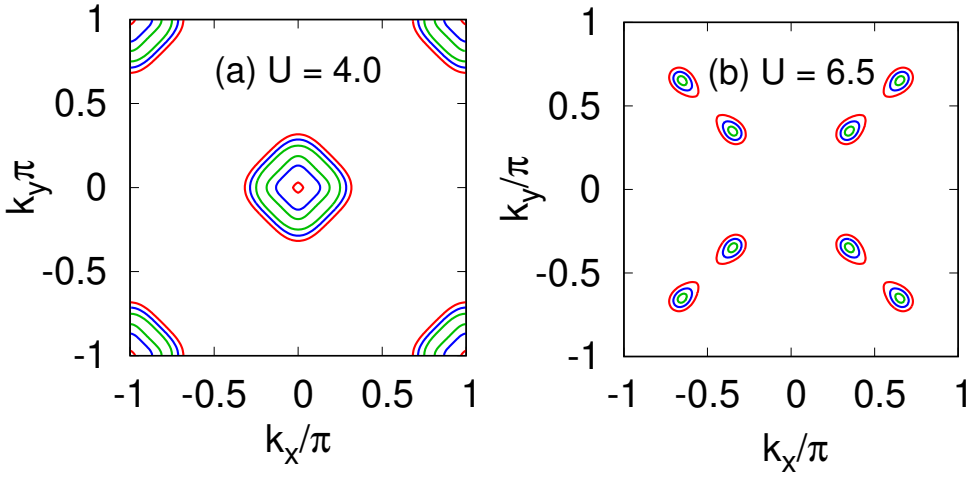

Figure 6.9: Constant energy contours (CECs) at different energies, plotted in different colors, in the DSM state for (a) U = 4.0 and (b) U = 6.5. The lowest energy contour is obtained for $\omega = 0.2$ and shown in green color while the highest energy contour is obtained for 0.6 and shown in red with an increment of 0.2 (shown in blue).

0.1 for all the calculations.

Figure 6.8 presents the momentum-space quasiparticle interference (QPI) patterns generated by a non-magnetic impurity in the Dirac semimetallic phase at $\omega = 0.2$ for different values of the Coulomb interaction strength U. For $U = 4.0$, the QPI response is characterized by concentric diamond-shaped features centered around the Γ point, originating predominantly from intrapocket scattering. This behavior can be understood by examining the constant-energy contours shown in Fig. 6.9(a) at energies 0.2, 0.4, and 0.6 (indicated by different colors). In this regime, additional bands except the ones forming Dirac cones lie sufficiently close to the Fermi level and exhibit varying dominant orbital character in different momentum regions, leading to diamond-like contours and corresponding features in the QPI patterns.

In contrast, for $U = 6.0$ [Fig. 6.8(b)] and $U = 6.5$ [Fig. 6.8(c)], the QPI patterns are obtained along the diagonals of the BZ and are governed primarily by interpocket scattering between distinct Dirac pockets, as substantiated by the constant-energy contours in Fig. 6.9(b). The pocket like structures along $q_x = q_y$ include both Umklapp and non-Umklapp scatterings. The structure nearest to Γ appears because of interpocket scattering between nearest constant energy pockets across the Brillouin zone folding line. Similarly, the structure in the vicinity of (π, π) appears because of Umklapp scattering between another pair of distant constant energy contours located across the Brillouin zone folding line. The remaining QPI structure results because of scattering between pockets inside the reduced Brillouin zone.

6.6 Conclusion

In this chapter, we have demonstrated that a Dirac semimetallic state can be robustly realized within a two-orbital Hubbard model in the presence of a perfectly nested (π, π) ordered Fermi surface, achieved by suppressing the next-nearest-neighbor intraorbital hopping term t_3. Unlike the $(\pi, 0)$ SDW phase commonly associated with iron pnictides, the (π, π) magnetic ordering preserves fourfold rotational symmetry, resulting in equal but anisotropic orbital occupancies and magnetization for the d_{xz} and d_{yz} orbitals. This symmetry restoration plays a central role in stabilizing Dirac points in the reconstructed band structure. Another important difference from the $(\pi, 0)$ SDW phase is that the Dirac semimetallicity disappears when the on-site Coulomb parameter is increased beyond a certain critical value.

Our analysis of the bulk electronic dispersion reveals the emergence of symmetry-protected Dirac points aligned along the Γ–M direction of the Brillouin zone, with linear dispersion in their vicinity and equal contributions from both orbitals. By systematically varying the interaction strength U, we have identified a finite window in parameter space over which the Dirac semimetallic phase persists. Beyond a critical interaction strength, the Dirac points annihilate and a full gap opens at the Fermi level, signaling a transition to an insulating phase. The corresponding density of states and optical conductivity spectra consistently reflect this evolution, with the latter exhibiting complete isotropy in the x- and y-directions as a direct consequence of the (π, π) ordering and the absence of orbital polarization.

An analytical condition for the existence of Dirac points at the Fermi level has been derived, explicitly linking the exchange field, orbital-dependent potential, and kinetic energy scales. This condition provides clear insight into the mechanism driving the semimetal–insulator transition and establishes the minimal requirements for realizing a Dirac semimetallic phase in the present model. Furthermore, the effective low-energy Hamiltonian constructed near the Dirac points confirms the Dirac-like nature of the quasiparticle excitations and elucidates the anisotropic linear dispersion in momentum space.

The topological character of the Dirac semimetallic phase is further substantiated by our investigation of edge-state spectra in ribbon geometries. In the semimetallic regime, gapless edge states emerge and evolve in tandem with the bulk Dirac points, while these states become fully gapped once the system enters the insulating phase. The disappearance of edge modes concomitant with the bulk gap opening confirms the close correspondence between bulk topology and boundary excitations. Additionally, quasiparticle interference calculations reveal characteristic scattering signatures

dominated by inter-Dirac-pocket processes, providing experimentally accessible fingerprints of the Dirac semimetallic state.

Overall, this chapter establishes that a (π, π)-ordered antiferromagnetic phase in a minimal two-orbital framework can host a symmetry-protected Dirac semimetallic state over a finite interaction range. These findings highlight the crucial role of magnetic ordering, orbital symmetry, and hopping structure in shaping the low-energy electronic topology, and they offer a complementary perspective to the more extensively studied $(\pi, 0)$ SDW phase of iron pnictides. The results presented here may serve as useful model studies for Dirac semimetallic behavior in correlated magnetic materials.

Bibliography

[1] Ran Y, Wang F, Zhai H, Vishwanath A, and Lee D -H 2009 *Phys. Rev. B* **79** 014505

[2] Watson M D *et al* 2019 *npj Quantum Materials* **4** 36

[3] Richard P *et al* 2010 *Phys. Rev. Lett.* **104** 137001

[4] Raghu S, Qi X -L, Liu C -X, Scalapino D J, and Zhang S -C 2008 *Phys. Rev. B* **77** 220503(R)

[5] Brydon P M R *et al* 2011 *J. Phys.: Condens. Matter* **23** 246001

[6] Lv W and Phillips P 2011 *Phys. Rev. B* **84** 174512

[7] Valenzuela B, Bascones E, and Calderón M J 2010 *Phys. Rev. Lett.* **105** 207202

[8] Rodriguez J P 2020 *Phys. Rev. B* **102** 024521

Chapter 7

Summary and Future Scope

This chapter encapsulates the key contributions of the thesis and outlines promising directions for future research.

7.1 Summary

This thesis is focused on the theoretical studies of topological semimetallic (TSM) states in two-dimensional magnetically ordered systems, driven by their potential relevance to future technological applications in spintronics, low-dissipation transport, anisotropic electronic behavior, and anomalous Hall responses. Particular emphasis is placed on Dirac semimetals (DSMs) supported by specific symmetry constraints within realistic interaction regimes. In the current work, two different systems were explored: (i) One without spin-orbit coupling but involved more than one orbital. Two types of the magnetic ordering were considered, one with spin-density wave (SDW) order with ordering wave vector $(\pi, 0)$ and checkerboard antiferromagnetic order with ordering wavevector (π, π). (ii) The other system, which was explored in detail, was the non-symmorphic crystal accompanied with the antiferromagnetic (AFM) ordering in the presence of spin-orbit coupling.

Key findings of the thesis are summarized as follows:

- **Dirac semimetallic state with $(\pi, 0)$ spin-density wave phase:** Using a two-orbital model with on-site Coulomb interaction, we showed that by tuning the orbital splitting (OS) between d_{xz} and d_{yz} orbitals, the location of symmetry-protected Dirac points can be brought exactly at the Fermi level. Moreover, the same process suppresses non-Dirac Fermi pockets, resulting in a DSM-SDW phase with linear dispersion at the Fermi level. The necessary condition for the same is obtained and the effective Hamiltonian is derived.

  The inclusion of the OS parameter has been motivated by its presence in the high-temperature state with tetragonal symmetry and nematic order, and experimentally, it can be realized by applying in-plane stress on the sample. The nematic phase is marked by the presence of a short-range order with broken

four-fold rotation symmetry and is observed at a temperature $T > T_{SDW}$ in several iron-based superconductors. It was noted that the lattice anisotropy in the orthorhombic symmetry cannot give rise to a splitting as large as ≈ 60 meV between the d_{xz} and d_{yz} orbitals. This perhaps indicates that the OS, which persists into the high temperature tetragonal phase, in addition to the orthorhombic symmetry or magnetic order, could be the key factor behind the anisotropic electronic behavior. Therefore, it is not unreasonable to include such splitting in the low-temperature phases such as the SDW state. OS can be controlled by applying appropriate pressure such as an in-plane stress.

The current findings not only identify an interesting minimal model without spin-orbit coupling, which supports symmetry protected Dirac-semimetallic state with collinear magnetic order $(\pi, 0)$, but they also provide important insight into various experimentally observed anisotropic electronic states and the role of Dirac cones in the anisotropic electronic properties of iron-based superconductors in the SDW state. This is investigated through detailed analysis of the Drude-weight anisotropy, quasiparticle interference, and optical conductivity.

Various possible distinct edge states existing for different ribbon geometry running along ferromagnetic arrangement of magnetic moments or another running along antiferromagnetic arrangement of magnetic moments are investigated. In the case when the ribbon is running along the ferromagnetic direction, two possible edge states are found depending on whether the number of ferromagnetic chains is even or odd.

- **Topological Semimetallic State with (π, π) order:** In the minimum two-orbital model of iron pnictides, it is further demonstrated that there exists a window in the largest interaction parameter, i.e., on-site Coulomb interaction U, when a Dirac semimetallic state can be realized with checkerboard-type antiferromagnetic order. This can be achieved via setting the second-neighbor intra-orbital hopping process to zero in the minimal two-orbital model. The perfect Fermi-surface nesting stabilizes a (π, π) ordered state. In addition, we investigated the nature of edge states, signature of associated collective excitations such as quasiparticle inteference and optical conductivity over a finite range of parameters, within which the crossover from Dirac semimetallic phase to an insulating state or to the normal state can clearly be identified. The Dirac semimetallic state obtained in this model has important differences from the Dirac semimetallic state with $(\pi, 0)$-type SDW state order. The most important difference is the transition to an insulating state for higher strength of interac-

tion which is contrary to the guaranteed metallic nature of $(\pi, 0)$-type SDW order. Secondly, because of four-fold symmetric state, there is no anisotropy in the nature of edge states or in the optical conductivity. The quasiparticle interference patterns are also four-fold symmetric. It may be noted that in the aforementioned two cases of Dirac semimetallic state with checkerboard or collinear magnetic order, the inversion symmetry was intact. Next, we investigated magnetically ordered states without inversion symmetry.

- **TSM State in Non-Symmorphic System with AFM ordering:** We investigated topological semimetallic states with non-symmorphic symmetry in the Rasbha-Hubbard model. In this case, the time-reversal ($\mathcal{T}$) and inversion ($\mathcal{P}$) symmetries are broken individually in a 2D AFM ordered system. The orientation of the magnetic moments and external magnetic field like term was shown to tune the system between Dirac and Weyl semimetallic phases. In the phase diagram, in the parameter space of U vs λ, we found that with increasing interaction strength, Dirac points annihilate each other, opening a bulk gap. This transition from semimetallic to insulating behavior was also reflected in the evolution of dispersion of symmetry protected edge states associated with the Dirac or Weyl points. In this state, we studied optical conductivity and quasiparticle interference (QPI) to probe the nature of collective excitations and electronic states. Our finding suggests an anisotropic electronic state is reflected in the Drude weight and optical conductivity as well as in quasiparticle inteference patterns. The anisotropy arises as a result of subtle interplay between the spin-orbit coupling and the magnetic ordering. It may be noted that the spin-orbit coupling or the AFM magnetic order cannot generate anisotropy individually.

Overall, this work establishes that symmetry-tuned magnetically ordered phases can host topologically nontrivial Dirac semimetallic states in a two-dimensional system. The interplay between topology, magnetic order, and electron correlations opens pathways for designing quantum materials with potential applications in spintronics and low-power electronics because of their interesting electronic properties studied in the current work.

7.2 Scope for Future Study

The search for two-dimensional topological semimetals, which can host Dirac and Weyl points, has intensified in recent times. Graphene remains one prominent non-

magnetic model system while the signature of Dirac points has also been noticed in the α-bismuthene. An example of a magnetically ordered system exhibiting evidence of Dirac points is the metallic spin-density state of iron pnictides. Results of the theoretical studies carried out here for symmorphic system without spin-orbit coupling and non-symmorphic system with spin-orbit coupling suggest that TSM phases can provide important insight into the behavior of such systems to be realized in near future as demonstrated in the case of spin-density wave state of iron pnictides.

- **Extensions to multi-orbital system:** In the current work, our study was limited to only one-orbital model in the case of non-symmorphic crystal with spin-orbit coupling or two-orbital case without any spin-orbit coupling. However, it would be interesting to extend the current work to multi-orbital case with spin-orbit coupling with or without non-symmorphic symmetry so that the multi-band effect or multi-orbital effect on topological properties can be studied as material systems to be discovered in the near future are likely to be multi-orbital systems.

- **TSM with complex spin-charge-orbital order**. Our study largely focused on the magnetically ordered topological semimetals. A multi-orbital correlated electron system can support magnetic, charge, orbital order or any combination of these. It would be interesting to explore the possibility of topological semimetals in such crystals with or without nonsymmorphic symmetry. Moreover, it would be interesting to explore and identify model systems or materials which can support semimetallic states with spin-charge, spin-orbital, or spin-charge-orbital order. These directions promise to enrich the understanding of topological quantum materials and support the development of innovative devices based on their exotic electronic and spin properties.

- **Magnetic excitations:** In the current work, we largely focused on collective excitations such as optical conductivity, quasiparticle interference, etc. It is also important to explore and understand the nature of magnetic excitations which can be probed experimentally via inelastic-neutron scattering or resonant inelastic x-ray spectroscopy. Such excitations can provide understanding of the nature and strength of correlation existent in such systems. In addition, one will be able to gain insight into the consequence of interplay between the Dirac fermion and collective spin excitations.

- **Extension to 3D Systems and Layered Structures:** In the magnetic topological semimetals in 3D, the Dirac/Weyl nodes can result from the interplay

of magnetism and band topology, leading to exotic properties. The candidate materials include $Co_3Sn_2S_2$ and Mn_3Sn. Our study can easily be extended for such magnetic topological semimetals by choosing an appropriate tight-binding part of the Hamiltonian.

- **Beyond Mean-Field Approaches:** Our study extensively used the static meanfield approximation to explore the interplay of magnetism and topology of bands. It would be interesting to incorporate dynamical electron correlations using methods such as Dynamical Mean-Field Theory (DMFT) which can provide more accurate insights into quasiparticle lifetimes and many-body effects in the presence of topologically protected linear band crossing.

- **Topological Transport Phenomena:** The current work is focused only on properties such as the nature of edge-states, quasiparticle interference, optical conductivity. However, it would be of strong interest to investigate transport signatures such as anomalous hall effect and magnetoresistance, etc. that can reveal novel response in magnetically ordered topological semimetals.

List of Publications

Publications based on the present research work:

[1] **Garima Goyal** and Dheeraj Kumar Singh, "Semimetallic spin density wave state in iron pnictides," 2023 *J. Phys.:Condens Matter* **35** 365501
10.1088/1361-648X/acda05

[2] **Garima Goyal** and Dheeraj Kumar Singh, "Antiferromagnetically ordered topological semimetals in Hubbard model with spin-orbit coupling," 2024 *J. Phys.:Condens Matter* **36** 265802
10.1088/1361-648X/ad3792

[3] **Garima Goyal** and Dheeraj Kumar Singh, "Role of Dirac cones in the anisotropic properties associated with the spin-density wave state of iron pnictides," 2025 *New J. Phys.* **27** 083503
10.1088/1367-2630/adf34f

[4] **Garima Goyal** and Dheeraj Kumar Singh, "Anisotropic electronic state in two-dimensional topological semimetal with checkerboard-type antiferromagnetic order," 2026 *Phys. Rev. B* **113** 094408

Other SCI Publications:

[1] Aastha Jain, **Garima Goyal**, and Dheeraj Kumar Singh, "Weyl semimetallic state with antiferromagnetic order in the Rashba-Hubbard model," 2024 *Phys. Rev. B* **110** 075134
https://doi.org/10.1103/PhysRevB.110.075134

[2] **Garima Goyal** and Dheeraj Kumar Singh, "Insight into interplay between bandstructure and Coulomb interaction via quasiparticle interference," 2025 *J. Phys.:Condens Matter* **37** 245601
10.1088/1361-648X/add77e

[3] Harun Al Rashid, **Garima Goyal**, Alireza Akbari, and Dheeraj Kumar Singh, "Temperature dependence of quasiparticle interference in d-wave superconductors," 2023 *SciPost Phys.* **6** 033
10.21468/SciPostPhysCore.6.2.033

[4] **Garima Goyal** and Dheeraj Kumar Singh, "Hund's coupling and electronic anisotropy in the spin-density wave state of iron pnictides," 2022 *Physica B: Condensed Matter* **644** 414223
https:/ /doi.org/10.1016/j.physb.2022.414223

[5] **Garima Goyal**, Aastha Jain, and Dheeraj Kumar Singh, "Estimating damping effects using a smartphone," 2023 *Phys. Teach.* **61** 708
https://doi.org/10.1119/5.0150235

Conferences Attended

National Conferences/Symposium:

[1] Poster presentation: Dependence of drude weight anisotropy on the interaction parameters, (**Garima Goyal** and Dheeraj Kumar Singh), delivered online at the *"65th DAE Solid State Physics Symposium"* organized by Bhabha Atomic Research Centre, Mumbai, India (2021).

[2] Poster presentation: Semimetallic spin-density wave state in iron pnictides, (**Garima Goyal** and Dheeraj Kumar Singh), delivered at *"13th Spectroscopies of Novel Superconductors (SNS 2022)"* organized by Indian Institute of Science, Bangalore (2022).

[3] Poster presentation: Role of orbital splitting in Fermi-surface reconstruction of spin-density wave state of iron pnictides, (**Garima Goyal** and Dheeraj Kumar Singh), delivered at *"66th DAE Solid State Physics Symposium"* organized by Bhabha Atomic Research Centre, Mumbai, held at Birla Institute of Technology, Mesra, Ranchi (2022).

[4] Poster presentation: Semimetallic spin-density wave state in iron pnictides, (**Garima Goyal** and Dheeraj Kumar Singh), delivered at *"Young Quantum"* organized by QIC group, HRI Allahabad (2023).

[**5**] Poster presentation: Topological semimetals with antiferrromagnetic order in Hubbard model, (**Garima Goyal** and Dheeraj Kumar Singh), delivered at *"Annual Conference on Quantum Condensed Matter (QMAT 2023)"* organized by National Institute of Science Education & Research, Bhubaneswar, India (2023).

[**6**] Poster presentation: Edge states for a ribbon oriented in the diagonal direction in 2D antiferromagnetically ordered semimetals, (**Garima Goyal** and Dheeraj Kumar Singh), delivered at *"68th DAE Solid State Physics Symposium"* organized by Bhabha Atomic Research Centre, Mumbai, India (2024).

[**7**] Oral presentation: Antiferromagnetically ordered topological semimetals in Hubbard model with spin-orbit coupling, (**Garima Goyal** and Dheeraj Kumar Singh), delivered at *"National Symposium on Theoretical Sciences"* organized by Thapar Institute of Engineering and Technology, Patiala, Punjab (2025).

International Conferences/Symposium:

[**1**] Poster presentation: Role of Dirac cones in the anisotropic properties associated with the spin-density wave state of iron pnictides, (**Garima Goyal** and Dheeraj Kumar Singh), delivered at *"International Conference on Strongly Correlated Quantum Materials (ICSCQM)"* organized in Hvar, Croatia (2025).

arima_DKS.pdf

ORIGINALITY REPORT

(Dr. Prabal Pratap Singh Bhadauria)

11%	5%	9%	1%
SIMILARITY INDEX	INTERNET SOURCES	PUBLICATIONS	STUDENT PAPERS

PRIMARY SOURCES

1	scipost.org Internet Source	1%
2	Nan Lin Wang, Hideo Hosono, Pengcheng Dai. "Iron-based Superconductors - Materials, Properties and Mechanisms", Pan Stanford, 2019 Publication	<1%
3	Dheeraj Kumar Singh, Yunkyu Bang. "Doping-induced disorder and conductivity anisotropy in the spin density wave state of iron pnictides", Physical Review B, 2020 Publication	<1%
4	www.db-thueringen.de Internet Source	<1%
5	Dheeraj Kumar Singh, Pinaki Majumdar. "Drude weight anisotropy in the doped iron pnictides: The primary role of orbital weight redistribution along the reconstructed Fermi surfaces", Physical Review B, 2018 Publication	<1%
6	Nikolay Plakida. "High-Temperature Cuprate Superconductors", Springer Nature, 2010 Publication	<1%
7	Leslie M. Schoop, Florian Pielnhofer, Bettina V. Lotsch. "Chemical Principles of Topological Semimetals", Chemistry of Materials, 2018 Publication	<1%